Heat sinks based on liquid metal for power electronics cooling applications

Yerasimos Yerasimou

M. Eng

School of Engineering
Newcastle University

A thesis submitted for the degree of
Doctor of Philosophy

August 2020

Abstract

Power semiconductor devices are key components for efficient power conversion in a wide range of industrial applications. The continuous trend toward increasing the power capability and decreasing the chip area of the semiconductors results in the generation of high heat fluxes, due to the power losses. Also, power electronics are one of the most common components of the power converter to fail, as a result of the thermomechanical stress within the structure of power module caused by large junction temperature swings (ΔT_{j}). Effective and efficient thermal management systems should therefore be employed to dissipate the excess heat to the ambient environment and reduce the thermomechanical stress.

Liquid metals received little attention as heat transport agents thus far, in spite of their excellent thermophysical properties. Also, their high electrical conductivity allows for driving them with a magnetohydrodynamics (MHD) pump, which is a reliable and low–power device. Hence, a thermal management system based on $Ga_{68}In_{22}Sn_{10}$ liquid metal coolant is able to remove high heat fluxes, requires low operating power and provides high reliability; all desirable attributes for modern power electronic applications.

This thesis focuses on the design and development of a cooling system based on liquid metal for conventional insulated–gate bipolar transistors (IGBTs), which are the most widely used power electronic switches for medium–to–high power conversion applications. The proposed heat sink is attached to the IGBT power module and liquid metal is impinged directly against the baseplate with the use of an integrated MHD pump, thus eliminating the need for thermal interface material (TIM). Moreover, an adaptive thermal management method based on liquid metal flow control is presented that is able to significantly reduce ΔT_{j}. Also in this thesis, the design and development of a liquid metal heat sink for press–pack IGBTs (PPIs) is proposed. Traditionally, water is used for cooling PPIs in high–power applications. However, ionised particles are developed in the cooling system that contribute to the corrosion of the piping system. Therefore, the use of a thermal management system based on liquid metal increases the heat dissipation capability without corroding the cooling structure. Analytical work is performed on the design of both heat sinks and the implementation of the temperature control method. The thermal performance of both heat sinks, as well as the adaptive heat sink control, are experimentally validated.

To my family for their endless support, patience and love.

Acknowledgements

First and foremost I would like to express my sincere gratitude to my supervisor, Prof. Volker Pickert, for his continuous guidance and support. The successful completion of this research project would not have been possible without his encouragement and motivation. I am very grateful for having the opportunity to work with him and gain from his broad knowledge and methodical thinking. Also, I would like to thank Dr. Bing Ji and Prof. Wenxian Song for their useful advice and guidance throughout various stages of the project.

Many thanks go to the technical support staff within the department of Electrical and Electronic Engineering; Allan, Jack, John, and Sam for helping with the construction of the equipment and Jeff and Paul for helping with the electronic circuits construction. Also, I would like to thank Gordon and James for their help and guidance.

Special thanks are due to the people that made life enjoyable in the UG Lab; Nicola, Iago, Ari, Raihan, and Reza, just to name a few. I am grateful for being surrounded and supported by some great friends during my PhD journey.

My deepest appreciation goes to my parents, Prokopis and Yianna, for their constant support and encouragement in every step of my life. Special thanks go to my brother, Constantinos, for tolerating me and being a good flatmate for the past 4 years.

Last but not least, I would like to thank Stefani for standing by my side and supporting me in everything I do. Her endless patience and support mean the world to me.

Contents

List of figures

List of tables

Nomenclature

Acronyms

AC	Alternating current
ADC	Analog–to–digital converter
CFD	Computational fluid dynamics
CPU	Central processing unit
CTE	Coefficient of thermal expansion
DCB	Direct copper bonded
DC	Direct current
DCJ	Dual–piezoelectric cooling jet
DUT	Device under test
EHD	Electrohydrodynamics
EMF	Electromotive force
FEA	Finite element analysis
HEV	Hybrid electric vehicle
IGBT	Insulated–gate bipolar transistor
LED	Light emitting diode
LFV	Lorentz Force Velocimetry
MHD	Magnetohydrodynamics
PCB	Printed circuit board

PCM	Phase change material
PPI	Press–pack insulated–gate bipolar transistor
RUL	Remaining useful lifetime
TEC	Thermoelectric cooling
TIM	Thermal interface material
TSEP	Temperature sensitive electrical parameter

Roman Symbols

A	Area
$\mathbf{B}$	Magnetic field strength
B_{eff}	Efficient magnetic flux density
B_{u}	Systematic uncertainty
C_{p}	Specific heat capacity
$\mathrm{C_{th}}$	Thermal capacitance
C_{v}	Volumetric heat capacity
$\boldsymbol{E}$	Electric field
E_{a}	Activation energy
$\mathbf{F}$	Lonentz force
f_{s}	Switching frequency
h	Heat transfer coefficient
Ha	Hartmann number
$\mathrm{I_C}$	Collector current
$\mathrm{I_D}$	Current amplitude per bond wire
$\mathrm{I_{heat}}$	IGBT self–heating current
$\mathrm{I_{pump}}$	MHD pump current
$\mathrm{I_{sense}}$	Sense current for temperature measurement

$\mathbf{J}$	Current charge density
k	Thermal conductivity
k_{B}	Boltzmann constant
L	Length
N	Stuart number
N_{a}	Avogadro constant = $6.022 \cdot 10^{-23}\,\mathrm{mol}^{-1}$
$\mathrm{N_f}$	Cycles to failure
p	Pressure
$\mathrm{P_{avg}}$	Average power losses
$\mathrm{P_{cond}}$	Conduction losses
P_{MHD}	MHD pump pressure head
$\mathrm{P_{pump}}$	MHD pump power consumption
P_{s}	Static pressure
$\mathrm{P_{sp}}$	Single power loss pulse
$\mathrm{P_{sw}}$	Switching losses
P(t)	Power losses
$\mathrm{P_{on}}$	Turn-on losses
$\mathrm{P_{off}}$	Turn-off losses
Q	Volumetric flow rate
q	Heat
q_{x}	Heat transfer rate
R	Ideal gas constant = $8.314\,\mathrm{J}/(\mathrm{K}\cdot\mathrm{mol})$
Re	Reynolds number
Re_{m}	Magnetic Reynolds number
$\mathrm{R_{th}}$	Thermal resistance

T	Temperature
T_{amb}	Ambient temperature
T_{g}	Glass transition temperature
T_{hs}	Heat sink temperature
T_{j}	Junction temperature
T_{j}^{*}	Actual junction temperature
$T_{\text{j-max}}$	Maximum operating junction temperature
T_{lm}	Liquid metal inlet temperature
T_{max}	Maximum junction temperature
T_{min}	Minimum junction temperature
T_{m}	Mean junction temperature
T_{ref}	Reference junction temperature
ΔT_{j}	Junction temperature swing
t_{on}	Pulse duration
$\mathbf{u}$	Velocity
u_{t}	Overall uncertainty
$\text{V}_{\text{CE-on}}$	On–state voltage
x	Number of samples
Z_{th}	Transient thermal impedance
Z_{thjc}	Junction–to–case thermal impedance

Greek Symbols

α	Heat spreading angle
ε_0	Vacuum permittivity
μ	Dynamic viscosity
μ_0	Vacuum permeability

ρ	Volumetric mass density
ρ_e	Charge density
σ	Electrical conductivity
σ_d	Standard deviation
τ_{MHD}	Liquid metal heat sink time constant
τ_{th}	Thermal time constant

Chapter 1

Introduction

Power semiconductor devices are key components for power conversion in a wide range of domestic and industrial applications due to their efficiency and performance. They are the bridge connecting signal and high–power devices. The semiconductor industry has flourished over the last two decades, as the utilisation of power electronic devices has been adopted in almost any power conversion application. Among the reasons that helped in establishing power switching devices as the workhorse are mainly the development of semiconductors than are able to provide fast switching while handling high power levels, and the evolution in the control field.

The global initiative toward the exploitation of renewable energy sources [**?**] and electrification of transport [**?**] pushes the demand for more power electronic devices. As shown in Fig. 1.1, the market size of power devices has been increasing steadily in the past years and it is forecast

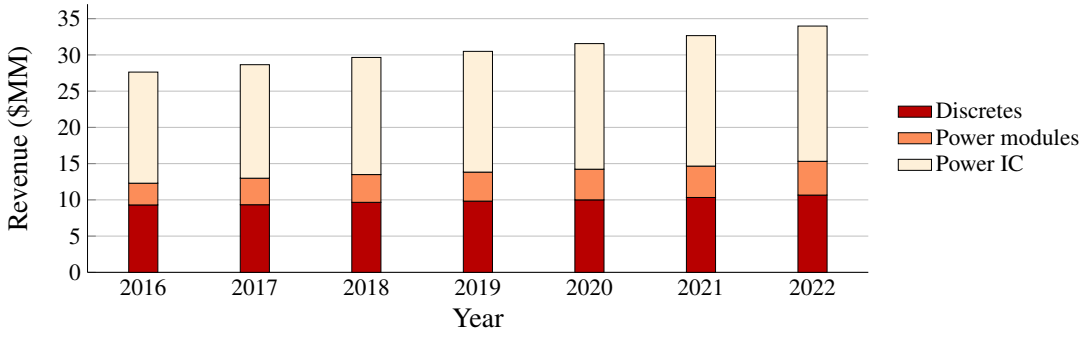

Fig. 1.1. Power electronics market for 2016–2022.

that it will grow even further in the foreseeable future [**?**]. Consequently, power electronics are overtaking existing technologies for a multitude of applications; including some that demand high reliability and safe operation on a system level.

1.1 Background and motivation

One of the power semiconductors that is mostly used in medium–to–high power applications is the insulated–gate bipolar transistor (IGBT). IGBTs are used in a variety of applications and operate within a broad range of voltage and current levels, as shown in Fig. 1.2 [**?**]. Although these devices are extremely efficient, the losses for such high power levels will generate a remarkable amount of heat that needs to be dissipated to another medium before the junction temperature (T_j) of the IGBT exceeds its operational boundaries.

Following the Moore's law trend, IGBT dies are shrinking in size and increasing in power rating simultaneously. Therefore, the heat flux generated by the power losses is substantial and often requires advanced thermal management solutions to maintain the junction temperature below its maximum operating point ($T_{j\text{-max}}$) that can be between 125–175 °C, depending on the

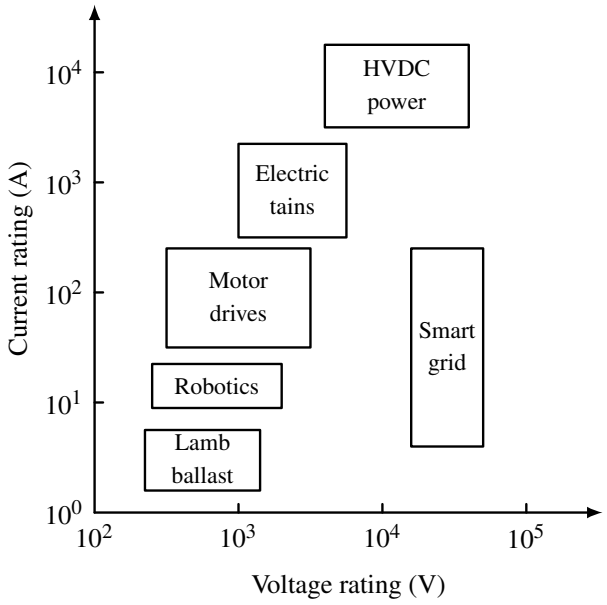

Fig. 1.2. IGBT application spectrum.

IGBT generation. Thermal design of power electronic systems is often overlooked and is only considered as an afterthought once a problem arises. However, this approach often leads to oversized cooling systems that reduce the overall system power density.

The design of a power converter is often associated with application–specific constraints regarding its physical parameters. For example, the weight of power converters used in transportation, including railway, aerospace, and electric vehicle applications, should be reduced in order to improve the power–to–weight ratio. In addition, the volume of the power converter is also a critical factor. Considering an electric vehicle, the power converter should fit under the bonnet that has restricted space, along with the other components of the drivetrain. The weight and volume of the thermal management system for the power converter in all the aforementioned applications is equally important; thus, the design of a cooling system that has a small form factor and is able to dissipate the high heat fluxes of modern power electronics is crucial.

Also, modern power electronics utilised in harsh environments, such as oil and gas drilling, as well as shipboard and airborne military applications, are operating at elevated ambient temperatures. Thus, powerful heat dissipation mechanisms are required in order to avoid thermal runaway. Currently, modern power electronics are expected to experience heat fluxes of around 100–150 $\mathrm{W/cm^2}$ under normal operating conditions, which is expected to rise to 500 $\mathrm{W/cm^2}$ in the foreseeable future, given the current trend in power electronics applications.

1.2 Liquid metal cooling for electronics

Liquid metals have gained attention in the past few years for electronics thermal management. They have excellent thermophysical properties, including very high thermal conductivity and low melting point. In addition, they own very high electrical conductivity; an important attribute for driving the fluid with an electromagnetic pump without any moving parts [**?** **?**]. Comparisons between liquid metal and water for mini– and micro–channels show that liquid metal can achieve up to 40% reduction of the heat sink's thermal resistance [**?**]. Moreover, heat fluxes greater

than 1500 W/cm^2 have been successfully dissipated [**?**]. Therefore, liquid metals are ideal for applications where high heat fluxes need to be dissipated and high reliability is required.

The design and development of thermal management systems based on liquid metal for central processing units (CPUs) has been reported on multiple occasions in the past decade, demonstrating significant increase in the cooling performance compared to commercial heat sinks [**? ? ? ?**]. Liquid metal heat sinks have also been utilised for cooling high–power laser diodes and adjusting their wavelength by controlling the coolant's flow rate [**?**]. Moreover, they have been used for cooling high–power light emitting diodes (LEDs) [**?**]. Liquid metals are also ideal for integrated cooling mechanisms for electronic devices in spatial restricted applications with local hotspots [**?**], as well as an alternative to heat pipes utilised as heat spreaders for orientation sensitive applications [**?**]. In addition, a liquid metal coolant has been proposed for reducing the weight of the power electronic cooling system for an aerospace application while maintaining similar cooling performance, in spite of its higher density [**?**]. Experimental investigations of liquid metal mini–channel heat sinks aimed at power electronic applications have been reported on a few occasions, however, the experimental validation is performed by using power resistors rather than power electronic devices [**? ?**]. Although that approach gives a good indication of the heat sink's thermal performance, the temperature transient of the electronic device that depends on its internal layers can not be emulated.

As liquid metals are considerably more expensive than other cooling mediums, the cost of a pure liquid metal cooling system can be rather high. In order to develop a more cost–effective thermal management system without compromising the cooling performance, liquid metal has been used as an intermediate stage for dissipating the excess heat of power converters in hybrid electric vehicles (HEVs). As the cooling loop of power electronics in HEVs is often shared with the internal combustion engine, thus leading to elevated fluid temperatures, liquid metal has been used to dissipate the excess heat of the power electronics to the main cooling loop [**?**]. An alternative solution to reduce cost for liquid metal cooling applications involves the use of a liquid metal droplet that activates the circuilation of a secondary fluid through a variable frequency signal based on the Marangoni effect, which is defined as the mass transfer across an interface between two fluids due to surface tension difference [**? ?**]. Despite that the majority of

Table 1.1. Thermophysical properties of various fluids used for power electronics cooling.

Property	Unit	$Ga_{68}In_{22}Sn_{10}$	Mercury	Water	Ethylene glycol*
Density	kg/m^3	6400	13593	998	1107
Melting point	°C	-19	-38.89	0	-52.8
Boiling point	°C	>1300	357.3	100	111.1
Specific heat capacity	$J/(kg \cdot °C)$	365	140	4081	3284
Volumetric heat capacity	$J/(°C \cdot m^3)$	$2.34 \cdot 10^6$	$1.9 \cdot 10^6$	$4.07 \cdot 10^6$	$3.63 \cdot 10^6$
Dynamic viscocity	$Pa \cdot s$	0.0024	0.0017	0.001	0.009
Electrical conductivity	S/m	$3.46 \cdot 10^6$	$1 \cdot 10^6$	$5.5 \cdot 10^{-6}$	$3.2 \cdot 10^{-6}$
Thermal conductivity	$W/(m \cdot °C)$	16.5	8.2	0.606	0.52
Prandtl number	—	0.027	0.013	6.62	23.2

* The physical properties of the fluid are based on a 60/40% ethylene glycol/water mixture.

liquid metal cooling applications use externally supplied electromagnetic or peristaltic pumps to drive the coolant, the excess heat can be harvested in order to drive an electromagnetic pump via a thermoelectric generator [**?**] or by exploiting the thermosyphon effect [**?**].

Table 1.1 provides a comparison between $Ga_{68}In_{22}Sn_{10}$, mercury, water, and a 60/40% ethylene glycol/water mixture. Water and ethylene glycol are commonly used for single phase cooling of power electronics, however, they require a conventional liquid pump for driving the fluid that relies on moving parts and can compromise the reliability of the cooling system. In addition, the thermal conductivity of liquid metals is much higher and can therefore achieve higher heat flux removal, in spite of the lower volumetric heat capacity. On the other hand, mercury can be used for cooling applications, however, compared to $Ga_{68}In_{22}Sn_{10}$ it has about half of its thermal conductivity and lower volumetric heat capacity. Also, it is a toxic material that requires extra precautions when used. Considering the advantages and disadvantages of each cooling medium, $Ga_{68}In_{22}Sn_{10}$ can provide high cooling performance and be driven through a reliable, non–moving pump, and is therefore selected for this study.

1.3 Contribution to knowledge and published work

The presented work in this thesis investigates the use of liquid metal as a heat transport agent for power electronic applications. Past research suggests that liquid metals are good candidates

for power electronics cooling, however the design and implementation of liquid metal heat sinks aimed at power electronics thermal management has not been investigated extensively. As mentioned earlier, the selected liquid metal coolant has high electrical conductivity, which is required for pumping the fluid using an electromagnetic pump that has no moving parts and thus, improves the reliability of the system by reducing the possibility of failure in the cooling system. Also, the cooling capability of the system can be very high, as heat fluxes as high as $1500\,\mathrm{W/cm^2}$ have been reported to be removed successfully. Compared to water–based systems $Ga_{68}In_{22}Sn_{10}$ has been able to achieve a 40% reduction in the thermal resistance of the system [**?**]. The areas of work where this thesis is scientifically contributing are listed as follows:

- The design, development and implementation of a magnetohydrodynamics (MHD)–driven liquid metal heat sink used for thermal management of IGBT power modules. The pump is positioned under the chip and the coolant contacts the baseplate of the power module directly; two parameters that contribute in achieving local cooling. The thermo–fluid simulation of the heat sink is experimentally validated.

- The design and development of a junction temperature control method for IGBT power modules based on the liquid metal heat sink. The proposed method can be implemented in high–power applications without compromising the electrical performance of the electronic device. Based on the adaptive controller, the lifetime of the power module is increased by reducing the temperature fluctuations.

- The design and development of an MHD–driven liquid metal heat sink used for thermal management of press–pack IGBTs (PPIs). The heat sink is driven by the load current, thus, it does not require an external power supply.

The following publications are the results of the work presented in this thesis:

- X. Song, V. Pickert, B. Ji, R. T. Naayagi, C. Wang and Y. Yerasimou, “Questionnaire-Based Discussion of Finite Element Multiphysics Simulation Software in Power Electronics,” in *IEEE Transactions on Power Electronics*, vol. 33, no. 8, pp. 7010–7020, Aug 2018.

- Y. Yerasimou, V. Pickert, B. Ji and X. Song, "Liquid Metal Magnetohydrodynamic Pump for Junction Temperature Control of Power Modules," in *IEEE Transactions on Power Electronics*, vol. 33 no. 12, pp. 10583 - 10593, Dec 2018.

1.4 Thesis overview

This thesis consists of seven chapters. A general introduction on the challenges associated to thermal management of IGBT power electronics is presented in *Chapter 1*. Moreover, a review of various applications where liquid metal is used as cooling medium for electronics is presented. Also in this chapter, the research contribution and published work resulted from this project are included.

The state of the art regarding thermal management methods aimed at power electronic applications is provided in *Chapter 2*. Comparisons for the various methods, as well as for different cooling mediums are also presented.

The governing equations describing the MHD phenomenon are presented in *Chapter 3*. In addition, this chapter includes an overview of typical liquid metal MHD applications, including pumps, generators and flow meters.

The design and development of a prototype liquid metal heat sink for a conventional IGBT power module driven by an MHD pump is presented in *Chapter 4*. In this chapter the development of a Cauer thermal network and the implementation of an electrical method for sensing the junction temperature, T_{j}, of the investigated IGBT power module is shown. Moreover, a finite element model and static experimental results of the heat sink are provided.

A method for extending the lifetime of power electronic devices is proposed in *Chapter 5*. For its implementation, a junction temperature control method based on the dynamic control of the liquid metal flow rate is implemented. Simulation results based on the developed Cauer model and experimental results are provided in this chapter.

A self–driven liquid metal heat sink for PPIs is proposed in *Chapter 6*. The design parameters of the heat sink and a study of the magnetic field in the active channel of the heat sink are presented, as well as experimental results of the heat sink under static heat loads.

Chapter 7 concludes the work and suggests potential areas for further work.

Chapter 2

Thermal management of power electronic devices

Heat is the form of energy that is transferred from an object with high temperature to an object with a lower temperature. In general, there are three physical mechanisms of heat transfer: (i) conduction, (ii) convection, and (iii) radiation. Conduction describes the heat transfer via oscillation of molecules, i.e. direct contact of objects. Similarly, convection describes the heat transfer between a solid and a moving fluid if a temperature gradient exists between the two mediums. The moving fluid can either be a liquid, a gas, or plasma. Finally, radiation is the transfer of heat via electromagnetic waves.

For power electronic applications, the heat dissipated to the ambient via radiation is insignificant and often neglected, unless a natural convection method is used for cooling the electronic components [**?**]. Considering the object in Fig 2.1(a) with surface area A and length L, the heat transfer rate (q_{x}) between T_1 and T_2 is given by the Fourier's law of thermal conduction:

$$q_{\mathrm{x}} = -kA\frac{\partial T}{\partial x} \tag{2.1}$$

where k is the thermal conductivity of the material and $\partial T/\partial x$ is the temperature gradient. It is assumed that the heat flow is one dimensional and $T_1 > T_2$. Similarly, Fig. 2.1(b) shows a flat

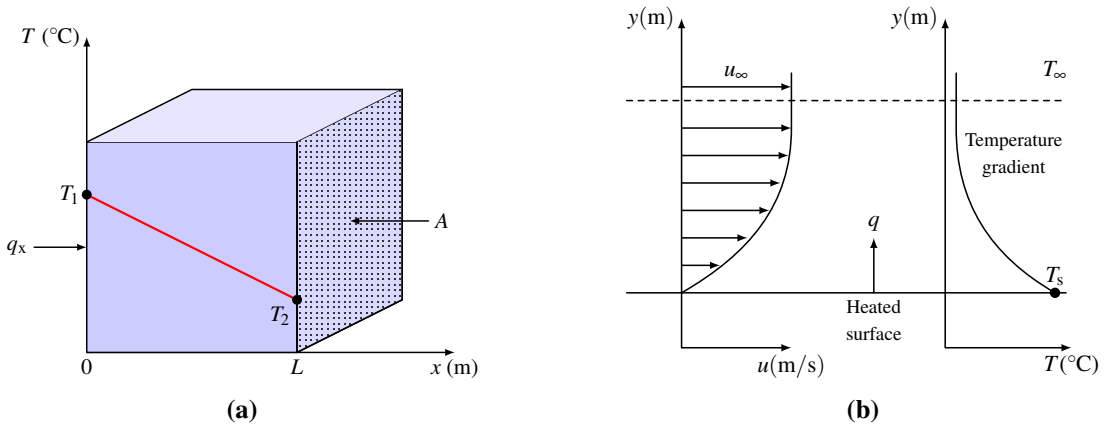

Fig. 2.1. Heat transfer mechanisms: (a) Conduction and (b) convection.

plane of area A and a fluid travelling with velocity u. Along the wall of the object the velocity of the fluid is assumed to be zero, whereas, it reaches free stream velocity (u_∞) as soon as it enters the free stream region. As long as there is a temperature difference between the wall temperatures (T_w) and the free stream fluid temperature (T_∞), heat transfer by convection will occur, described by Newton's law of cooling:

$$q = hA(T_\mathrm{w} - T_\infty) \tag{2.2}$$

where q is the heat and h is the heat transfer coefficient. The heat transfer coefficient h is not a thermophysical property of the fluid but rather depends on the flow channel geometry, flow regime, and the thermophysical properties of the fluid. In most high power applications, forced convection is used for dissipating the excess heat generated by the power semiconductors. The various heat management methods are further discussed in section 2.2.

2.1 Requirement for cooling

The continuing demand in power conversion applications for higher power and further miniaturisation of power electronics packages has led the semiconductor industry towards building high power density chips. Therefore, advanced thermal management solutions should be employed in

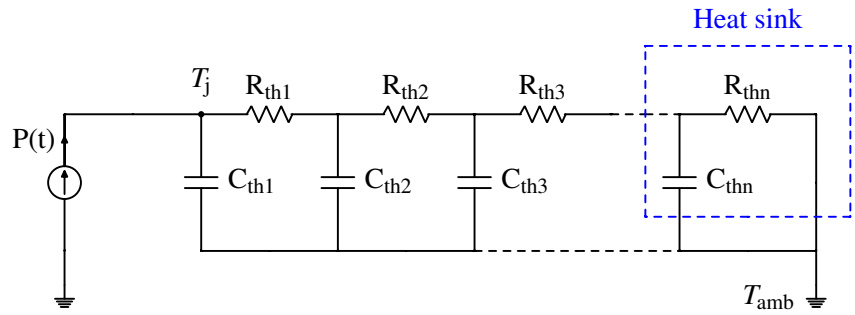

Fig. 2.2. Typical thermal network for power semiconductor.

order to cope with the high heat fluxes generated by the power semiconductor chips and maintain their junction temperature below $T_{\text{j-max}}$.

A simplified ladder thermal network for power electronic devices is illustrated in Fig. 2.2. In order to maintain T_j below the maximum allowable junction temperature of the device, $T_{\text{j-max}}$, the power losses (P(t)) need to be dissipated to the ambient air. The nodes consisting of the thermal resistances R_{th1}-R_{thn-1} and thermal capacitances C_{th1}-C_{thn-1} emulate the layers of the power device and their value is dictated by the layers' material and geometry and is therefore constant. Hence, to reduce the thermal resistance between T_j and the ambient temperature (T_{amb}), the thermal resistance of the cooling system, R_{thn}, should be minimised.

During IGBT's normal operation, the power losses, P(t), generated by the chip itself are the main source of heat. Thermal coupling between adjacent chips could also exist for multichip devices and should also be considered [**?**]. The power losses, P(t), are mainly divided in: (i) conduction losses (P_{cond}) and (ii) switching losses (P_{sw}) that consists of turn-on (P_{on}) and turn-off (P_{off}) losses. Blocking losses that are the product of leakage current and blocking voltage are also present, however, their contribution to the chip heating is negligible for most applications. Therefore, the average power loss (P_{avg}) in the IGBT for a period T, is given by:

$$\begin{aligned} P_{avg} &= P_{cond} + P_{on} + P_{off} \\ &= \frac{1}{T}\int_0^T P(t)\cdot dt \\ &= f_s\left(\left(\int_{tcond} P_{cond} + \int_{ton} P_{on} + \int_{toff} P_{off}\right)\cdot dt\right) \end{aligned} \tag{2.3}$$

where f_s is the switching frequency. The components P_{cond}, P_{on} and P_{off} can be defined as:

$$\int_{tcond} P_{cond} \cdot dt = E_{cond}(V_{CE}, I_C, T_j) = \int_{tcond} V_{CE} \cdot I_C \cdot dt \tag{2.4}$$

$$\int_{ton} P_{on} \cdot dt = E_{on}(V_{DC}, I_{on}, T_j) \tag{2.5}$$

$$\int_{toff} P_{off} \cdot dt = E_{off}(V_{DC}, I_{off}, T_j) \tag{2.6}$$

where V_{CE} is the collector-emitter voltage across the IGBT, V_{DC} is the DC-link voltage and E_{cond}, E_{on} and E_{off} are the energies for conduction, switching on and switching off of the device, respectively. Finally, I_{cond}, I_{on} and I_{off} are the currents during conduction, switching on and switching off periods, respectively. An example voltage and current waveform of an IGBT device with the corresponding loss component for each interval is shown in Fig. 2.3 for a full switching cycle.

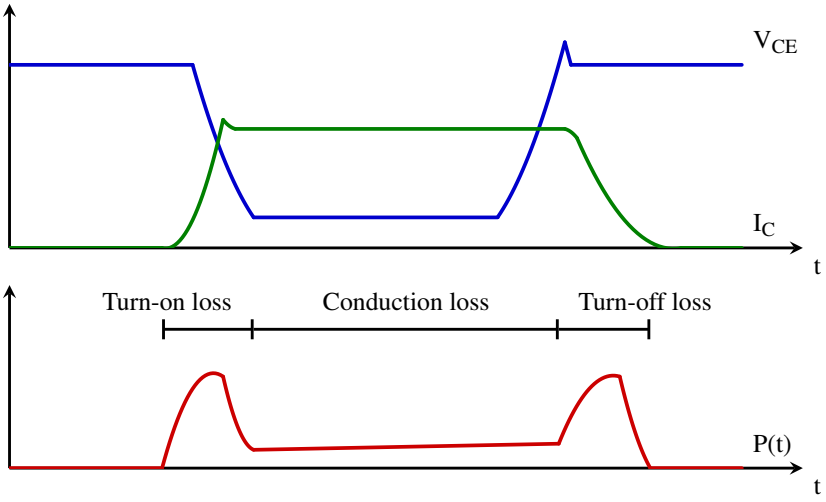

Fig. 2.3. Example power loss waveform for power electronic device.

A study conducted in 2018 indicates that the majority of power conversion failures are associated with power electronics, steering the future research towards their reliability enhancement [**?**]. In addition, according to questionnaire-based survey on industrial power electronic system failures, the power semiconductor devices are the most fragile components of the power system [**?**]. As Fig. 2.4 shows, power modules could fail due to vibrations or shocks, operating

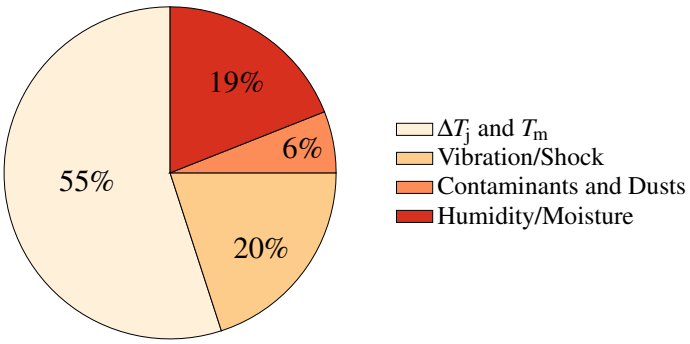

Fig. 2.4. Common failure mechanisms for power electronic devices [**?**].

in a dusty or humid environment, however, the majority of the failures are associated to the junction temperature swing (ΔT_j) and mean junction temperature (T_m) [**?**]. Hence, the design and implementation of efficient and effective cooling system are of paramount importance.

2.2 Overview of power electronics cooling methods

This section presents various cooling methods that are currently employed for thermal protection of electronic devices. The principle of operation, advantages and disadvantages, as well as comparisons of the heat removal performance and consumption ratio of the heat sinks are discussed. The consumption ratio of the cooling system is defined as the ratio of the heat removed and the input power required for the cooling to operate.

2.2.1 Solid state cooling

Solid state cooling uses materials with high thermal conductivity and dissipates heat either via heat conduction or thermoelectric effect. Finned heat sinks, conduction plates, thermal interface materials (TIMs), magnetic cooling and thermoelectric cooling are the most common passive heat dissipation methods applied for power electronics cooling.

The most cost effective method for cooling a power electronic device is by using either an aluminium plate or finned heat sink. A typical passive finned heat sink is shown in Fig. 2.5.

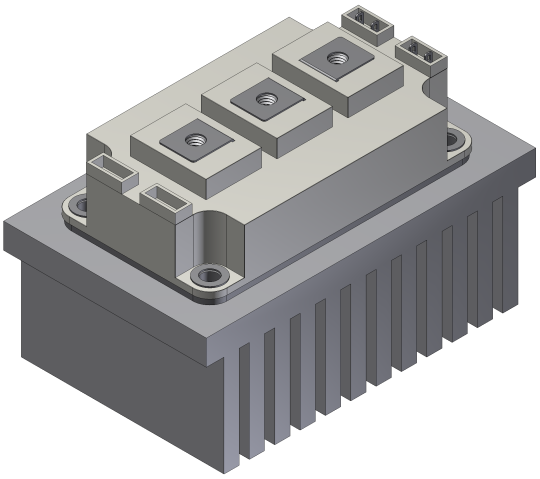

Fig. 2.5. Typical passive finned heat sink for power modules.

Aluminium owns a relatively high thermal conductivity of approximately $205\,\mathrm{W/(m \cdot K)}$. Also, it is cheap and light when compared to other materials used for heat sink structures. However, this cooling method is only limited to low power density applications, as the heat dissipation of such heat sinks is very low. Despite the use of different geometries and fin configurations, such as plate fin, pin fin, and triangular fin, passive aluminium heat sinks can only dissipate heat fluxes less than $1\,\mathrm{W/cm^2}$. Copper could also be utilised, as it has a thermal conductivity of about $385\,\mathrm{W/(m \cdot K)}$, however, the selection of copper over aluminium would drive up the cost and weight of the heat sink without substantial improvement of the heat transfer coefficient (U-value) [**?**].

In addition to the heat sink, heat spreaders are used, that aim in increasing the contact surface area between the baseplate of the power module and the heat sink. The purpose of heat spreaders is to increase the existing heat transfer coefficient of the cooling mechanism [**?**]. Moreover, TIMs are used between the baseplate and the heat spreader to ensure that there are no air gaps between the two surfaces that will increase the contact thermal resistance. The schematic of TIM application is shown in Fig. 2.6. Although that with the addition of TIM the contact thermal resistance between the baseplate and the cooling medium is significantly decreased, it is not completely eliminated. Hence, further development of TIM applications in the last decade has led to the use of liquid metals as substitute to the traditional thermal grease because of their high thermal conductivity [**?**].

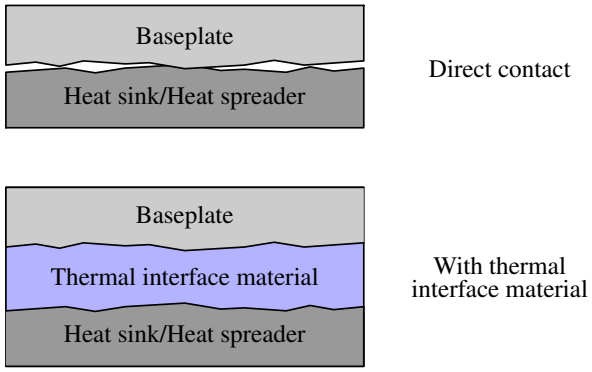

Fig. 2.6. Schematic of thermal interface material application.

The research of advanced solid conduction has led to the fabrication of alloys that own higher thermal conductivity, are lighter and more compact than aluminium and copper. Applications such as aerospace and satellite often impose constraints such as weight and volume. In addition, in some instances, the use of active cooling is not favourable due to reliability issues. Hence, the research for cooling applications for these sectors is steered towards advanced materials that own thermal conductivities of up to $1.9\,\mathrm{kW}/(\mathrm{m}\cdot\mathrm{K})$. In addition, these materials have increased thermal diffusivity; a property that also contributes to increasing the heat transfer coefficient of the cooling device. Thermal diffusivity is described as the ratio of the thermal conductivity to the density multiplied by the specific heat capacity of the material. Nonetheless, the fabrication of conduction plates and heat spreaders with such materials is challenging as the heat spread is two–dimensional. In combination with the significant increase in cost, the thickness of the material should be minimised [**?**].

Magnetic cooling is another passive cooling method. Its principle of operation is based on the magnetocaloric effect, where a change in temperature is achieved when magnetocaloric materials experience a variable magnetic field. Although it is mainly used for refrigiration systems, motor cooling, pumps, and heat exchangers, it has been recently considered for electronics and nanoelectronics cooling applications with volume and weight restrictions, as well as for applications that require high cooling consumption ratio [**?**].

Finally, thermoelectric cooling (TEC), which is based on the Pielter effect, is a passive cooling method that has been used for numerous cooling applications. As Fig. 2.7 shows, a negative temperature gradient is generated between two materials when a direct current (DC) flows

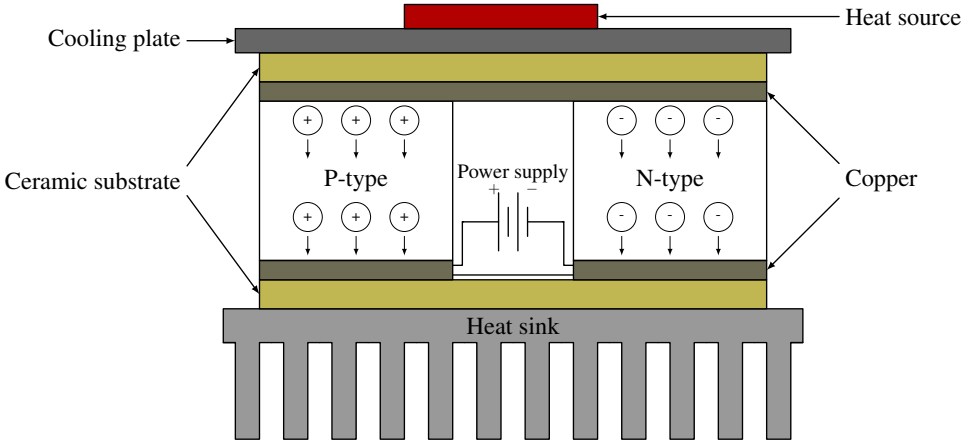

Fig. 2.7. Working principle of thermoelectric cooling.

between two semiconductors. The implementation of TEC devices, often referred to as solid–state heat pumps, in the power electronic area has been proposed due to the absence of moving parts, silent operation, precise temperature control and small form factor compared to air cooling technologies. However, the consumption ratio of the cooling system is very low. Also, in addition to the heat that needs to be dissipated from the heat source, TECs need to dissipate the heat that is generated from its own power, which reduces their overall heat dissipation capability to less than 150 W with low heat fluxes. Because of these limitations, thermoelectric cooling is not a good candidate for many applications, especially for high–power electronic devices [**?** **?**]. Thermotunneling and thermionic cooling are extensions of TEC applied in nanoscale, such as tunnel and thermionic effects. They are promising cooling methods, as the use of complex structures, such as nanotubes and heterostructures, increases the consumption ratio of the cooling system [**?** **?**]. Thermotunneling is based on the same principle as thermoelectric cooling, however, it is applied in narrow tunnel junctions where the transport of electrons aids in a temperature grade in the tunnel. Similarly, thermionic cooling is based on the behaviour of hot electrons emitting from the cathode surface and thus, absorb heat from it.

2.2.2 Air cooling

The heat transfer coefficient of cooling systems can be increased with the use of gas fluid as a heat transfer agent. Air cooling is one of the most common methods for cooling power electronic

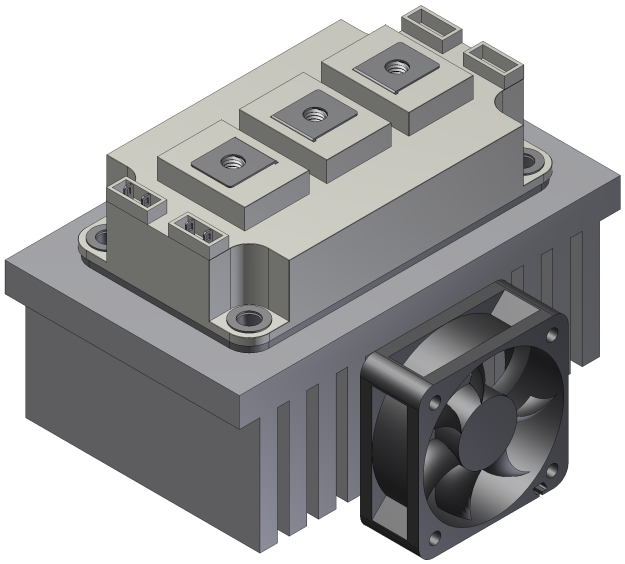

Fig. 2.8. Typical forced-air cooled heat sink.

devices, as the complexity of the heat sink is significantly reduced compared to liquid and two–phase cooling technologies. The various air cooling methods, their performance, advantages and disadvantages will be discussed in the following paragraphs.

The simplest form of air cooling is natural (or free) convection . The power semiconductor is often attached to a heat sink in a similar configuration to Fig. 2.5 and the heat is dissipated to the ambient air because of the density variation caused by temperature gradients in the air itself. It is a passive cooling method, as no external mechanisms are utilised to pump the fluid. Natural convection can only dissipate a few watts of heat and is not suitable for high power applications.

The heat transfer coefficient of the cooling system can be dramatically increased with the introduction of forced–air. The implementation of a forced–air cooling system is simple; the power module is attached on a finned heat sink and a fan blows air along the fins. A typical example of forced–air cooled power module is shown in Fig. 2.8. This cooling method is the most popular for power electronic applications, where the heat load is no more than 200 W, as it is cheap, can deliver high cooling consumption ratio and the level of complexity is much lower than liquid cooling methods. However, in order to achieve high heat transfer coefficients, the weight and volume should be significantly increased, thus leading to poor power density of the overall system [**? ?**].

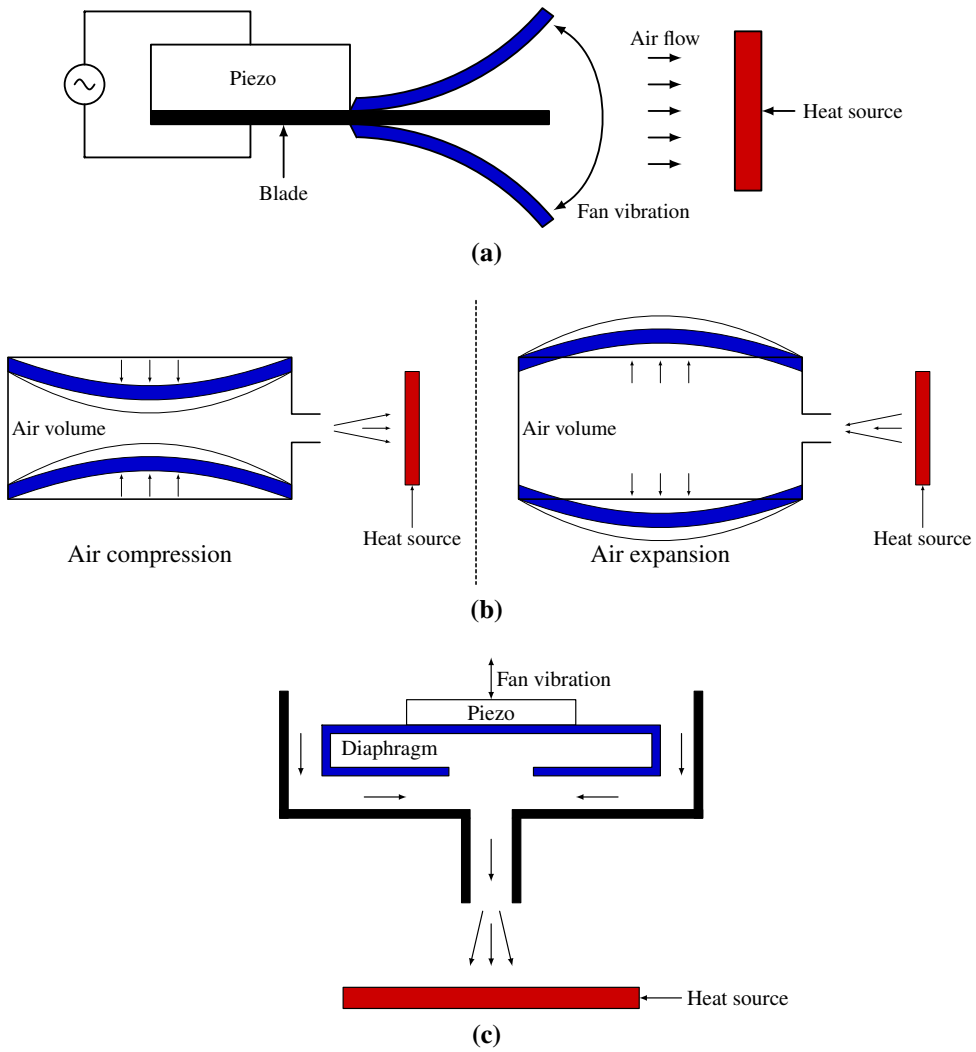

Fig. 2.9. Working principle of piezoelectric coolers: (a) Piezoelectric fan (b) dual piezoelectric cooling jet and (c) piezoelectric microblower.

Another type of forced–air heat dissipation is piezoelectric cooling, which utilises the piezoelectric effect instead of a fan to generate air flow. There are three main types of piezoelectric cooling devices in electronics cooling applications: (i) piezoelectric fans, (ii) dual-piezoelectric cooling jets (DCJ) and (iii) piezoelectric microblowers. The principle of operation of the different piezoelectric cooling devices is shown in Fig. 2.9. The piezoelectric fan, shown in Fig. 2.9(a), generates vibrations through a piezoelectric transducer attached to a cantilever, which causes the air flow. Since the amplitude of motion is tiny, a blade is attached that amplifies it and increases the air flow volume [**?**]. Similarly to the piezoelectric fan, DCJs shown in Fig. 2.9(b) use piezo components that when actuated by alternating current (AC) power expand and contract

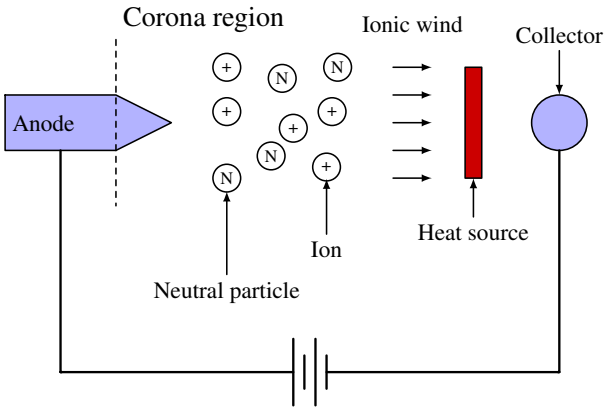

Fig. 2.10. Working principle of EHD cooling.

simultaneously, thus generating air flow [**?**]. Finally, a piezoelectric microblower uses a piezo device that generates vibrations on a diaphragm. As Fig. 2.9(c) shows, the vibration causes air flow through a nozzle that can be used for dissipating power from a heat source. All the presented piezoelectric cooling methods have high cooling consumption ratio, low noise and high reliability, however, they can only be used for low power applications, as they are unable to dissipate high heat fluxes.

Synthetic jet impingement has similar principle of operation to piezoelectric microblowers. A diaphragm, that is either magnetically or electrically controlled, generates turbulent air flow, which results in enhanced heat transfer coefficient. The main advantages of this cooling technique are silent operation, high reliability because of the lack of moving parts, low power consumption, and compactness. Nonetheless, its use is only limited to low power applications [**?**].

Electohydrodynamics (EHD) convert electric energy to kinetic energy in the form of fluid flow. Unlike traditional air cooling technologies, that convert mechanical energy by using a fan to generate air flow, electrohydrodynamic cooling devices make use of the corona effect to generate ionic air streams. The working principle of EHD cooling is shown in Fig. 2.10, where voltage between the anode and the cathode generates a high electric field that ionises the neighbouring air molecules. The ionised molecules are moving within the electric field and in their turn transfer momentum to the neutral molecules, thus generating air flow. EHD cooling has been successfully used for dissipating heat in laptops [**?**] and LEDs [**?**]. The most important benefits of EHD cooling are silent operation, increased reliability due to the absence of moving parts, freedom

over geometry and design, and precise control over the air velocity. On the other hand, high voltages are required for their operation and wear of the electrodes occurs over time due to the corona effect.

Thermoacoustic devices are based on the thermoacoustic effect and have the ability to either generate sound out of heat or pump heat by utilising sound. The operation of thermoacoustic cooling devices is based on generating high–amplitude sound waves that creates pressure changes in a resonator. Hence, the travelling air wave within the housing of the device, which is used for dissipating heat from one medium to another, is controlled by the sound intensity. This method shares many of the advantages of EHD cooling, such as silent operation, increased reliability due to the absence of moving parts, and simplicity in construction. Nonetheless, it is incapable of removing high heat fluxes and thus, unsuitable for high power applications [**?**].

2.2.3 Liquid cooling technologies

Solid state and air cooling methods mentioned earlier often offer easy and reliable implementation of power electronic devices' cooling, however, when considering high power density application, where heat fluxes exceed $100\,\mathrm{W/cm^2}$, liquid cooling is preferred [**?** **?**]. Liquids in general have superior thermophysical properties compared to air, such as higher thermal conductivity and volumetric heat capacity (C_v) and can therefore achieve higher heat transfer coefficients. In addition, the volume, weight and noise of the heat sink can be significantly reduced. Nonetheless, the complexity of the heat sink manufacturing is increased, as hazards such as fluid leakage and piping corrosion exist and should be considered in the design process. Additional precautions should be taken when working with coolant agents that possess high toxicity, are electrically conductive or flammable. Liquid coolants can be utilised to dissipate heat in various ways and can be classified in three categories depending on their electrical conductivity: (i) liquids with dielectric properties that allow direct immersion of the electronics, (ii) liquids that own very low (albeit not zero) conductivity that will not damage the electronics in case of contact, and (iii) liquids with conductivity high enough that will damage the electronics in case of contact [**?**]. In addition, liquid cooling can be split in two categories, depending whether a direct contact

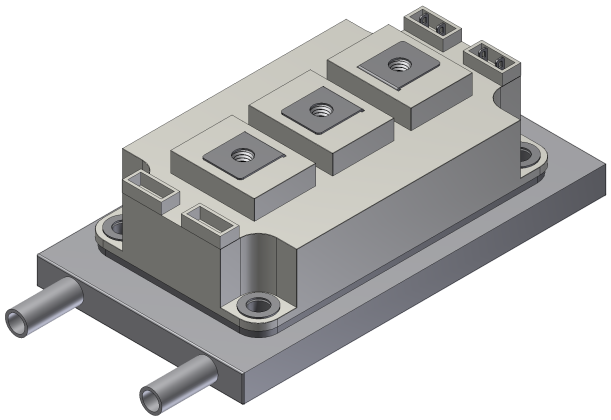

Fig. 2.11. Typical cold plate for power modules cooling.

between the power electronic device and liquid exists, or there is a wall present between them. Examples of the former are electrowetting, immersion and jet impingement, whereas cold plates are a form of indirect liquid cooling.

The implementation of liquid cold plates for power electronics thermal management is the simplest form of liquid cooling. The pipes that contain the fluid are commonly routed in a meander structure and housed in a solid body made of aluminium or copper [**?**]. As the liquid is acting as a heat transport agent, the excess heat is dissipated to a heat exchanger and finally, to the ambient air. A typical cold plate for power modules cooling is shown in Fig. 2.11. Despite the simplicity and superior heat dissipation properties compared to forced-air cooling, standard cold plates are not able to dissipate heat fluxes in excess of $300\,\mathrm{W/cm^2}$. Consequently, continuous development of cold plates that focused on increasing the heat transfer coefficient and therefore, further enhancing liquid cooling effectiveness by increasing the contact surface of the coolant has led to the introduction of techniques such as mini–channel [**?**] and micro–channel [**?**] based heat sinks. The term mini– and micro– defines that hydraulic diameter of the channel, which can be between a few µm and several hundreds of µm. Mini–channel and micro–channel cooling methods are able to cope with heat fluxes as high as $1000\,\mathrm{W/cm^2}$. They have managed to increase the heat transfer coefficient and cooling consumption ratio of the system at the cost of increased pressure drop within the piping system, which forces the use of more powerful pumps or the integration of micropumps. These technologies allow the use of other cooling mediums than water and oil, such as nanofluids [**?**] and room temperature liquid metals [**?**].

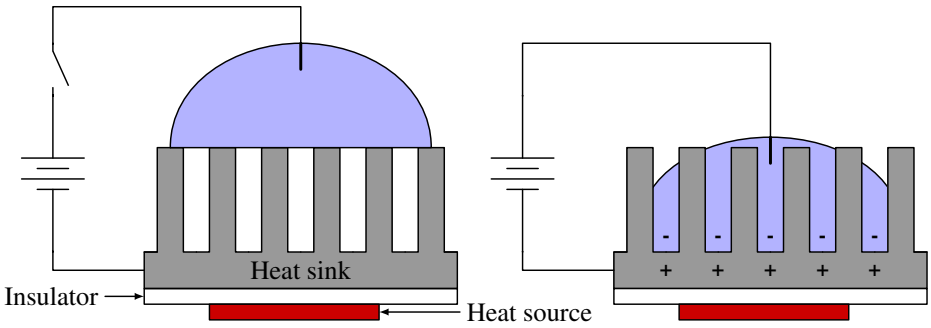

Fig. 2.12. Working principle of electrowetting cooling.

Another form of heat extraction via liquid cooling is electrowetting . It is based on the phenomenon where an electric field can alter the shape of a liquid droplet by modifying the surface tension force. Fig. 2.12 shows the working principle of this cooling method. As an electric field is applied between the liquid and the substrate, the shape of the droplet expands, thus increasing its contact surface area. This cooling method has the ability to remove high heat fluxes while consuming little power. Hence, the consumption ratio of the cooling system is very high. Typically, deionised water, liquid electrolytes, and liquid metals are used as working fluids [**?** **?**].

In addition, immersion is another form of liquid cooling. The electronic devices are submerged in a bath of liquid, thus providing direct contact between the coolant and the heat source. This method can either be classified as natural convection or forced convection, depending on whether a pump is used to generate fluid flow. Also, it can either be single–phase or two–phase cooling based on whether the boiling point of the fluid has been reached. Although the consumption ratio of the cooling could be very high, as high heat fluxes could be removed at very little to none cooling power, non–electrically conductive fluids are required [**?** **?**].

Finally jet impingement is a cooling method where high speed jets of liquid are driven towards the heat source, thus creating a thin boundary layer that contributes in achieving high heat transfer coefficient. As illustrated in Fig. 2.13, jet impingement is either structured as free surface with the jet interacting with air before hitting the surface, or submerged, where the jet remains within the liquid the whole time. An extension of submerged jet impingement is confined jet impingement, where the jet is driven through predefined narrow channels. Depending on geometry and fluid flow parameters, jet impingement techniques can dissipate heat fluxes in

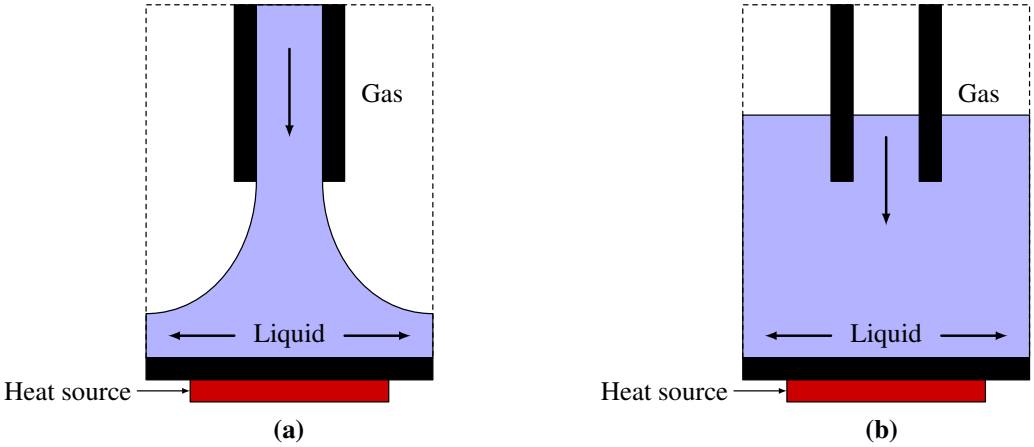

Fig. 2.13. Jet impingement: (a) Free surface and (b) submerged jet.

excess of 1000 W/cm^2 at a very high cooling consumption ratio. This type of cooling is often expensive, as bespoke heat sinks should be designed in order to meet the needs of the specific application [**? ?**].

2.2.4 Two-phase cooling techniques

Two–phase cooling is described as the method where the working fluid changes phase, for example from liquid to gas and vice versa. Some of the methods reviewed in section 2.2.3 also change phases throughout the cooling process, however, it is a by–product of their operation and were not designed as two–phase cooling mechanisms. The main benefits of two–phase cooling compared to single–phase is the reduction in volume, weight and cost, while maintaining, or even increasing, the performance in heat dissipation and cooling consumption ratio. The main disadvantage of this type of cooling is the increased complexity in designing and manufacturing the heat transfer mechanism. In addition, many methods utilise toxic fluids that could be dangerous in case of a spillage or a leakage.

Heat pipe is the best known two–phase heat transport mechanism. It is a passive cooling device, as there is no external mechanism to generate the fluid flow. Heat pipes can be found in a large spectrum of applications; from laptops to nuclear reactors cooling [**? ?**]. The working fluid is often water, ammonia or alcohol. The working principle of a heat pipe is described in Fig. 2.14.

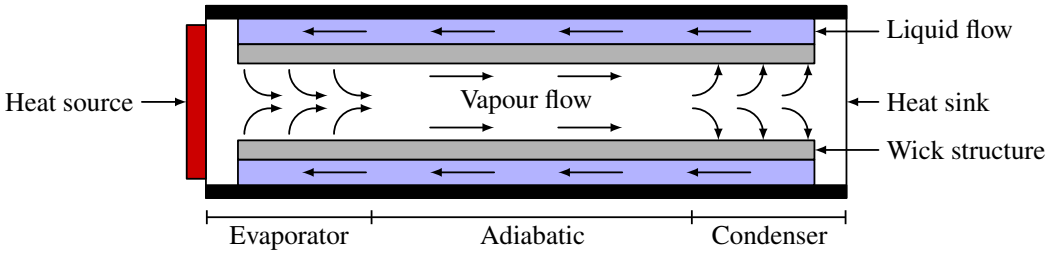

Fig. 2.14. Working principle of heat pipe.

It consists of three different bodies: (i) the heat sink container, (ii) the wick structure, and (iii) the fluid. Also, it is divided in three parts: (i) the evaporator, (ii) the adiabatic section, and (iii) the condenser. The heat pipe begins the cooling process when the heat source boils the fluid and at the point where the evaporation process starts, the heat is dissipated from the heat source to the vapour. Then the vapour transports the heat to the condenser, where it is dissipated to another medium and finally, to the ambient air. The working fluid returns to its liquid phase in the condenser and is pumped back to the evaporator via capillary action in the wick structure. Although heat pipes are able to achieve very high thermal conductivities, ensure high reliability and long lifetime service and can cope with high heat fluxes, their main disadvantage is that they are position–sensitive and therefore their cooling capability is dramatically decreased when used against gravity.

Many variants of heat pipe implementations exist, such as thermosyphons, vapour chambers and loop heat pipes. Thermosyphons base their operation solely on gravity. The heat is collected at the bottom and is transported to the top, where it is dissipated to another medium. Vapour chamber is a flat type of heat pipe, able to achieve heat transfer in two dimensions. Finally, loop heat pipes utilise external fluid pumps to increase the cooling effectiveness and decrease the effect of gravitational forces.

Spray cooling is also utilised when high heat fluxes need to be removed. A spray can either be classified as pressure or atomised, depending on the nature of operation. The former uses high pressure in the liquid flowing through the nozzle, whereas the latter uses air flow of high pressure that breaks the liquid into small droplets as they contact the heat source. Fig. 2.15 shows the working principle of a spray cooling heat sink. Although it shares some of the characteristics of free surface jet impingement, the heat transfer coefficient of spray cooling is higher. The reasons

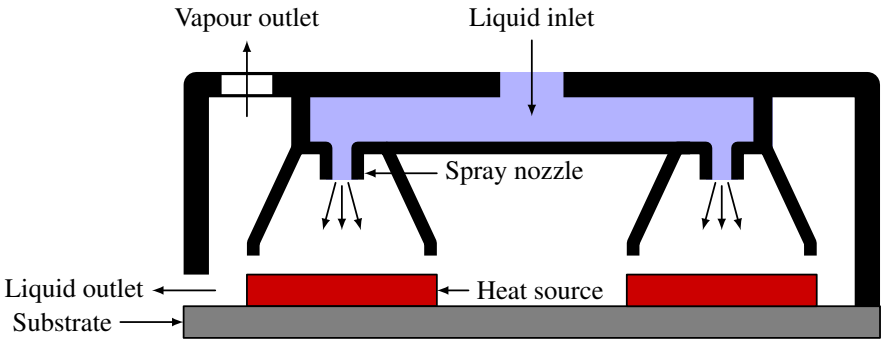

Fig. 2.15. Working principle of spray cooling.

are that large amounts of heat are dissipated because of the latent heat absorbed during the evaporation. Moreover, as the fluid comes in direct contact with the heat source, heat spreading material is not required and therefore, the overall contact thermal resistance is significantly reduced. Despite the increased cooling performance spray can offer, the implementation of this method in power electronics applications is challenging, as the fluid should be dielectric to avoid short circuiting, which would cause catastrophic failure of the devices. Moreover, there is a risk of liquid layers building on the electronic surface that will increase the thermal resistance of the system or the development of corrosion in the device [**?** **?**].

Finally, the use of phase change materials (PCM) for cooling electronic devices is based on the fact that certain materials are able to release or store heat during phase change (i.e. from solid to liquid and vice versa) at a specific temperature. PCM cooling is a passive heat dissipation method, however due to its ability to change phases and store and release heat, the bulk of the cooling system can be significantly reduced. For power electronic applications, it is mostly used in conjunction with forced–air and liquid cooling methods for reducing the overall heat sink cost and cooling power consumption [**?**]. The high thermal resistance of PCMs is the main disadvantage compared to other materials, however, it is promising for future applications [**?**].

2.3 Summary of cooling technologies

In section 2.2 an overview of cooling technologies implemented for various electronics cooling has been presented. The advantages and disadvantages in implementation of each method, as

Table 2.1. Summary of cooling technologies in the literature for power electronic devices.

Cooling technology	Method	References
Conduction plate	Solid state cooling	[**?**]
Magnetic cooling		[**?**]
Thermoelectric cooling		[**?**], [**?**]
Thermionic / Thermotunelling		[**?**], [**?**]
Natural air convection	Air cooling	[**?**], [**?**], [**?**]
Forced–air convection		[**?**], [**?**]
Piezoelectric fan		[**?**], [**?**]
Synthetic jet impingement		[**?**]
Electrohydrodynamics		[**?**], [**?**]
Thermoacoustic cooling		[**?**]
Cold plate	Liquid cooling	[**?**]
Mini / micro channel		[**?**], [**?**], [**?**], [**?**]
Electrowetting		[**?**], [**?**]
Immersion		[**?**], [**?**]
Jet impingement		[**?**], [**?**]
Heat pipe	Two–phase cooling	[**?**], [**?**]
Spray		[**?**], [**?**]
Phase change material		[**?**], [**?**]

well as cooling performance and power consumption have been analysed. As already mentioned, the junction temperature of the device, T_{j}, should remain below the maximum operating limit, $T_{\mathrm{j\text{-}max}}$, to avoid catastrophic failure, including chip burn–out and bond wire lifting or melting. Moreover, the lifetime of the power module also depends on T_{j} [**?**] and is discussed in detail in Chapter 5. Therefore, an effective cooling mechanism is a critical component of the power conversion system. Figures 2.16 – 2.18 provide comparisons of the cooling methods in terms of heat flux dissipation, their consumption ratio and volume of the cooling system. It should be noted that the comparisons are done in a qualitative manner based on the information provided in the literature of section 2.2. In Table 2.1, the various cooling technologies that were discussed in section 2.2, are listed with the associated references from the literature.

The most important design parameter of the cooling system for power electronic applications is the heat dissipation. As the chips are shrinking in size and simultaneously provide higher power, the heat fluxes generated are increasing, which highlights the urge for effective cooling and further development and enhancement of heat management methods. Fig. 2.16 compares

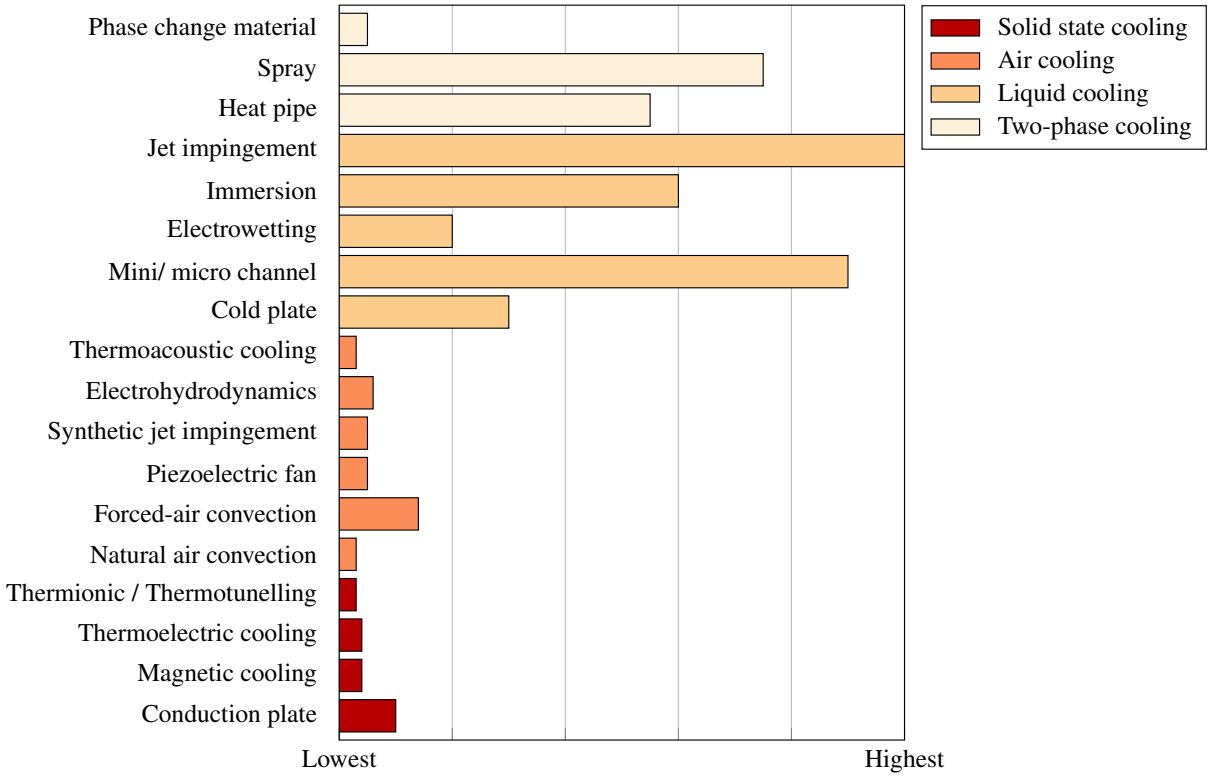

Fig. 2.16. Comparison of heat flux dissipation of cooling technologies.

the cooling methods presented in section 2.2 in terms of heat flux dissipation. As shown, solid state and air cooling techniques are only able to dissipate low amounts of heat flux. The interest for heat management of high heat flux devices is therefore steered towards liquid and two–phase technologies. Mini–, micro–, and jet impingement cooling provide the highest heat dissipation, whereas spray can also be a suitable solution for specific applications. Cold plates are usually used for the heat management of power electronic applications, unless there are high heat fluxes involved or the environment temperature is significantly elevated.

The efficiency of the cooling system is also a very important attribute that should be considered in the design process. With the exception of passive cooling methods, such as conduction plates, natural air cooled heat sinks and heat pipes, the cooling mechanism requires some input power to drive the cooling agent. In the case of water cooling, the power required for operating the mechanical pump driving the coolant is the input power of the cooling system. Similarly, the input power for forced–air cooling is the power supplied to the fan. The consumption ratio of the cooling system is a dimensionless number defined as the ratio of the heat dissipated from

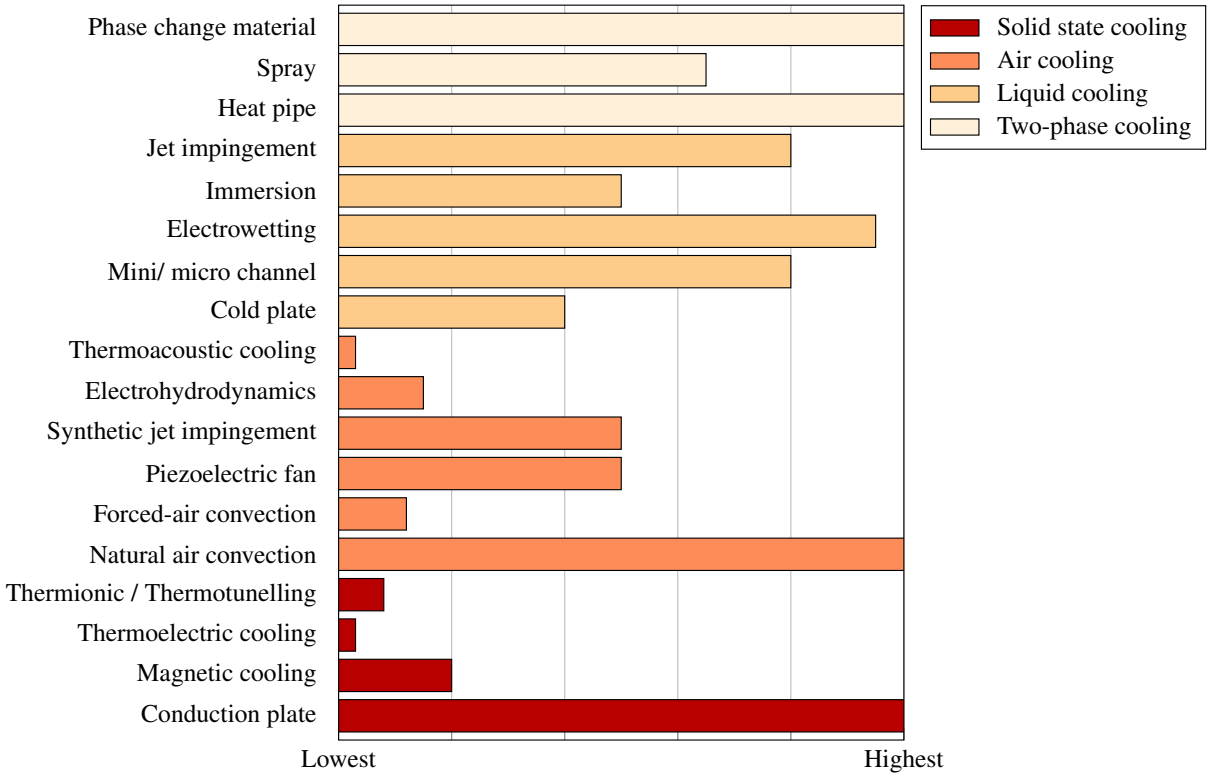

Fig. 2.17. Comparison of consumption ratio of cooling technologies.

the heat source to the ambient air to the input power for operating the cooling system. As Fig. 2.17 shows, passive cooling methods provide the highest consumption ratio, as no input power is required for their operation. Electrowetting offers the highest consumption ratio among the active cooling methods, with mini/micro channel, jet impingement and spray cooling achieving very high numbers of consumption ratio as well. Considering a system–level approach, the consumption ratio of the cooling system affects the overall efficiency of the system that could include power converters, motors, etc. Hence, it is another very important parameter that could also be limiting in certain applications.

Another property of cooling systems that plays a key role in implementation of power electronics thermal management is the volume coefficient of cooling system, which can be defined as the ratio of the volume to the heat dissipation. Fig. 2.18 shows a comparison between the reviewed cooling methods in terms of volume coefficient. Electrowetting, EHD, synthetic jet impingement and piezoelectric fans are able to maintain a small form factor, which can be crucial in specific applications.

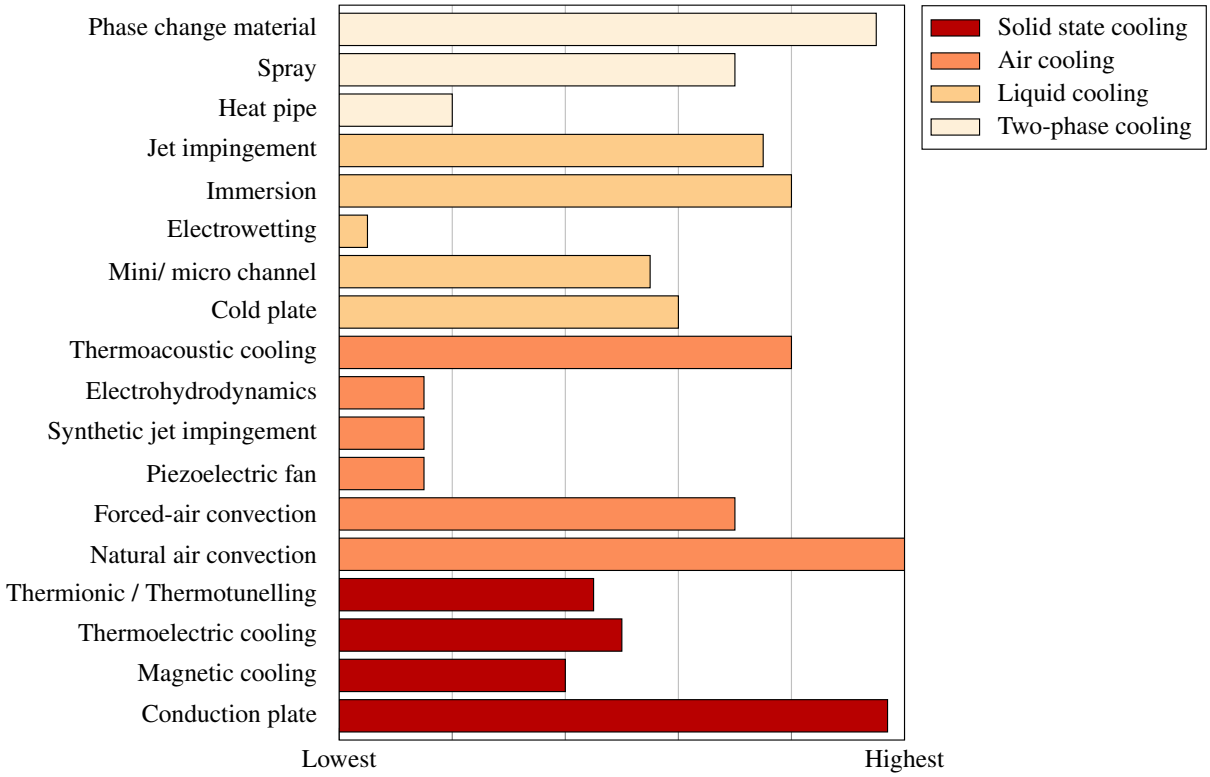

Fig. 2.18. Comparison of heat sink volume of cooling technologies.

In modern high power density applications, the efficiency and volume of the cooling system are equally important to the peak power heat dissipation, so as to achieve high overall power density. Mini/micro channel and jet impingement cooling methods offer high heat dissipation with good cooling consumption ratio and acceptable volume and are the best candidates for such applications. For each cooling method, specific risks and limitations exist that should be considered, such as leakage for liquid cooled systems, mechanical failures for forced–air and liquid cooling, and orientation sensitivity of heat pipes. Finally, parameters such as cost of development, fabrication and maintenance of the cooling system, as well as complexity in manufacturing and implementation should be considered.

Most manufacturers include the static performance of the heat sink in datasheets, however, the dynamic response of the system is as important for specific applications and should also be considered. For example, the dynamic response of natural air convection is much slower than forced–air convection, which is crucial for cases where fast thermal transients need to be dissipated. Even for applications where the use of an active cooling method is either not feasible

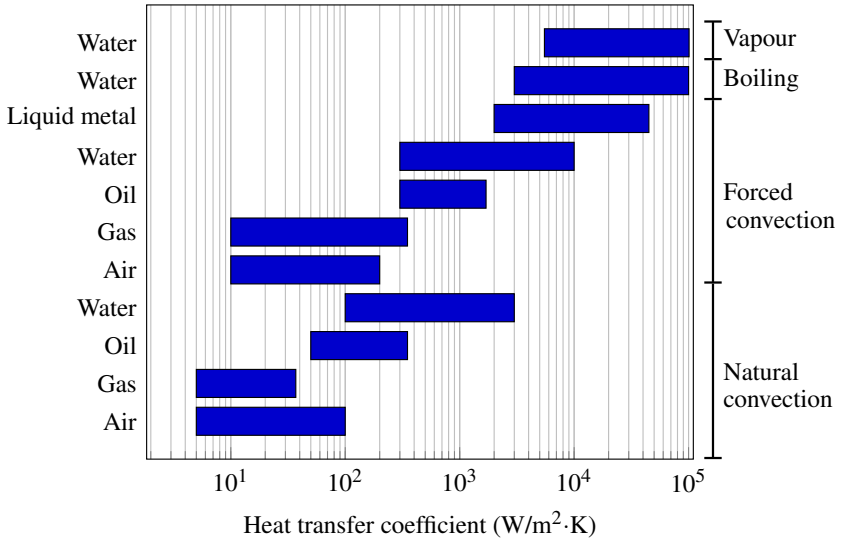

Fig. 2.19. Comparison of heat transfer coefficient for various cooling methods.

or not desirable, advanced conduction plates utilising materials such as pyrolytic graphite can achieve better dynamic response because of the higher thermal diffusivity compared to aluminium and copper.

Fig. 2.19 provides a comparison between various fluids used as coolants and their heat transfer coefficient. According to (2.2), the convective heat transfer coefficient of a cooling mechanism is directly related to its cooling performance. As shown, liquid metals can achieve the highest heat transfer coefficient for single–phase forced convection cooling, due to their superior thermal properties.

This work focuses on the development and fabrication of liquid metal heat sinks in a mini–channel geometry for two different types of power electronic devices. In addition, to exploit the high electrical conductivity liquid metals own, magnetohydrodynamic (MHD) pumps, which are integrated in the heat sink body, are used for driving the fluid in a closed loop. In Chapter 3, the theory on which the MHD phenomenon is based and different MHD pump types are presented.

Chapter 3

Magnetohydrodynamics theory and applications

Magnetohydrodynamics is the branch of physics dealing with the flow of an electrically conductive fluid in the presence of a magnetic field. The term magnetohydrodynamics consists of the components *magneto-*, *hydro-*, and *-dynamics* that stand for the magnetic field, water or any other fluid medium and the motion of the object, respectively. The movement of the fluid can either be accomplished by external forces, in which case the movement of fluid in the presence of a magnetic field will generate an electric current, or by the interaction of the magnetic field and an imposed electric field, where a force is generated driving the fluid.

3.1 The origins of MHD

The birth of MHD is a controversial and a debatable topic. A first attempt was made by Michael Faraday in 1832, when he tried to experimentally validate the use of a conductive fluid for electric power generation. By immersing two electrodes at each side of Waterloo Bridge of Thames and connecting them to a galvanometer, he suggested that the water flow will generate an electromotive force (EMF) because of the interaction of the fluid flow and Earth's magnetic field [**?**]. The experiment did not yield any significant results, apart from some disturbances in

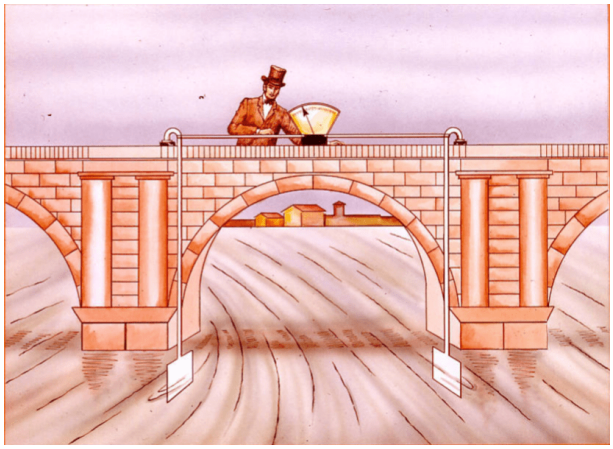

Fig. 3.1. Michael Faraday's Waterloo Bridge experiment [**?**].

the galvanometer, because of equipment limitations at the time. Fig. 3.1 illustrates the experiment ran by Faraday in 1832 [**?**]. Nonetheless, to many people Faraday's experiment can not be classified as an MHD experiment, as the field's dynamic effect on the fluid's motion is negligible and not taken into consideration. Similarly, many of the early attempts to characterise the Earth's geomagnetic field are not accepted as MHD studies, including the experiment of William Hyde Wollaston, who successfully managed to measure an induced voltage in the English Channel in 1851 caused by the interaction of the geomagnetic field and the tide [**?**].

In the first half of 20^{th} century many efforts have been devoted to developing devices for pumping liquid metals. The first attempt was recorded in 1907, when a prototype electromagnetic pump was presented [**?**]. Later in 1928, Allgemeine Elektricitäts-Gesellschaft AG (A.E.G.) demonstrated in public an electromagnetic pump, however, it was dismissed because of the excessive noise it was generating. The pumping of liquid metals for cooling applications was presented by Albert Einstein and Leó Szilárd in 1930. It was used for nuclear reactors cooling 20 years later, however, not extensively, as there were technical challenges in the manufacturing process of the pump [**?**]. In 1937 Julius Hartmann and Freimut Lazarus were the first to characterise incompressible MHD flows by implementing mercury flow for ducts of different dimensions under the influence of a magnetic field [**?**].

Hannes Alfvén is considered to be the father of MHD, as in 1942 he discovered that the interaction of magnetic fields and conductive fluids results in oscillating wave of the ions; an important component for low frequency waves in plasma physics. His theory received a lot of criticism

when it was first introduced, as it conflicted Maxwell's theory of electromagnetism stating that all conductors attenuate electromagnetic waves of a magnitude known as skin depth. In 1958, his theory was experimentally validated in a laboratory environment [**?**]. Alfvén received the Nobel prize in 1970 for his study in MHD. Despite being a branch of classical physics, MHD is a framework of ongoing theoretical and experimental research.

3.2 Governing equations of MHD

The physical laws governing the MHD phenomenon for a Newtonian fluid flow are a combination of electromagnetism and classical fluid dynamics that include Maxwell's equations, Ohm's law and Navier-Stokes conservation of mass and momentum, as well as energy equations. As this study deals with the implementation of a liquid metal heat sink for power electronic devices, the presented governing equations are only limited to Newtonian fluids.

The simplified Maxwell's equations that include magnetohydrodynamic components are:

$$\nabla \cdot \boldsymbol{E} = \frac{\rho_e}{\varepsilon_0} \tag{3.1}$$

$$\nabla \cdot \mathbf{B} = 0 \tag{3.2}$$

$$\nabla \times \boldsymbol{E} = -\frac{\partial \mathbf{B}}{\partial t} \tag{3.3}$$

$$\nabla \times \mathbf{B} = \mu_0 \mathbf{J} \tag{3.4}$$

where $\boldsymbol{E}$ is the electric field, $\mathbf{B}$ is the magnetic field strength, $\mathbf{J}$ is the current charge density, ρ_e is the charge density, ε_0 is the vacuum permittivity and μ_0 the vacuum permeability. In these equations, it is assumed that the magnetic field is solenoidal and therefore, magnetic monopoles do not exist. In addition, magnetic fields could be generated by currents and electric fields could be generated by varying magnetic fields.

Moreover, according to Ohm's law, the current charge density $\mathbf{J}$ is proportional to the force experienced by free charged particles. For a conductive fluid with an electrical conductivity σ

moving with velocity **u** in a magnetic field **B**:

$$\mathbf{J} = \sigma(\boldsymbol{E} + \mathbf{u} \times \mathbf{B}) \tag{3.5}$$

For liquid metal pump applications, the cross product $\mathbf{u} \times \mathbf{B}$ in (3.5) can be interpreted as an apparent electric field. Considering the case of electrical machines, $\mathbf{u} \times \mathbf{B}$ is analogous to the back EMF of the machine, whereas the fluid flow is analogous to the armature voltage. The power produced by the pump is maximised when **B**, $\boldsymbol{E}$ and **u** are mutually orthogonal, in which case $\mathbf{u} \times \mathbf{B}$ is in the opposite direction of **J**.

Moreover, a Lorentz force is acting on a particle with a given charge that is moving with velocity **u**, which is the sum of electrostatic Coulomb forces and magnetic forces. In MHD, the bulk forces acting on the medium are dominating the fluid flow, hence the force per unit volume acting on the conductor is:

$$\mathbf{F} = \rho_e \boldsymbol{E} + \mathbf{J} \times \mathbf{B} \tag{3.6}$$

As the fluid used in most cases has a very high electrical conductivity and its velocity is very small compared to the speed of light, the Coulomb force is negligible and can be ignored. Therefore, only the magnetic force is considered:

$$\mathbf{F} = \mathbf{J} \times \mathbf{B} \tag{3.7}$$

In addition to the electromagnetic equations, the MHD phenomenon also involves fluid dynamics equations to characterise the flow of the medium. Fluid dynamics is a subset of fluid mechanics and deals with the motion of fluids systems. It has a large spectrum that includes both aerodynamics and hydrodynamics, for gases and liquids, respectively. The fundamental laws of fluid dynamics are based on the conservation of mass, momentum and energy and the governing equations describing the fluid flow can be written as:

$$\nabla \cdot \mathbf{u} = 0 \tag{3.8}$$

$$\rho \left(\frac{\partial \boldsymbol{u}}{\partial t} + (\boldsymbol{u} \cdot \nabla)\boldsymbol{u} \right) = -\nabla p + \mu \nabla^2 \boldsymbol{u} + \rho_e \mathbf{E} + \mathbf{J} \times \mathbf{B} \tag{3.9}$$

$$\rho C_{\mathrm{p}}\left(\frac{\partial T}{\partial t}+(\boldsymbol{u}\cdot\nabla)T\right)=k\nabla^2 T+\frac{\mathbf{J}^2}{\sigma} \tag{3.10}$$

where ρ is the fluid density, p is the pressure, μ is the dynamic viscosity and C_{p} is the specific heat capacity of the fluid. The term J^2/σ in (3.10) accounts for Joule heating caused by the injected current. In (3.9), the momentum equation is modified for MHD applications by including the electromagnetic force component, $\rho_e\mathbf{E}+\mathbf{J}\times\mathbf{B}$. As mentioned earlier, the Coulomb force is negligible for liquid metal pumping and thus, can be omitted:

$$\rho\left(\frac{\partial \boldsymbol{u}}{\partial t}+(\boldsymbol{u}\cdot\nabla)\boldsymbol{u}\right)=-\nabla p+\mu\nabla^2\boldsymbol{u}+\mathbf{J}\times\mathbf{B} \tag{3.11}$$

In addition to the electromagnetic and fluid dynamic equations, MHD flows can be described by several non-dimensional parameters, presented in (3.12) – (3.15):

$$Re=\frac{\rho \mathrm{uL}}{\mu} \tag{3.12}$$

$$Ha=\mathrm{BL}\sqrt{\frac{\sigma}{\mu}} \tag{3.13}$$

$$N=\frac{Ha^2}{Re} \tag{3.14}$$

$$Re_{\mathrm{m}}=\mu_m\sigma\mathrm{uL} \tag{3.15}$$

The Reynolds number (Re) is the ratio of inertial to viscous forces for a conductor of length L and can be used to predict the flow pattern[1], Hartmann number (Ha) is the ratio of electromagnetic to viscous forces, Stuart number (N) is the ratio of electromagnetic to inertial forces, and finally, magnetic Reynolds number (Re_{m}) is the ratio of induction to diffusion of $\mathbf{B}$.

Given a conductor of length L, for Re_{m} considerably higher than 1, the magnetic diffusion is not as dominant as the induction. As a result, the magnetic flux cutting through the closed loop of the material is conserved during the fluid's motion. In addition, elastic oscillations are generated by small disturbances on the medium in the presence of the magnetic field, which supplies the restoring force. Therefore, Alfvén waves are generated in the motion of the fluid. In contrast,

[1] More information on fluid flow types is provided in Appendix A.

for Re_m smaller than 1 the magnetic field is almost purely diffusive and determined by external conditions instead of the fluid flow. As the imposed magnetic field is many orders of magnitude larger than the induced magnetic field, the impact of the latter is negligible. Therefore, for flows that own a low magnetic Reynolds number, such as liquid metal flow, the induced magnetic field can be omitted. On the other hand, it should be considered for flows involving plasmas and astrophysical applications, which are out of the scope of this work [**?**].

Other properties that should be considered are the compressibility and viscosity of the fluid. Compressibility is defined as the relative volume change of the medium as a response to a pressure change. In the case where the density of the fluid remains constant through pressure and temperature variations, the flow is described as incompressible. Viscosity is a fluid property determining the friction between the molecules in the fluid. The case in which the viscosity of the fluid has a negligible effect on its flow is called inviscid. The liquid metal flow presented in this work is described as incompressible and viscous.

3.3 Overview of liquid metal MHD applications

The MHD phenomenon has been used extensively with liquid metal as the working medium for fluid pumping, electrical energy generation and flow rate measurement. An overview of various applications and their working principle is presented in this section.

3.3.1 Liquid metal MHD pump

The interaction of magnetic and electric fields is utilised in various applications for driving electrically conductive fluids. Compared to conventional pumps, they offer numerous advantages. The most important is the lack of moving parts. Because of that, the pump can provide silent operation, high reliability and minimal maintenance requirements. In addition, the pump can operate at very high temperatures and demonstrate high efficiencies. They have been successfully used for a range of applications, including seawater thrusters for ship propulsion [**? ? ?**], liquid

metal stirring and shaping for industrial applications [**? ? ?**], molten salt pumping in nuclear reactors cooling [**? ?**], blood pumping [**?**], sample propelling [**?**] etc. In addition, a few instances have been reported where MHD pumps have been used for liquid metal cooling of electronic devices, as discussed earlier in Chapter 1.

As Fig. 3.2 shows, MHD pumps are split in two main categories depending on how the magnetic and electric fields are developed; conduction pumps and induction pumps. The selection of pump type depends on application–specific constraints, such as size, cost, performance, and efficiency. The advantages and disadvantages of each topology are discussed in the rest of the section.

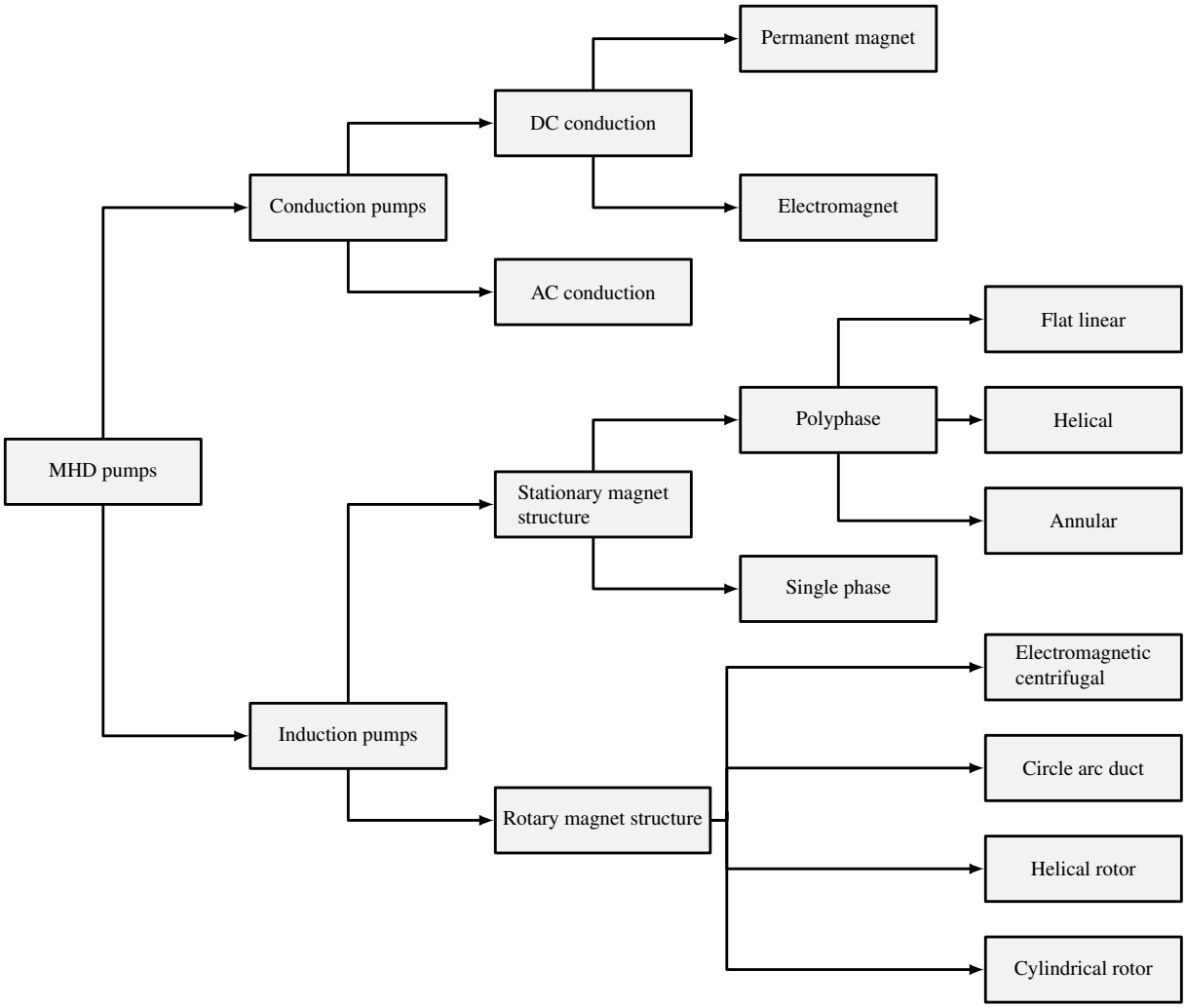

Fig. 3.2. Classification of MHD pumps

Conduction pump

Conduction pumps provide the current in the active part of pump, which is where the electric and magnetic fields intersect, through electrodes that are physically contacting the wall of the pump or in some cases, the fluid directly. Conduction pumps can be classified as either DC or AC, depending on the current that is supplied to the electrodes. Both types of conduction pumps have similar loss mechanisms, as the same pump structure is maintained for driving the fluid.

DC conduction pumps have simple structure, consisting of electrodes that provide the electric current and either permanent magnets or electromagnets for providing the magnetic field. Both fields are oriented perpendicular to the conductive fluid, so as to maximize the Lorentz force. Typical examples of DC conducting pumps that utilise permanent magnets and electromagnets are shown in Fig. 3.3(a) and Fig. 3.3(b), respectively.

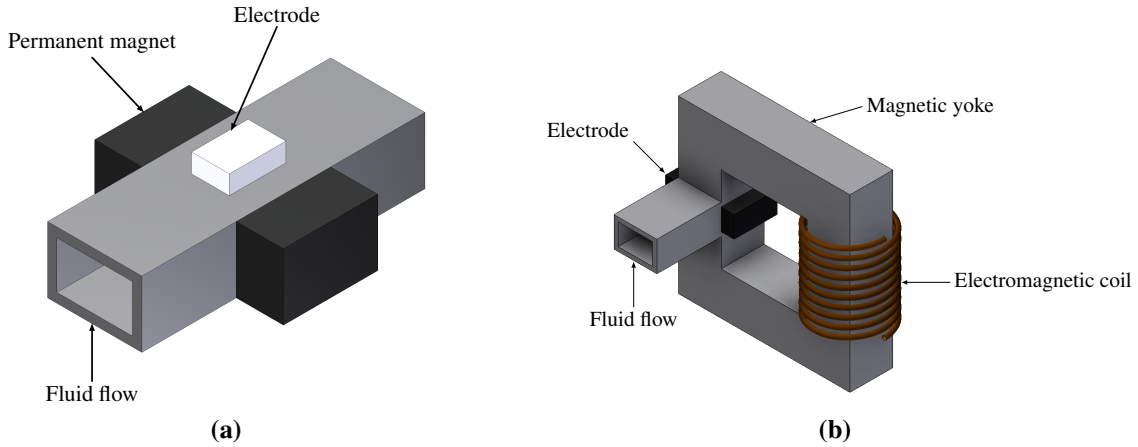

Fig. 3.3. Examples of DC MHD pump with the use of: (a) permanent magnets (b) and electromagnetic coil.

In spite of the many advantages that this type of pump offers, there are many loss mechanism that can reduce its performance. Firstly, the current passing through the electrodes results in ohmic losses in the system. Moreover, at the ends of the pump, the magnetic field is either weaker or not present. Thus, the efficiency is reduced, as the current passing through these areas does not contribute as much. Also, as the current passes through the fluid, an extra magnetic field is induced that opposes the applied magnetic field and therefore, decreases the overall magnetic

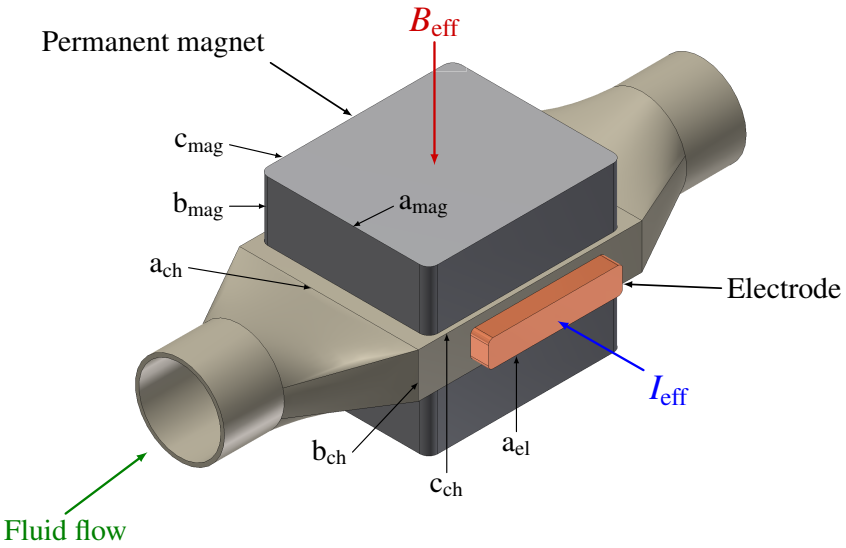

Fig. 3.4. Schematic of a typical MHD pump.

flux density. In addition, depending on the pump materials, wall currents could be induced because of the fluid motion. Finally, while the fluid moves in the magnetic field a back–EMF is generated in the opposite direction of the injected current that contributes in the power loss of the pump. The effect of these loss mechanisms depends on the working conditions of the pump, however, they are more prominent for applications like liquid metal steering and casting, as well as nuclear reactors cooling. In all these cases either a high operating current ($>10\,\text{kA}$) is used to achieve high pressure difference and therefore the ohmic losses and armature effect are large or the flow rate of the liquid metal is high ($>90\,\text{L}/\text{min}$) and the back–EMF losses should be considered. Nonetheless, the study cases that are presented in this work involve relatively low flow rates and operating currents, hence, the losses are not affecting the pump performance.

A schematic representation of the principle on which DC conduction pumps operate is shown in Fig. 3.4. The working fluid moves in a channel of width a_{ch}, height b_{ch}, and length c_{ch} with the magnetic and electric fields placed perpendicular, so as to maximise the Lorentz force. The Lorentz force exerts body force F on the fluid that can be expressed as:

$$F = \int (\mathbf{J} \times \mathbf{B}) \cdot \mathrm{d}V \approx B_{\text{eff}} \cdot \mathrm{I}_{\text{pump}} \cdot a_{\text{ch}} \tag{3.16}$$

where $\mathrm{d}V$ is the active volume of the pump (i.e. the volume of the fluid under the presence of electric and magnetic fields), B_{eff} is the efficient magnetic flux density, and I_{pump} is the current

through the electrodes. As the channel width b_{ch} is the distance between the electrodes, it is considered to be the conductor length (i.e. the current flow distance). The direction of the flow is dictated by the direction of electric and magnetic fields. Equation (3.16) assumes that **B** and **J** are homogeneous and constant. As shown in (3.17), the pressure developed by the pump is only a function of the magnetic field strength, the injected current, and the pump height b_{ch}:

$$P_{\mathrm{MHD}} = \frac{F}{A} \approx \frac{B_{\mathrm{eff}} \cdot \mathrm{I}_{\mathrm{pump}}}{\mathrm{b}_{\mathrm{ch}}} \tag{3.17}$$

where P_{MHD} is the pressure head and A is the cross section of the pump with width a_{ch} and height b_{ch}.

In contrast with DC conduction pump, the electric and magnetic fields of an AC conduction pump are time varying. A schematic representation of a typical AC conduction pump is shown in Fig. 3.5. A transformer is often utilised for providing the time–varying current in combination with an electromagnetic coil providing the time–varying magnetic field. The introduction of additional components results in extra weight, bulk and design complexity. Although the presence of a transformer allows for providing higher currents at low voltages more practically, the ohmic losses generated in these devices often require a cooling mechanism that furthers complicates the design. In addition, as both fields are varying, the Lorentz force ($F(t)$) applied on the fluid is also time dependent. The magnetic field ($B(t)$) and conducted current ($I(t)$) are described by:

$$B(t) = B_{\max} \cdot \sin(\omega t) \tag{3.18}$$

$$I(t) = I_{\max} \cdot \sin(\omega t \pm \theta) \tag{3.19}$$

where ω is the field frequency and θ is the phase difference between them. Hence, the resultant body force, $F(t)$, is:

$$F(t) = \frac{1}{2} \cdot B_{\max} \cdot I_{\max} \cdot \mathrm{L} \cdot \Big(\big(1 - \cos(2\omega t)\big) \cdot \cos\theta \mp \sin(2\omega t) \cdot \sin\theta \Big) \tag{3.20}$$

As the physical method for conducting the two working fields is the same for DC and AC conduction pumps, all the loss mechanisms mentioned earlier are valid for this type of pump in RMS values. In addition to other losses, eddy currents that provide no useful work are induced

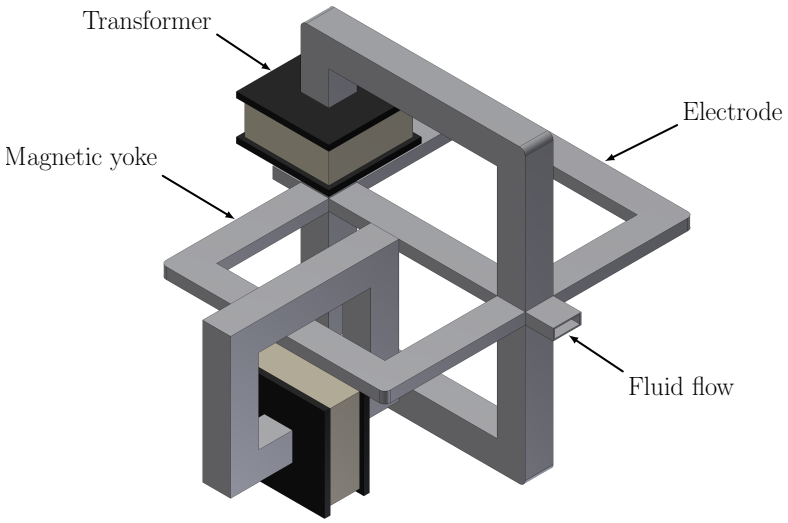

Fig. 3.5. Example of AC MHD conduction pump

in the working fluid and pump's walls. Finally, as shown in (3.20), phase difference between the electric and magnetic fields leads to reduced force exerted to the fluid.

Induction pump

The operation of induction MHD pumps is based on induced currents generated by a travelling magnetic field. As Fig. 3.2 shows, the different topologies that exist for induction pump are divided in two groups depending on the way the travelling magnetic field is established: (i) induction pumps that have a stationary magnetic structure and (ii) induction pumps that have a rotating magnetic structure. Induction pumps with stationary magnetic structure, such as flat linear, annual linear and helical induction pumps, have coils wounded on iron cores that are supplied with a time varying current. The current generates a magnetic field that is induced in the conducting fluid and in its turn induces currents in the fluid. The cross product of the two fields results in a Lorentz force that acts on the liquid metal. The schematic diagram of a typical induction pump that operates with a non–rotating magnetic structure is shown in Fig.3.6.

Compared to conduction pumps, induction pumps have the ability to operate at extreme temperatures, as there is no physical contact between the supplied fields and the fluid channel. In

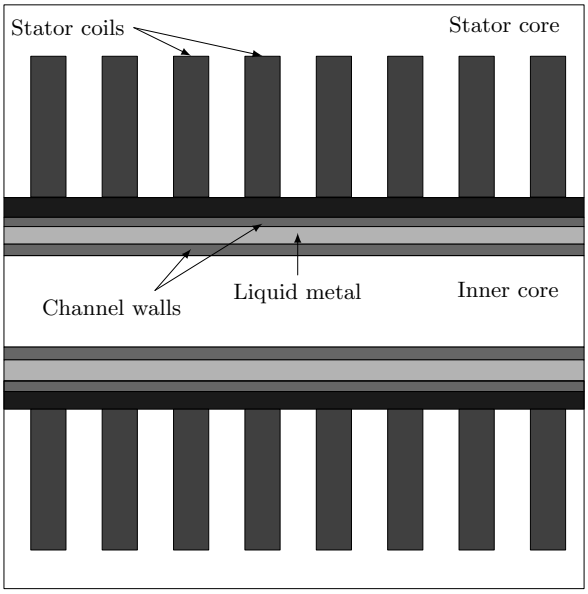

Fig. 3.6. Cross sectional view of typical induction pump with fixed magnetic structure.

addition, they demonstrate higher efficiencies when operating at high power and easier integration in existing high power systems through AC power. As with conduction pumps, many loss mechanism as associated with its operation, such as resistive heating through the supply coils and the liquid metal itself, eddy currents that are induced in the working fluid and the pump's walls and Lorentz force oscillation that could lead to disturbances and vibrations, as the force velocity is not in–phase with the fluid velocity. Moreover, induction pumps with a rectangular duct, such as flat linear induction pumps, can suffer from magnetic leakage. Finally, additional heat conducted from the liquid metal to the stator structure should be considered. The stator should be close to the channel for achieving a strong magnetic field, however, as the temperature of the working fluid in applications like nuclear reactors cooling and metal stirring is very high, some of the heat is transferred to the stator structure and therefore, external cooling of the pump is required.

Another type of induction pump has a rotating magnetic structure and uses permanent magnets to achieve the travelling magnetic field. A schematic diagram of a permanent magnet induction pump is shown in Fig. 3.7. The magnets are fixed on the pump's core that is coupled to the shaft of an external machine. An outer ferrous sleeve is utilised for closing the magnetic path. The principle of operation is similar to induction pumps with a stationary magnetic structure, as the Lorentz force is generated by the interaction of the travelling magnetic field that cuts

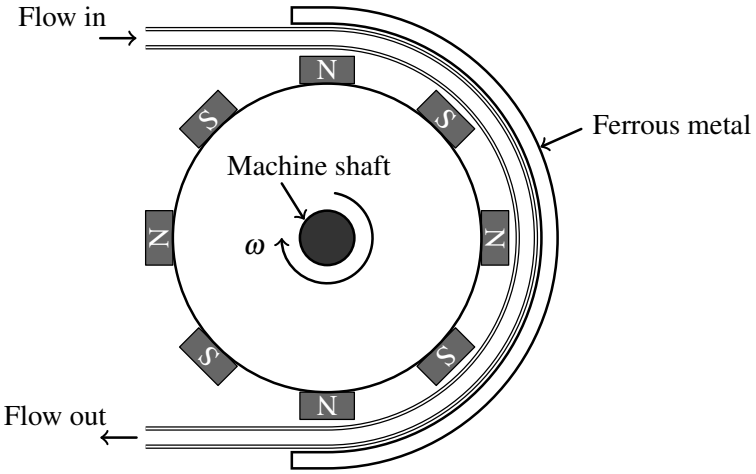

Fig. 3.7. Example of rotating induction pump.

the conducting fluid and the induced currents in the fluid caused by the magnetic field itself. Comparing the two induction pump topologies, the pumps with rotating magnetic structure demonstrate higher efficiencies as any resistive losses associated to the magnetic field generation are not present. Consequently, external active cooling of the pump is not required. In addition, its design and fabrication is considerably simpler.

In general, induction pumps are more suited for high power/high flow rate applications, as their efficiency is greater when operating at high power. However, the additional weight and bulk of the field generation system and the support structure makes them unsuitable for small–scale applications. As this work investigates the use of liquid metal cooling for power electronics applications, where the flow rate and pressure requirements are low, and weight, volume, efficiency, and reliability are of paramount importance, DC conduction pumps with permanent magnets, which will be referred to as MHD pumps in this thesis, were selected for both study cases that are presented in the following sections.

For applications such as cooling and molten metals stirring, the MHD phenomenon is utilised to function as pump. The magnetic and electric fields are supplied or induced in the structure of the device, which results in fluid flow. Similarly, liquid metals can be the working fluid for applications other than pumping, such as flow rate measurement and electric power generation. For both flow meters and generators, the output of the system is the current for a given magnetic field and fluid motion. Liquid metal MHD flow meters are a mature technology, commonly used

for molten metals flow rate measurements, whereas research on MHD generators since 1960s has led to substitution of plasma for liquid metal in many generation systems.

3.3.2 Liquid metal MHD generator

Faraday and Hall generators are the two main configurations for MHD power conversion. The Faraday generator, shown in Fig. 3.8(a) uses multiple electrode pairs across the length of the active channel in order to minimise the Hall effect. However, as each electrode pair has its own load, there is a voltage difference between their outputs. On the other hand, Hall generator shown in Fig. 3.8(b) has the advantage of having only one load and can deliver high power densities. Nonetheless, the efficiency is poor compared to segmented Faraday generator [**?**].

MHD generators are classified as open cycle and closed cycle, depending on their operating principle. Open cycle uses atmospheric air in high temperature and high pressure mixed with coal in a combustor. It is then mixed with a seeding material, so as to increase the electrical conductivity of the plasma, and passes through the magnetic field. Ions movement toward the electrodes that are placed perpendicular to the magnetic field results in the generation of an electric field. Finally, the medium exits from the generator to the ambient air. On the other hand, the closed cycle operates in a closed loop, which has significant benefits over open cycle, such as effective heat transfer and pollution–free operation, as the same fluid is used without mixing with the ambient air. Because of its ability to operate in a closed loop without contacting the ambient, liquid metals can be utilised as the working medium, which have additional benefits

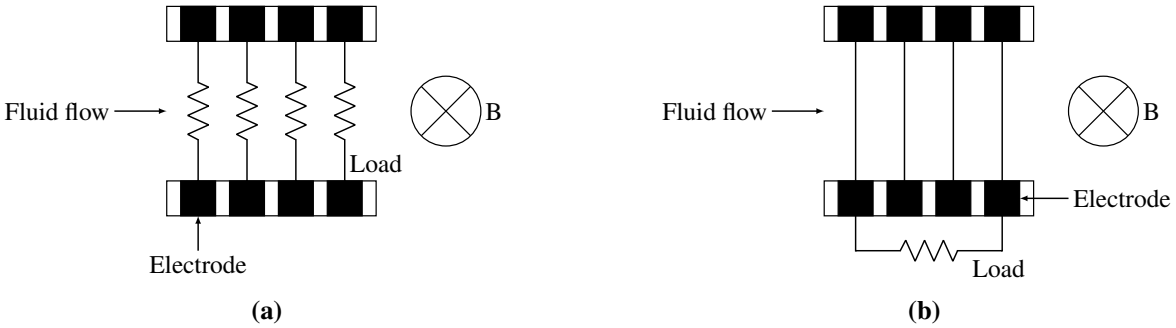

Fig. 3.8. MHD generator configurations: (a) Faraday and (b) Hall.

compared to gas, since their electrical conductivity is 5–6 orders of magnitude larger than ionised gas. Hence, the operating temperature is much lower. In addition, liquid metal MHD generators are able to output high currents at low voltages. Compared to conventional energy generators based on steam, MHD systems have the advantage of no moving parts, which increases the reliability and eliminates frictional losses. In addition, higher efficiency is achievable and power is delivered instantly. The main disadvantages are the requirement for electrically conductive working medium and corrosion in the generator structure due to the relatively high operating temperatures [**? ? ?**].

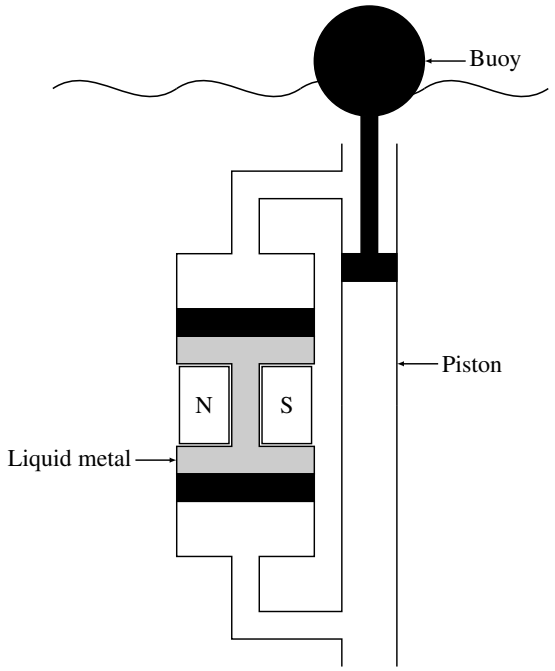

Fig. 3.9. Schematic of liquid metal MHD generator for wave energy conversion.

In addition to industrial power plants, liquid metal MHD generators are used for harvesting renewable energy. More specifically, they take advantage of the ocean waves periodic movement in a direct wave–to–electrical energy conversion. A schematic diagram of the generator's operating principle is shown in Fig. 3.9. The liquid metal is driven via an external piston coupled to a buoy. As mentioned before, the interaction of the moving conducting fluid with the magnetic field yields a net electric power, that is typically applied for charging autonomous underwater vehicles [**?**] and underwater sensors and monitoring devices [**?**].

3.3.3 Liquid metal MHD flow meter

The famous experiment by Faraday on Waterloo Bridge was the first attempt of measuring the flow rate of an electrically conductive fluid by using the MHD phanomenon, albeit an unsuccessful one. In 1950s, electromagnetic flow meters based on Faraday's theory were commercially available. The magnetic field was imposed in the fluid externally and the flow rate was calculated based on the output current through the electrodes. Although the implementation of such device is straightforward, it requires mechanical contact with the fluid or the channel walls, which is not desired for high temperature applications.

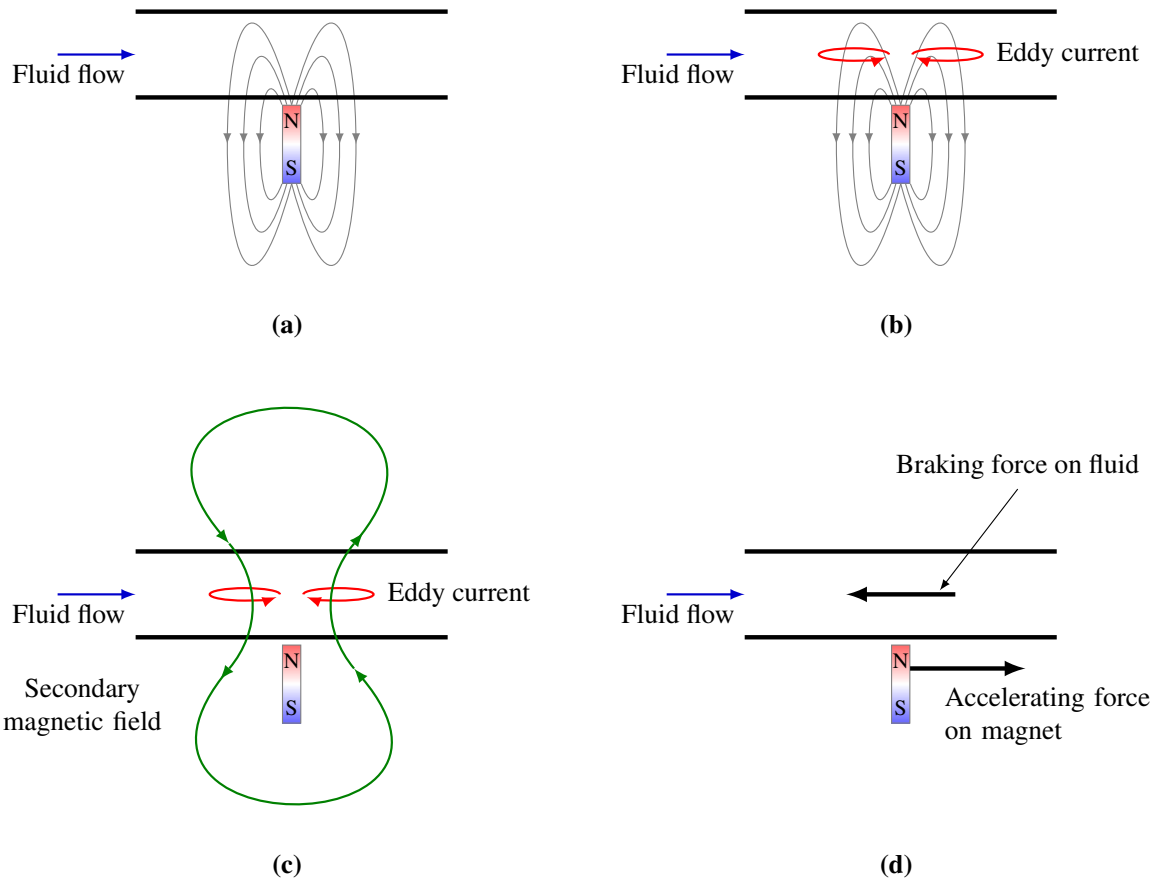

Fig. 3.10. Working principle of Lorentz Force Velocimetry: (a) The electrically conductive fluid travels in a magnetic field. (b) Eddy currents are induced in the fluid. (c) The eddy currents generate a secondary magnetic field. (d) A braking force acts on the fluid that is equal to the accelerating force acting on the magnet.

To overcome this challenge, devices known as force flow meters were developed. The flow rate is estimated based on the force generated within the fluid. Lorentz Force Velocimetry (LFV) is a variant of force flow meters and its operating principle is shown in Fig. 3.10. As an electrically conductive fluid cuts the magnetic field lines while moving, eddy currents are induced in the fluid itself. According to Ampere's law, the eddy currents generate a secondary magnetic field resulting in a Lorentz force opposing the fluid flow. By Newton's third law the action of the braking Lorentz force will give rise to an accelerating force acting on the magnet body. By measuring the magnitude of the accelerating force, which is proportional to the fluid velocity and the magnetic field strength, the fluid flow rate is determined. Nowadays, LFVs are extensively used in metallurgy, chemical processing and food processing [**? ?**].

3.3.4 Conclusion

This section has presented a wide range of MHD applications that utilise liquid metals as the working fluid. More specifically, applications such as liquid metal pumping, electric power generation based on the fluid flow and liquid metal flow rate measurements, as well as their working principles have been presented. The scope of this work focuses on the pumping of a liquid metal that is used as a cooling medium for power electronics applications. However, the other two applications can be combined in future work within the same cooling device. For example, an MHD generator can be combined with the pump and thus, feed some power back to the system in order to reduce the power consumption of the cooling device. Similarly, a liquid metal flow rate meter can be incorporated into the structure of the heat sink and aid in the coolant's flow control.

Considering the various types of pumps presented earlier, induction pumps are more suited for high power/high flow rate applications, as their efficiency is greater when operating at high power. However, the additional weight and bulk of the field generation system and the support structure makes them unsuitable for small–scale applications. As this work investigates the use of liquid metal cooling for power electronics applications, where the flow rate and pressure requirements are low, and weight, volume, efficiency, and reliability are of paramount importance,

DC conduction pumps with permanent magnets, which will be referred to as MHD pumps in this thesis, were selected for both study cases that are presented in the following sections.

Chapter 4

Liquid metal thermal management of conventional power module

Thermal management for power semiconductor devices is essential for dissipating the excess heat generated by the electronic chips during their operation. As already highlighted in Chapter 2, efficient and effective thermal management of electronic devices provides many significant advantages for the operation of the overall conversion system. For example, with more effective cooling higher heat flux can be removed from the chip. Consequently, the device can either be used in higher power systems or in harsh environments with elevated ambient temperatures. In addition, the power consumption of the cooling system is of equal importance, as it affects the overall power density of the system. Finally, an effective cooling system can significantly reduce the operating junction temperature of the device. Consequently, the remaining useful lifetime (RUL) of the device can be significantly increased.

The active structure of the IGBT device is applied on a silicon chip, however, a package is required to provide electrical connection and a thermal path to the ambient. Therefore, the package technology is as important as the semiconductor chips themselves for the operation of the device. The illustration of a conventional half–bridge IGBT power module is shown in Fig. 4.1. Its structure consists of many layers of different materials stacked on each other. The baseplate is usually made of nickel–plated copper, which has high thermal conductivity, in order

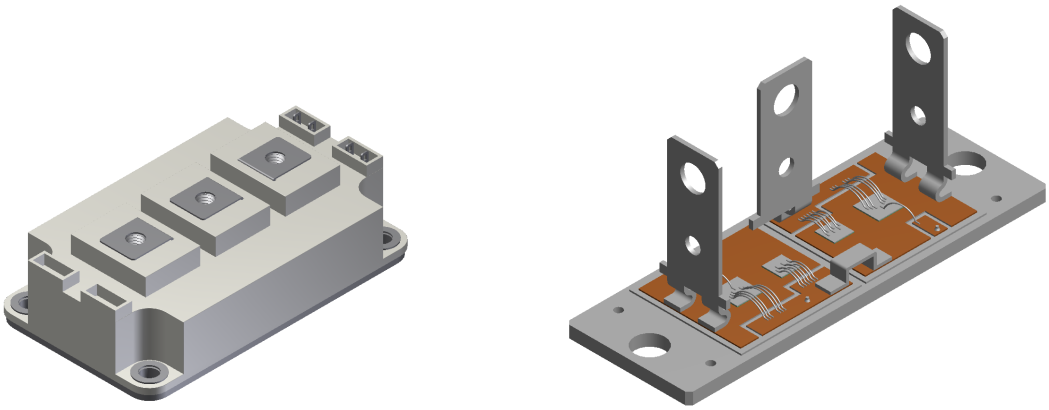

(a) (b)

Fig. 4.1. Conventional half–bridge IGBT power module: (a) sealed module and (b) protective cover removed.

to ensure an effective thermal path from the silicon chip to the heat sink. Electrical insulation is provided by the direct copper bonded (DCB) substrate that is made of layered copper and aluminium nitride. The latter is a material that provides high electrical resistivity and thermal conductivity, thus ensuring heat dissipation through it and at the same time electrical insulation. A plastic protective cover is also used for electrical insulation. Finally, for high–voltage applications a dielectric gel is applied on the top surface area of the power module. Screw contacts are used for the power terminals for securing electrical connection. Most of the conventional power module failures are due to the absolute operating temperature and temperature cycling of the IGBT chip, which further highlights the importance of thermal management for power electronic devices.

Also in Chapter 2, an overview of various heat sinks used in power electronic applications have been presented. As two–phase cooling is out of the scope of this thesis, liquid metals are the fluids that achieve the highest heat transfer coefficient for single–phase cooling. In addition, heat sinks configured in mini–channel geometry have been reported to successfully remove high heat fluxes. In this chapter, the design and development of a liquid metal heat sink for conventional power modules is provided, including the implementation of thermal models and a junction temperature sensing technique for the power module, the design of the MHD pump and its hydrostatic characterisation, and finally, the design of the liquid metal heat sink and its thermal characterisation through simulation and practical experiments.

4.1 Thermal modelling for power electronic devices

Thermal modelling estimates the heat transfer in a system mathematically, which is either caused by internal effects, such as the self–heating of the chip due to power losses, or by external conditions, such as the ambient temperature. Thermal equivalent networks are utilised to emulate the thermal impedance of the device, thus indicating its temperature response. Thermal networks are able to describe a variety of problems; from simplified one – dimensional (1–D) to complex three – dimensional (3–D) heat flows [**?** **?** **?**]. The analogy between electrical and thermal domains, which is presented in Table 4.1, can be used to couple the thermal behaviour of electronic devices to electrical parameters in circuit simulation software. Finite element methods are also popular for determining the thermal behaviour of power electronic systems, especially for investigating multidisciplinary problems [**?**].

Table 4.1. Electrical and thermal analogy.

Electrical			Thermal		
Parameter	Symbol	Unit	Parameter	Symbol	Unit
Voltage	V	V	Temperature	T	K
Current	I	A	Heat flow	P	W
Electrical resistance	R	Ω	Thermal resistance	R_{th}	K/W
Electrical capacitance	C	F	Thermal capacitance	C_{th}	J/K
Electrical conductivity	σ	S/m	Thermal conductivity	k	W/(m·K)
Stored charge	q	C	Stored heat	q	J

4.1.1 Types of thermal models

The most commonly used thermal networks are Foster [**?**] and Cauer [**?**]. Schematics of these networks for a power electronic device application are illustrated in Fig. 4.2. Their implementation assumes that the heat generation is uniform in the top surface of the chip and that the heat propagates perpendicularly to the bottom surface, which is usually a heat sink. Despite that the networks shown in Fig. 4.2 are only considering one heat source (i.e. one electronic chip), extending them for multiple heat sources is possible. The transient response of the junction temperature, T_j, of the device for known input power loss, P(t), and ambient temperature, T_{amb}, is calculated based on the impedance of the network's elements. The total thermal impedance

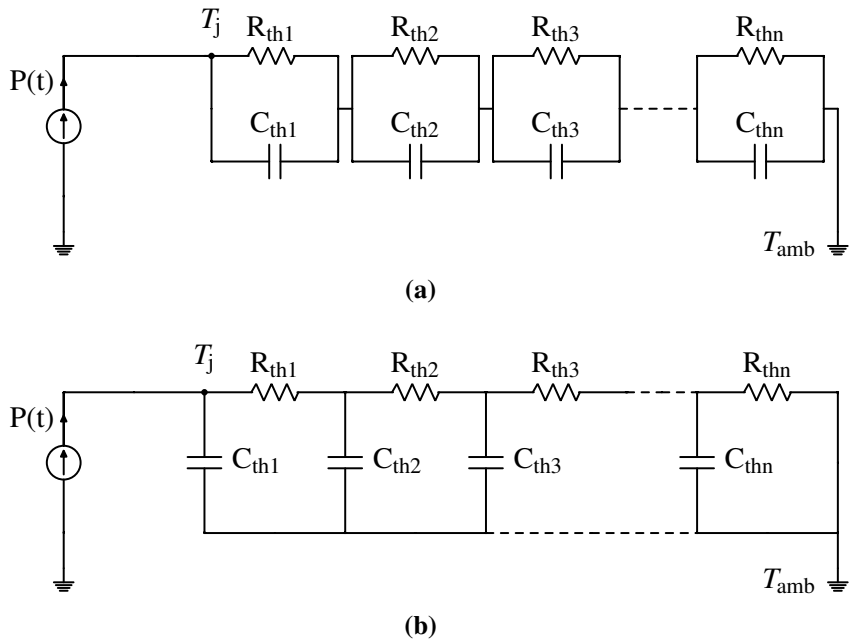

Fig. 4.2. Thermal network topologies: (a) Foster and (b) Cauer.

value that corresponds to the sum of resistances and capacitances in the network can either be obtained via parametrisation of network's components through curve fitting of the temperature step response or via calculation of each component value based on material's geometry and physical properties. The advantages and disadvantages of both methods are discussed in the following sections.

Foster network

In this model it is assumed that the power electronic device has a small cubical geometry and is attached to an isothermal heat sink. As mentioned earlier, the whole amount of heat travels from the chip, which has uniform heat distribution, to the heat sink. Therefore, the sidewalls of the device are thermally insulated. For a step input, the temperature response of the device can be described as:

$$T_{j(t)} = \mathrm{P(t)} \cdot Z_{th(t)} + T_{hs} \tag{4.1}$$

where T_{hs} is the reference temperature of the heat sink. The transient thermal impedance, $Z_{\mathrm{th(t)}}$, is described as the sum of exponential time constants.

$$Z_{\mathrm{th(t)}} = \sum_{i=1}^{n} \mathrm{R}_{\mathrm{th},i}\left(1 - e^{-\frac{t}{\tau_{\mathrm{th},i}}}\right) \tag{4.2}$$

where τ_{th} is the thermal time constant defined as:

$$\tau_{\mathrm{th}} = \mathrm{C}_{\mathrm{th}} \cdot \mathrm{R}_{\mathrm{th}} \tag{4.3}$$

The values of $\mathrm{R}_{\mathrm{th},i}$ and $\tau_{\mathrm{th},i}$ for every node can be obtained through the transient response of the device (i.e. cooling or heating curve). Power electronic manufacturers often include the values of Foster thermal network in the datasheet of the device. Usually, four R_{th} C_{th} elements are required for obtaining the transient response, albeit a higher order model yields more accurate results.

Although the Foster model is easy to derive and adequately accurate, it has a pure mathematical basis and the R_{th} C_{th} elements and τ_{th} have no physical representation. As thermal capacitances C_{th} are connected in parallel to their equivalent thermal resistances R_{th}, the current flow at each side of the capacitor is the same. Foster network can provide the thermal behaviour at the first node representing T_{j}, however, the thermal distribution within the device's layers can not be obtained. Consequently, if the thermal resistance of the heat sink that is attached to the power semiconductor changes, the model derivation process should be repeated.

Cauer network

Cauer model is derived from classic heat transfer physics and the elements consisting the network can be calculated based on the components' geometry and physical attributes under the condition of 1-D heat flow. In contrast with Foster model, Cauer model has physical meaning. Hence, each R_{th} C_{th} element represents a layer of the device. Each capacitor C_{th} is connected to the thermal ground, thus representing the energy stored in each layer and the heat propagation between the components.

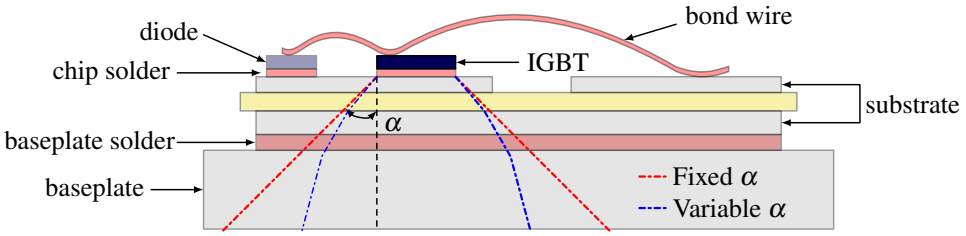

Fig. 4.3. Heat spreading angle α in IGBT power module.

A spreading angle α of 45° is usually assumed, however, this is only applicable where the heat does not accumulate in subsequent layers that own a lower thermal conductivity. As the heat transfer in IGBT power modules is a three–dimensional problem, such assumption could lead to erroneous results and should be avoided in cases where the thermal model is to be used for accurate temperature measurements [**?**]. The schematic representation of an IGBT device in Fig. 4.3, shows a comparison of a 45° fixed and variable heat spreading angles for a multilayer IGBT power module that is not drawn to scale.

The thermal components R_{th} and C_{th} for a layer of heat flow length L and surface area A, can be calculated by:

$$R_{th} = \frac{L}{k \cdot A} \tag{4.4}$$

$$C_{th} = C_p \cdot \rho \cdot L \cdot A \tag{4.5}$$

Similar to the Foster network topology, a minimum of four R_{th} C_{th} elements between the heat source and sink are required to accurately represent the transient temperature response [**?**].

Finite element analysis

For 3–D complex thermal problems, finite element analysis (FEA) is used. The 3–D geometry of the system is approximated by a mesh that consists of a finite number of elements, each assigned with a set of algebraic equations. For thermal analysis, the temperature is the unknown in each node. Therefore, the temperature distribution within a surface or a volume can be found by solving the heat transfer equation for every node. Precise geometry of the model, as well as valid material data are key components for an accurate solution. In addition, known boundary conditions, such as the input heat, ambient temperature, sidewalls thermal behaviour etc., should

also be defined. The meshing elements number, size and shape are also very important for accurate and valid results.

Thermal analysis based on FEA is often combined with fluid flow and/or other problems, although, at early stages of simulating or if a simplified solution is required, the fluid flow can be defined as a convective boundary condition, thus focusing solely on the heat conduction through the solid components of the power electronic device. Multiphysics software, such as ANSYS and COMSOL, are usually used for FEA, as they can couple the thermal problem to an electromagnetic, fluid dynamics, structural problem etc.. However, FEA is a much more compute–intensive task than the thermal models mentioned earlier, hence it is not used for online temperature measurement. Instead, it is mostly limited to offline thermal evaluations. FEA is a powerful tool for analysing thermal models and providing solutions for complex phenomena, however, users face several challenges in using them, such as simulation speed and accuracy, lack of coupling between various FEA software and credibility of results in comparison to experimental work [**?**].

4.1.2 Development of a 1–D Cauer network for power module

As discussed in the previous sections, a Cauer model is directly associated with physical parameters of the device and is able to provide information on the temperature distribution of the power module's inner layers. The Cauer model presented in this work is based on a multilayer IGBT power module (Semikron SKM50GB063D), whose structure is schematically represented in Fig. 4.3. Despite that a high order network would likely return more accurate results regarding the transient response of the temperature, the constructed model was limited to one R_{th} C_{th} element per layer of the power module. Additional elements were used to emulate the TIM and heat sink attached to the device. All material parameters and layer geometries for the selected power module are listed in Table 4.2.

As illustrated in Fig. 4.4, dimensions a_s, b_s and c_s are the two sides and the thickness of the material, respectively. A number of assumption were made for constructing the 1-D Cauer thermal network. Firstly, the IGBT chip is considered to be the only heat source in the device.

Table 4.2. Power module and heat sink physical properties and dimensions.

Layer	Physical properties			Dimensions		
	ρ [k/m^3]	k [W/(m·K)]	C_p [J/(kg·K)]	a_s [mm]	b_s [mm]	c_s [mm]
Silicon die	2330	163	703	6.5	6.5	0.22
Die attach	9000	50	150	6.5	6.5	0.08
Copper (top)	8950	400	385	28.4	25.8	0.3
Aluminium oxide	3900	27	900	30.6	28	0.38
Copper (bottom)	8950	400	385	28.4	25.8	0.3
DCB solder	9000	50	150	28.4	25.8	0.08
Baseplate	8950	400	385	91.4	31.4	3
TIM	2100	0.55	1000	92	32	0.03
Heat sink	2700	160	900	125	100	1

All the heat is transferred from the chip to the heat sink, where the back–surface temperature is equal to the environmental temperature. Consequently, thermal coupling caused by neighbouring heat sources is neglected. All layers in the device are assumed to have a virtual homogeneous temperature at their center, which allows to model each layer using only one R_{th} C_{th} element. In addition, the heat transfer is assumed to be one–dimensional, as the surface area to the thickness of each component is very large. In reality, the heat does not travel from the IGBT chip straight to the heat sink but rather spreads to the intermediate layers before reaching the cooling mechanism. To compensate for some of the heat spreading, a heat spreading angle, α, of 45° is introduced to the model. The use of this angle implies that the heat transfer is homogeneous and heat propagation does not occur because of heat transfer from a medium with high thermal conductivity to a medium with low thermal conductivity. As mentioned earlier, a variable spreading angle should be used in cases where high accuracy is essential. In addition, the heat transfer is assumed to be purely conductive, therefore, heat dissipation through convection and radiation are assumed to be zero. As such, the heat sink is assumed to be a convective

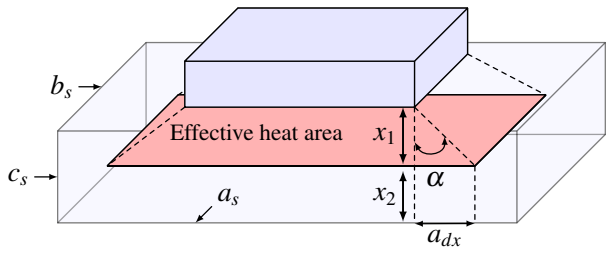

Fig. 4.4. Heat spreading area A_{he} between module's layers.

boundary condition. Also, the material properties of the layers are considered to be independent of temperature variations. Finally, the thermal contact resistance between the two layers is considered to be zero. Although adhesive material between the layers has a physical thickness, it is considerably small and cannot be quantified to be included in the thermal model.

The effective heat area (A_{he}) should be calculated in order to define each R_{th} and C_{th} value. The schematic in Fig. 4.4 shows two neighbouring layers, in which heat is transferred from the top to the bottom one. As the heat is assumed to be in the middle plane of each layer, the distances x_1 and x_2 are equal. For a spreading angle of α=45° the distance a_{dx} is also equal to x_1. Since the IGBT chip has a square shape, all four sides of A_{he} are the same, defined as:

$$A_{\text{he}} = (a_s + 2\,a_{dx})^2 \tag{4.6}$$

where:

$$a_{dx} = \frac{1}{2} c_s \tag{4.7}$$

The effective heat area for each layer is shown in Table 4.3. In addition, by using (4.4)–(4.5) the R_{th} and C_{th} values for each element are calculated and also presented in Table 4.3. It should be mentioned that the heat spreading angle α between the silicon die and die attach is assumed to be zero, as both layers have the same side distances, a_s and b_s. Also, the power module is assumed to be mounted to an aluminium heat sink, however, only a thin layer of 1 mm is considered in this model as the heat transfer of heat sinks is usually convective and can not be defined by

Table 4.3. Power module thermal parameters for Cauer model.

Layer	i	A_{he} [mm^2]	$R_{\text{th},i}$ [K/W]	$C_{\text{th},i}$ [J/W]	$\tau_{\text{th},i}$ [ms]
Silicon die	1	42.25	0.0319	0.0152	0.486
Die attach	2	42.25	0.0379	0.0046	0.173
Copper (top)	3	46.24	0.0162	0.0478	0.775
Aluminium oxide	4	55.95	0.2515	0.0746	18.77
Copper (bottom)	5	66.59	0.013	0.0688	0.775
DCB solder	6	72.93	0.0219	0.0079	0.173
Baseplate	7	135	0.0555	1.3958	77.53
TIM	8	214.6	0.2541	0.0135	3.44
Heat sink	9	245.9	0.0254	0.5974	15.19

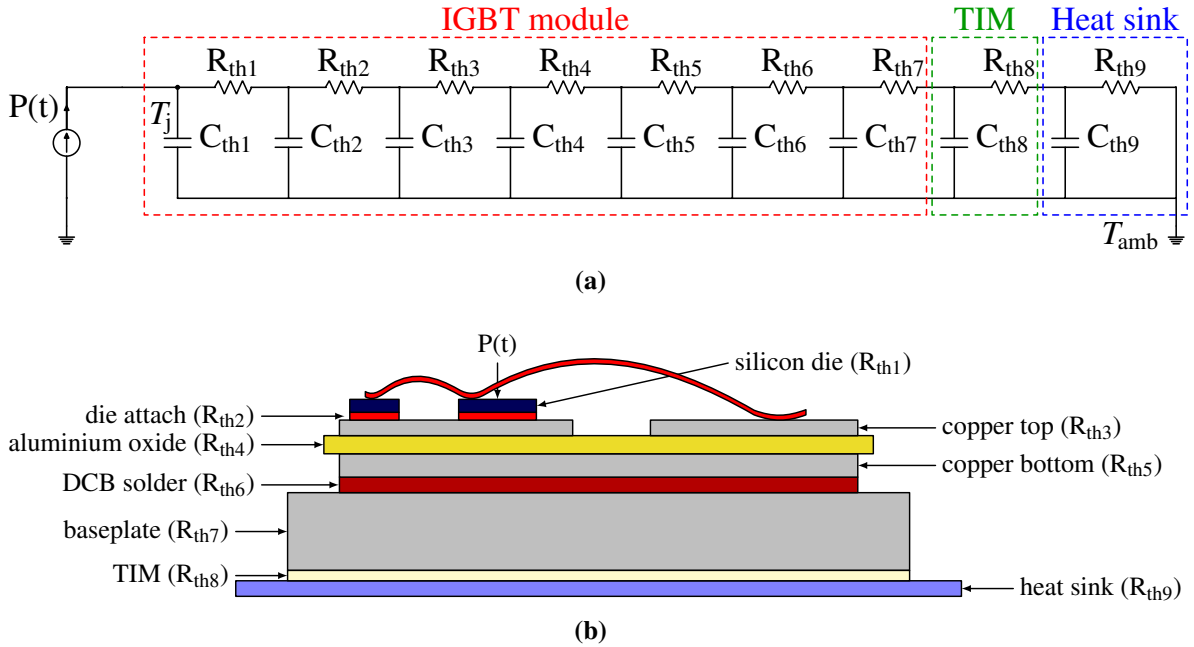

Fig. 4.5. Constructed 1-D Cauer model for IGBT power module: (a) network and (b) physical model.

(4.4)–(4.5). Hence, for the constructed Cauer network the heat sink acts as a convective boundary layer coupled to the ambient temperature, T_{amb}. The final Cauer network is shown in Fig. 4.5.

The thermal model was built in PLECS and evaluated by comparing the transient thermal impedance against the one provided in the manufacturer's datasheet, as shown in Fig. 4.6. The thermal impedance from the junction to the case (i.e. the baseplate) of the device (Z_{thjc}) is calculated by rearranging (4.1):

$$Z_{thjc} = \frac{T_j - T_{hs}}{P_{sp}} \tag{4.8}$$

where P_{sp} is a single power loss pulse of predefined duration. Fig. 4.6 validates the accuracy of the Cauer model, as the slopes of the two curves are similar throughout the whole transient response. Some error in the absolute value of the thermal impedance exists that could be caused by inaccuracies in material properties and geometries, as well as assumptions made throughout the development process. As already mentioned, the Cauer model is only intended to be used for the investigation of heat sink effect on T_j and not as a temperature sensing tool, thus, any small errors of the T_j estimation are insignificant and can be neglected.

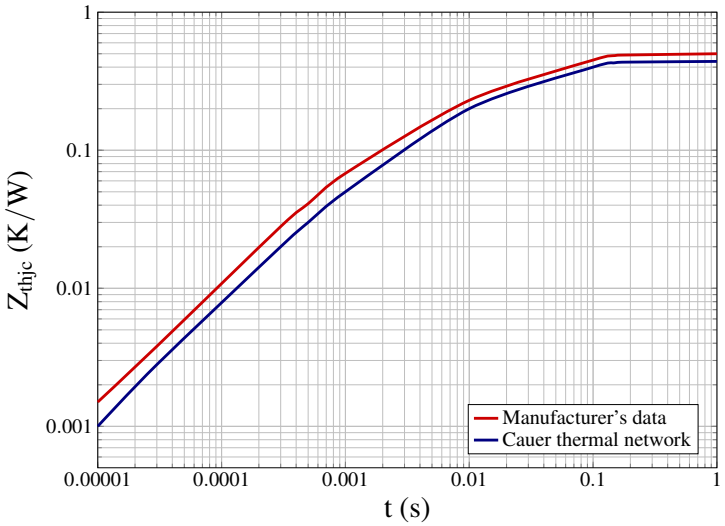

Fig. 4.6. Transient impedance, Z_{thjc}: simulation and manufacturer's datasheet.

The developed thermal network was used in order to investigate the effect of the cooling system on the junction temperature of the IGBT device. Fig. 4.7 shows the simulated transient response of the junction temperature over time. The thermal resistance representing the heat sink, R_{th9}, was the only variable parameter between the simulation trials, whereas parameters such as input power losses, P(t), and ambient temperature, T_{amb}, were fixed at 50 W and 30 °C, respectively. The selected R_{th9} values are based on electronics heat sinks, ranging from forced–air cooling to water–based cold plates at different fluid flow rates [**? ?**]. From the simulation results it is evident that T_j is directly associated to the heat sink's thermal resistance, which further highlights the significance of effective cooling for power electronic devices.

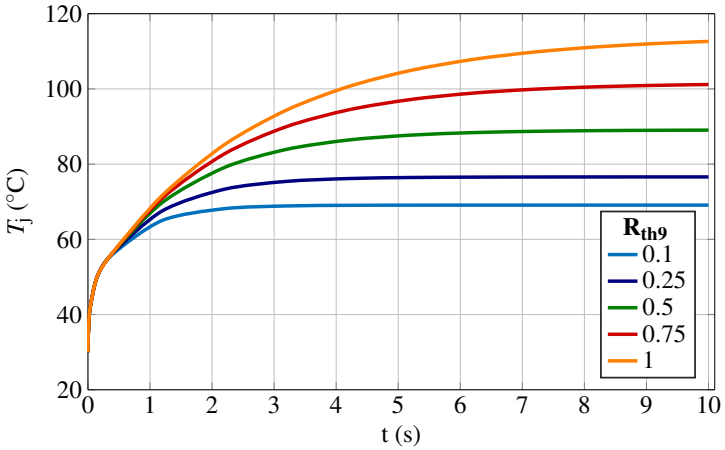

Fig. 4.7. Transient thermal response of T_j for different heat sink thermal resistance.

4.2 Junction temperature measurement for power module

The measurement of the junction temperature, T_j, for power electronic devices is an interesting yet challenging topic of ongoing research. Knowledge of T_j is vital in many ways; it can be used to prevent the electronic device from thermal runaway, as well as a reliability tool, used for both condition monitoring and estimation of the device's RUL. In addition to the mathematical models mentioned in Section 4.1, which are used for estimating T_j, the measurement of the chip temperature can be achieved in three ways: (i) optical measurements, (ii) physical contact measurements, and (iii) electrical parameters measurements. Typical temperature measurement via an optical method for power electronic applications include infrared cameras [**?**] and microscopes [**?**], as well as laser deflection [**?**]. The main advantage that optical temperature measurement techniques offer is the ability to provide a complete map of the temperature distribution within the heated area. This feature allows for studying the temperature distribution within a power module that consists of multiple paralleled IGBT chips. Moreover, optical methods have very high accuracy and are frequently used for research purposes, yet it is unlikely to be implemented in an industrial application. The implementation of an optical method is rather expensive and requires modifications to the power module package, such as removing the top plastic cover and the dielectric gel, which makes it unsuitable for high voltage applications.

Temperature measurement within a power module can also be achieved via a physical contact method between the chip and a temperature sensitive material. Usually, thermocouples or thermistors are utilised to obtain the chip temperature [**?**], although the use liquid crystals and thermographic phosphors has also been reported [**?**]. Physical contact methods are cheap and reliable, however, the dynamic response of the temperature measurement is very slow compared to the fast transients of the junction temperature of a power electronic device in operation. In addition, compared to optical methods, they only provide local temperature measurements, which could lead to erroneous results.

Finally, an indirect method, such as a temperature sensitive electrical parameter (TSEP), can be utilised to determine the junction temperature, T_j. As the implementation of a TSEP only requires acquisition of voltage or current signals, or both, T_j can be measured without physical

access inside the power module package. Hence, TSEPs can be used in high voltage applications. Additionally, fast signal acquisition and temperature estimation is achievable with this temperature sensing method, thus making them suitable for fast thermal transients often found in power electronics applications. The temperature measurement via an electrical parameter, however, only provides a virtual temperature of the power electronic switch. Consequently, the temperature distribution in the chip's area cannot be determined. Although for single chip devices the virtual temperature can be very close to the junction temperature, TSEPs could yield significant errors for temperature sensing of multichip devices.

The dependency of electrical parameters on the junction temperature of the device can be established by numerous methods for IGBT devices. Some of the most common TSEP techniques presented in literature are the on–state voltage ($V_{CE\text{-}on}$) for low ($<$1 A) [**?**] and high [**?**] forward conducting current, threshold voltage [**?**], saturation current [**?**], turn–on delay [**?**] and turn–off delay [**?**].

In this work, the chip junction temperature is required to evaluate the thermal properties of the heat sink, therefore, an indirect method via a TSEP was used for its measurement. More specifically, the temperature dependency of $V_{CE\text{-}on}$ on T_j for IGBTs at a low forward conducting current is selected because of its straightforward implementation, easy calibration, linearity and high sensitivity. In addition, the utilisation of a TSEP rather than an optical method or a thermocouple allows for measuring the dynamic response of T_j, which is further discussed in Chapter 5. The main disadvantage of this method is the added complexity when implemented for temperature sensing during normal operation of the device, however, in the current experimental setup it is not required.

The relationship between T_j and $V_{CE\text{-}on}$ is obtained through a preliminary TSEP calibration test, where a temperature controlled hotplate is attached to the baseplate of the IGBT power module, thus heating it externally. A schematic diagram of the calibration process is shown in Fig. 4.8. Three thermocouples (T1–T3) are placed between the hotplate and the IGBT power module to ensure that the temperature distribution across the baseplate area is even.

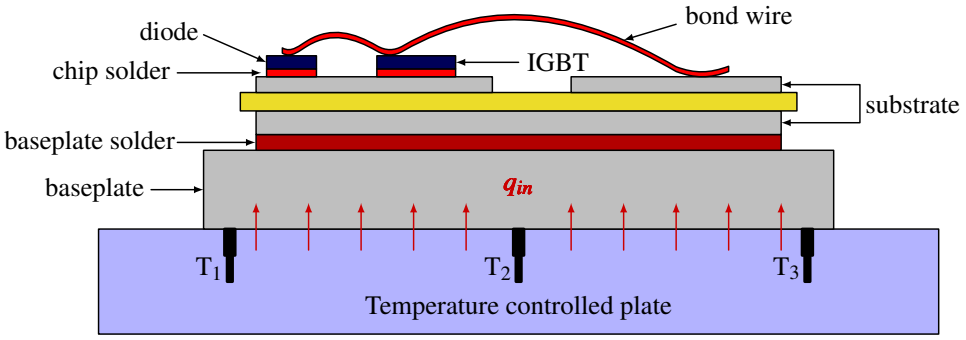

Fig. 4.8. Schematic of temperature controlled plate for TSEP calibration.

During the calibration, the IGBT switch is in its forward conducting state by applying a constant +15 V at the gate–emitter terminals while a low forward conducting current (I_{sense}) flows through it. Due to its low amplitude, the I_{sense} current is used for temperature sensing without contributing to the self–heating of the IGBT device [**?**]. The schematic diagram of the constant current source, I_{sense}, is shown in Fig. 4.9, which is based on the LM317 adjustable voltage regulator. The output current of the constant current source, I_{sense}, is calculated as:

$$I_{sense} = \frac{1.25}{R_{sense}} \tag{4.9}$$

The calibration process was performed for a current I_{sense} from 50 to 200 mA in 50 mA intervals, in order to select the sense current that provides the highest resolution. To ensure that the IGBT module had reached thermal equilibrium, a $V_{CE\text{-}on}$ reading was taken after all three thermocouples and $V_{CE\text{-}on}$ values were constant.

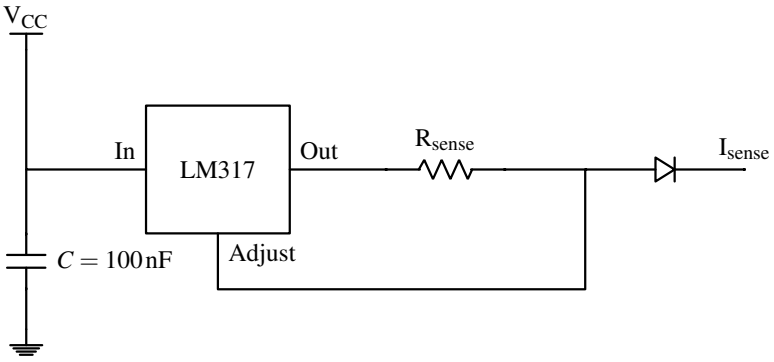

Fig. 4.9. Sense current, I_{sense}, circuit diagram.

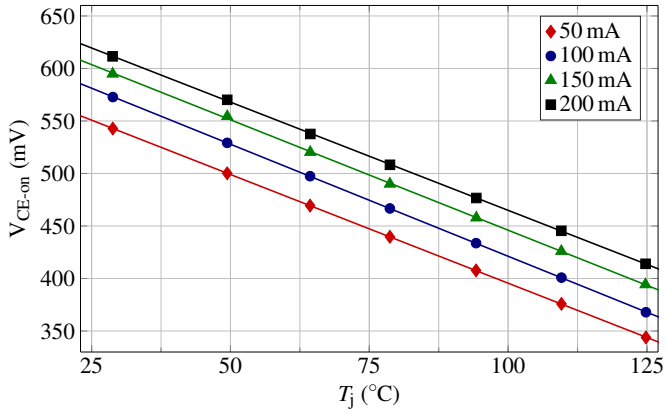

Fig. 4.10. TSEP calibration curves for various sense currents.

The results of the TSEP calibration are shown in Fig. 4.10. The value of 100 mA was selected as sense current for temperature measurement of the IGBT device, as it provides the highest resolution ($-2.14\,\mathrm{mV/°C}$). In addition, the R^2 value of the graph approaches 1, thus indicating a very good linear regression of the curve. Hence, for a constant sense current of 100 mA and a given $V_{CE\text{-}on}$, the junction temperature, T_j, is defined as:

$$T_j = 297.39 - 468.67 \cdot V_{CE\text{-}on} \tag{4.10}$$

4.3 Liquid metal MHD heat sink for IGBT power module cooling

The design and development of an effective and efficient convective heat dissipation mechanism is a challenging process that depends on many individual parameters. One of the most important aspects that determine the cooling performance of the system is the heat transport agent, which is responsible to move the heat from one medium to another. The $Ga_{68}In_{22}Sn_{10}$ liquid metal is selected for the proposed heat sink. It is a non–toxic and non–flammable eutectic alloy composed of 68% gallium, 22% indium and 10% tin in weight. The thermophysical properties of $Ga_{68}In_{22}Sn_{10}$, which are similar to the Galinstan[1] alloy, are shown in Table 4.4. Compared to

[1]Galinstan is the commercial name for the eutectic alloy with 68.5% gallium, 21.5% indium and 10% tin made by Geratherm Medical AG.

Table 4.4. Thermophysical properties of liquid metal and water.

Property	Unit	Water	$Ga_{68}In_{22}Sn_{10}$
Density	kg/m^3	998	6400
Melting point	°C	0	-19
Boiling point	°C	100	>1300
Specific heat capacity	$J/(kg \cdot °C)$	4081	365
Dynamic viscocity	$Pa \cdot s$	0.001	0.0024
Electrical conductivity	S/m	$5.5 \cdot 10^{-6}$	$3.46 \cdot 10^{6}$
Thermal conductivity	$W/(m \cdot °C)$	0.606	16.5
Prandtl number	—	6.62	0.027

water, which is widely used as a cooling medium for power electronic applications, $Ga_{68}In_{22}Sn_{10}$ has a much lower specific heat capacity. Hence, its volumetric heat capacity that is defined as the product of specific heat capacity and fluid density in (4.11), is about 55% lower compared to water's volumetric heat capacity. Nonetheless, $Ga_{68}In_{22}Sn_{10}$ has a higher cooling capability due to its high thermal conductivity, which is approximately 27.2 times larger than water's thermal conductivity. Other design parameters of the heat sink include the geometry of both the pump and the heat exchanger, as well as material selection and are discussed in detail in section 4.3.1.

$$C_{\mathrm{v}} = \rho \cdot C_{\mathrm{p}} \tag{4.11}$$

4.3.1 MHD pump design

The self–contained liquid cooling system consists of two parts; a MHD pump head with direct immersion cooling and a U–type tubular liquid–to–water heat exchanger with connection pipes. The Semikron power module, which is used as the device under test (DUT), is bolt on the pump head and there is a direct interface between the backside of the baseplate and the liquid metal coolant, thus eliminating any thermal resistance caused by the TIM in traditional liquid cooling methods. The coolant flowing is confined to the designed liquid block and directed by two narrow slots in the nylon housing, as shown in Fig. 4.11.

The liquid block of the heat sink is sealed with an o–ring. The heat source is in direct contact with the liquid metal, which impinges the baseplate as illustrated by Fig. 4.12. Two MHD

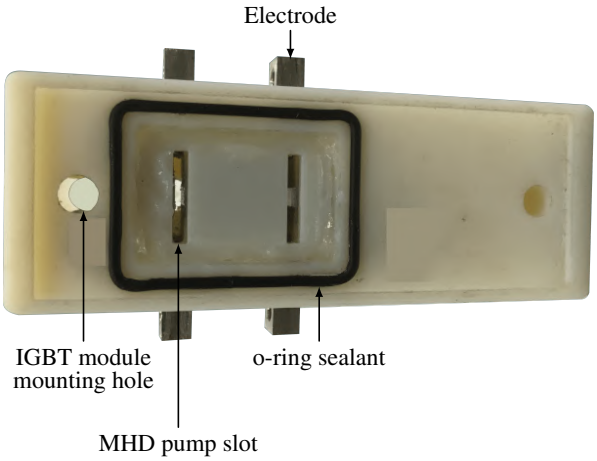

Fig. 4.11. Bottom view of the liquid metal heat sink prototype.

micro–pumps are integrated in the plastic housing, where totally five magnets are embedded in x direction and a pair of nickel electrodes is embedded in y direction and thus, perpendicular to the magnets. The U–type heat exchanger and the pump head are connected with two short pipes to form a closed loop. The pump is positioned beneath one IGBT chip of the half bridge module, as this is the only one used in the experiment. The 3–D printed housing of the pump head is made of engineering plastic (VeroWhite), which is able to provide good electrical insulation, good

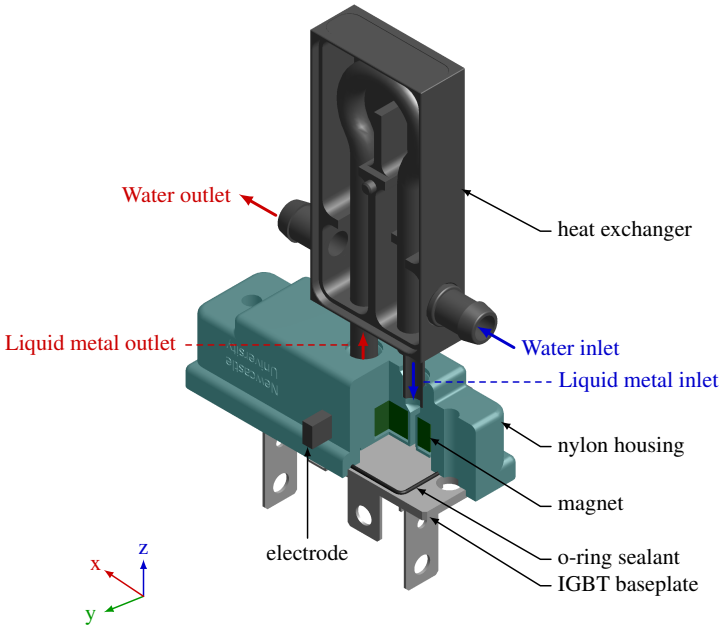

Fig. 4.12. Isometric view of the heat sink and IGBT module.

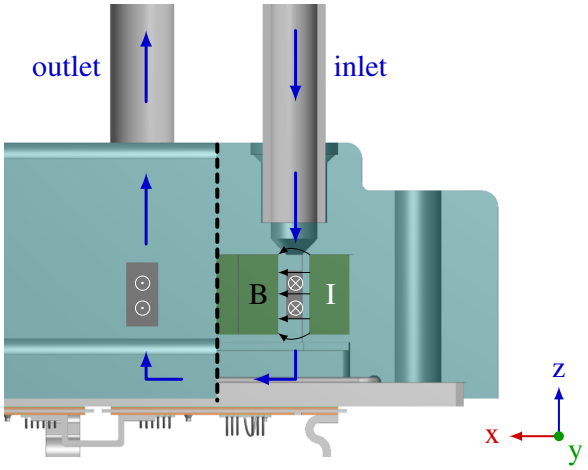

Fig. 4.13. Working principle of MHD liquid metal pump.

waterproofness, good chemical resistance and sufficient rigidity. The main disadvantage of the selected material is its relatively low glass transition temperature T_g, which equals 52 °C. That is the point at which the material transitions from hard to soft. The 3–D printed material is utilised in this study to demonstrate the effectiveness of the proposed heat sink in the heat management of the IGBT power module in a laboratory environment, however, for a real–case application, a material with a higher T_g should be selected.

The working principle of the MHD pump is shown in Fig. 4.13. As there is a constant magnetic field in x plane, injecting current through the electrodes in y plane, generates Lorentz force in z plane that is used for driving the conducting fluid in the channels of the pump. When a current is applied across the width of a channel filled with a conductive fluid subjected to an orthogonal magnetic field, the Lorentz force exerts body force on the fluid that is proportional to both the generated current density **J** in the fluid and the magnetic flux density **B**, as expressed in (3.16).

The main aim when designing the MHD pump geometry is to increase the driving pressure and reduce the flow resistance, thus resulting in a coolant flow rate increase for a given input power. It is evident from Fig. 3.4 and (3.17) presented in Chapter 3 that the only geometry parameter affecting the driving pressure, P_{MHD}, is the active channel height b_{ch}. Hence, the three examples of channel width a_{ch} shown in Fig. 4.14 can achieve the same P_{MHD}, however, geometry (a) has the lowest flow resistance. Therefore, a direct channel of the same width as the hydraulic diameter of the system is selected.

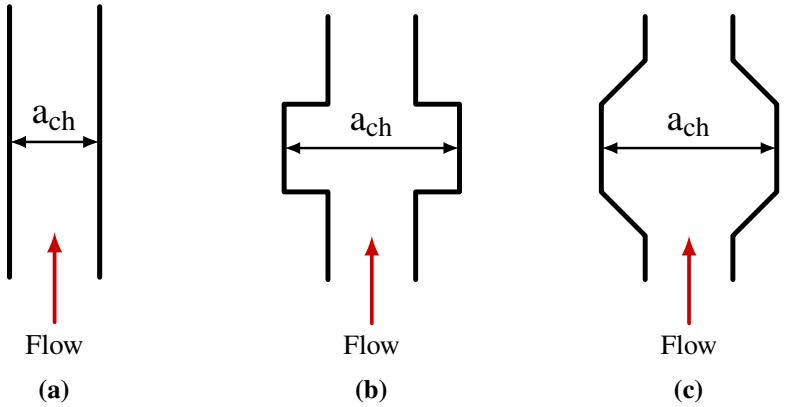

Fig. 4.14. Active channel pump designs: (a) direct, (b) rectangular and (c) trapezoidal channel width a_{ch}.

Table 4.5. Liquid metal MHD pump design parameters.

Parameter	Symbol	Unit	Value
Cross sectional area of MHD channel	A	mm^2	20
Magnetic field cross sectional area	A_{mag}	mm^2	100
Efficient magnetic flux density	B_{eff}	T	0.3
Liquid metal pipe radius	r	mm	3
Channel distance between magnets	d	mm	2
Coefficient 1	C_1	—	1.085
Coefficient 2	C_2	—	0.0123

Similarly, the flow resistance is also affected by the channel height, b_{ch}. Hence, there is a trade–off between the driving pressure and flow resistance when considering b_{ch}. As the system is described by a pressure driven laminar flow, the relationship between the pressure developed and mean velocity can be derived based on (3.17):

$$P_{MHD} \approx \frac{B_{eff} \cdot I_{pump}}{b_{ch}} \approx C_1 \cdot \rho u^2 + C_2 \cdot \rho u \tag{4.12}$$

where C_1 and C_2 are the coefficients of flow resistance through the system, considering pumps, piping and the tank of the loop. Therefore, the value of b_{ch} that provides adequate driving pressure and volume flow should be selected. Finally, the channel length c_{ch} is constrained by the magnets length.

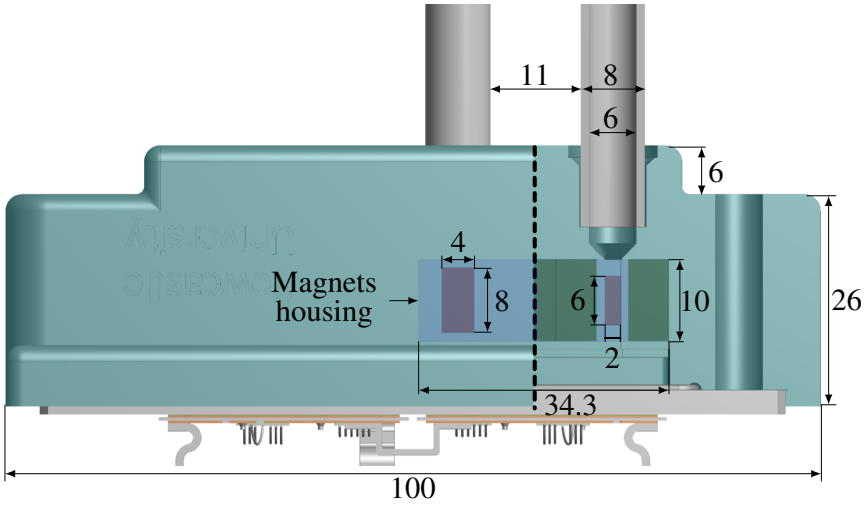

Fig. 4.15. Dimensions of the MHD pump in mm (front view).

The flow rate across the pump, Q, can be expressed as:

$$Q = uA = \left(\left({C_2}^2 + \frac{8 B_{\text{eff}} \cdot I_{\text{pump}}}{\rho \pi r} \right)^{\frac{1}{2}} - C_2 \right) \cdot \frac{\pi r^2}{2C_1} \tag{4.13}$$

where r is the radius of the tube. Equation (4.13) shows a straightforward relationship between the flow rate Q and the applied current I_{pump}, which can be used to calculate the coolant's flow rate. In this work, coefficients C_1 and C_2 were determined by computational fluid dynamics (CFD) simulations [2], whereas B_{eff} was obtained empirically. Hence, for a specific current value, the flow rate can be predicted and applied in the CFD simulation to estimate the thermal characteristics of the liquid metal heat sink. The design parameters for the developed pump are shown in Table 4.5 and Fig. 4.15.

4.3.2 CFD simulation

The conjugate heat transfer of MHD pump was simulated in ANSYS CFX 12.0, in which 3–D steady Reynolds–averaged Navier–Stokes (RANS) equations are solved for the fluid flow and energy equations are solved for fluid and solid simultaneously for the heat transfer. The geometry and material properties of the IGBT power module that were presented in Table 4.2 are used in the simulation model. A few basic settings and assumptions are applied for the simulation i.e.

[2] A detailed explanation on calculating coefficients C_1 and C_2 is available in Appendix B.

Table 4.6. Simulation boundary conditions.

Parameter	Unit	Value
Inlet static pressure	Pa	10^4
Outlet static pressure	Pa	0
Inlet fluid temperature	°C	20

(i) the flow is incompressible, (ii) the buoyancy and radiation heat transfer are not taken into account and (iii) the thermophysical properties of the liquid metal are temperature independent. The shear–stress–transport (SST) model is chosen as the turbulence model. Grid independence has also been examined, after which the grid of the solid domain has 111,292 nodes, and the grid of fluid domain has 195,245 nodes, which corresponds to a maximum y+ value of 1.0 on the wall boundary. Smooth wall conditions have been implemented over the wall. High resolution advection scheme is used too for the calculation of the advection terms, and root mean square residual of smaller than 10^{-5} is set as the convergence criterion.

To demonstrate the effectiveness of the liquid metal compared to water as the working fluid of the heat sink, a comparison between the two fluids was performed by running the simulation model for static tests under various heat loads. The boundary conditions for both fluids were the same and are listed in Table 4.6. It should be mentioned that during the simulation process both the IGBT and diode chips are generating heat simultaneously. Hence, thermal coupling between the two heat sources is also considered.

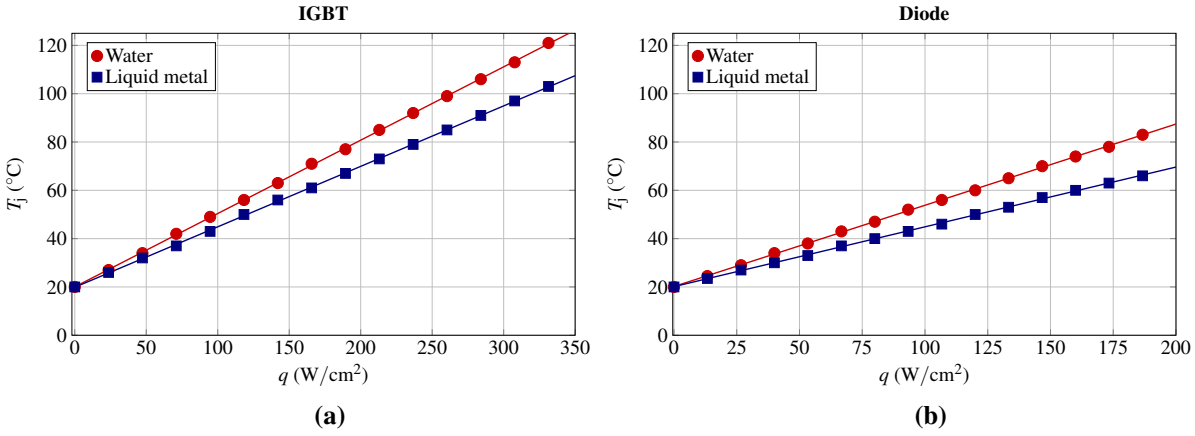

Fig. 4.16. CFD comparison between water and liquid metal coolant: (a) IGBT and (b) diode chips.

The simulation results presented in Fig. 4.16 demonstrate the liquid metal coolant effectiveness compared to water coolant, as there is a reduction of T_{j} under identical working conditions. The overall thermal resistance of the system is reduced from 0.7 to 0.6 °C/W for the IGBT die and from 1.35 to 1 °C/W for the diode die. The liquid metal coolant can therefore cope with higher heat fluxes and keep the junction temperature below $T_{\mathrm{j\text{-}max}}$ under higher heat loads.

4.3.3 MHD pump characterisation

The hydrostatic performance and power consumption of the MHD pump were evaluated through a set of experiments. Firstly, characterisation of the pump for a range of input current values was performed, which is also used to to estimate B_{eff}. Hence, the static pressure (P_{s}) is measured for different current values. Fig. 4.17 illustrates the pump characterisation process. Once the pump is attached to the IGBT module, its slots and the piping system are filled with the liquid metal and positioned vertically. Then, a PWM controlled current, $\mathrm{I_{pump}}$, is injected from a power supply unit (Agilent 6684A) to the pump's electrodes and the height difference (ΔH) between the inlet and outlet tubes is measured at the point where the liquid metal reaches its equilibrium position. In this position only the gravitational force and Lorentz force are acting on the liquid metal. Hence, the P_{MHD} equals the static pressure P_{s}, which can be defined as:

$$P_{\mathrm{MHD}} = P_{\mathrm{s}} = \rho g \Delta H \tag{4.14}$$

where g is the gravitational acceleration. In Fig. 4.18, the static pressure P_{s} is shown as a function of the supplied current $\mathrm{I_{pump}}$. As expected, for a constant magnetic field, the static pump pressure varies linearly with the injected current. Therefore, B_{eff} is estimated by rearranging (3.16) and is shown in Table 4.5.

As highlighted in Chapter 2, the power consumption of the cooling system is an important parameter, as it contributes to the overall power density of the power electronic device. Due to its high electrical conductivity, the liquid metal between the electrodes form a current loop that has a rather small ohmic resistance ($\approx 1\,\mathrm{m\Omega}$) and therefore, very little power is required for driving the coolant, as shown in Fig. 4.19. To define the overall efficiency of the cooling

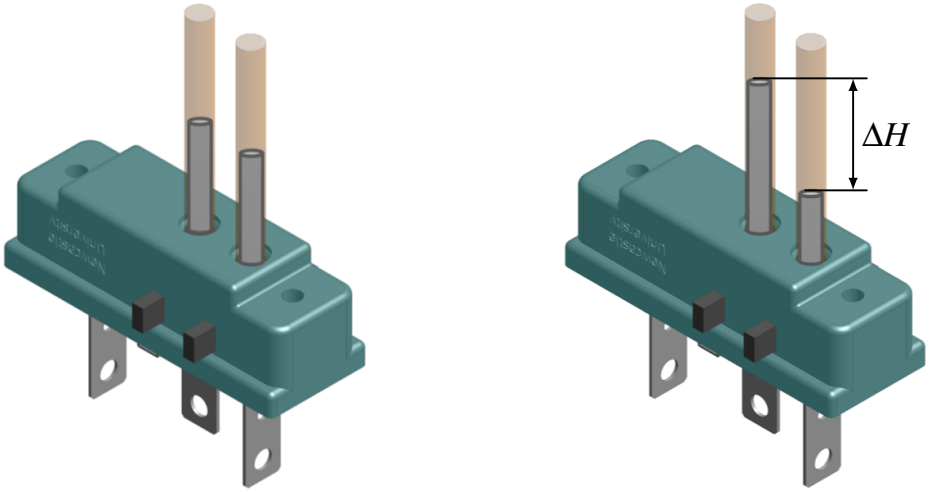

(a) (b)

Fig. 4.17. MHD pump characterisation test with I_{pump}: (a) off and (b) on.

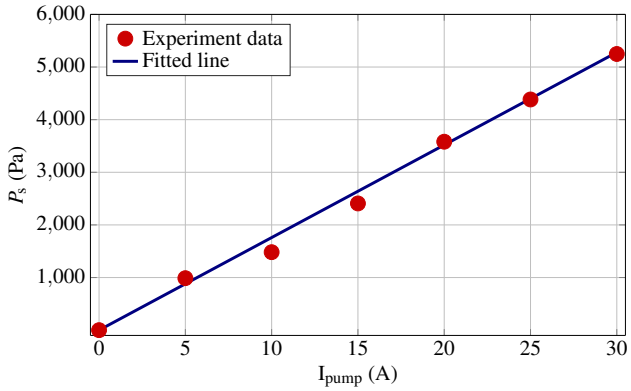

Fig. 4.18. MHD pump characterisation: static pressure P_s as a function of input current I_{pump}.

system, the power required by the water chiller for driving the water in the secondary cooling loop and dissipating the excess heat to the ambient should also be considered. As this work focuses solely on the liquid metal cooling loop, the power required for the water loop is not included in Fig. 4.19. A constant water flow rate of 5 L/min was maintained throughout the experimental validation, resulting in a pressure drop of 1.1 bar across the heat exchanger. Hence, the chiller consumption power for the cooling system is approximately 10 W without taking into account systems connected in series or the efficiency of the water pump. In real applications the secondary cooling medium is often shared among many heat loads (i.e electrical machine, gearbox etc.) or a heat exchanger that is optimised to the needs of the system is designed. Finally,

for applications where cooling efficiency is of paramount importance, a passive heat exchanger can be utilised [**?**].

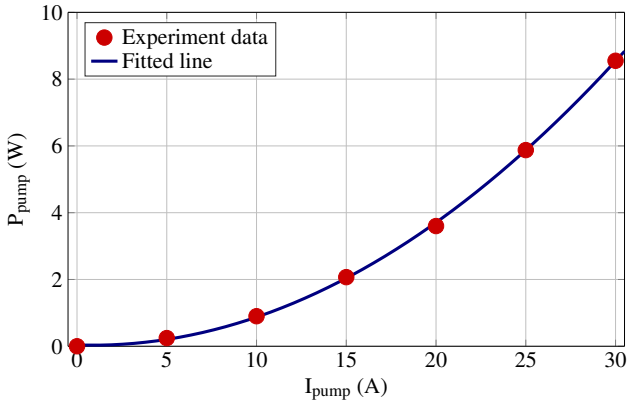

Fig. 4.19. Consumed power of liquid metal pump as a function of the input current.

4.3.4 Experimental test setup and heat sink characterisation

A liquid metal–to–water heat exchanger is employed in this work for its powerful heat dissipation. The heat exchanger uses a U–shaped nickel pipe that accommodates the liquid metal and can be directly jointed with the inlet and outlet orifices of the MHD pump, although soft plastic connectors are used for the ease of experimental connection. The heat exchanger pipe is made of nickel, as this material has high chemical resistivity against $Ga_{68}In_{22}Sn_{10}$. The pipe of the heat exchanger uses the same diameter as the inlet and outlet of the pump, in order to reduce the flow resistance in the loop. The slots of the MHD pump are the only points in the liquid metal loop that are narrower, in order to achieve high pressure for driving the coolant. The pipe is housed in an aluminium tank, which provides a water jacket from a liquid chiller unit (Cosmotec WRA70) with a predefined temperature. Fig. 4.20 shows the schematic drawing and the implementation of the cooling system. A flow meter (Q_w), pressure transducers ($P_{w\text{-}in}$ and $P_{w\text{-}out}$), and thermocouples ($T_{w\text{-}in}$, $T_{w\text{-}out}$, $T_{lm\text{-}in}$ and $T_{lm\text{-}out}$) are used for monitoring the water flow rate, the pressure drop across the heat exchanger and the inlet and outlet temperatures of water and liquid metal, respectively.

The liquid metal heat sink was subjected to a static thermal test in order to evaluate its cooling capability. The schematic diagram of the circuit used for heating and temperature sensing and a

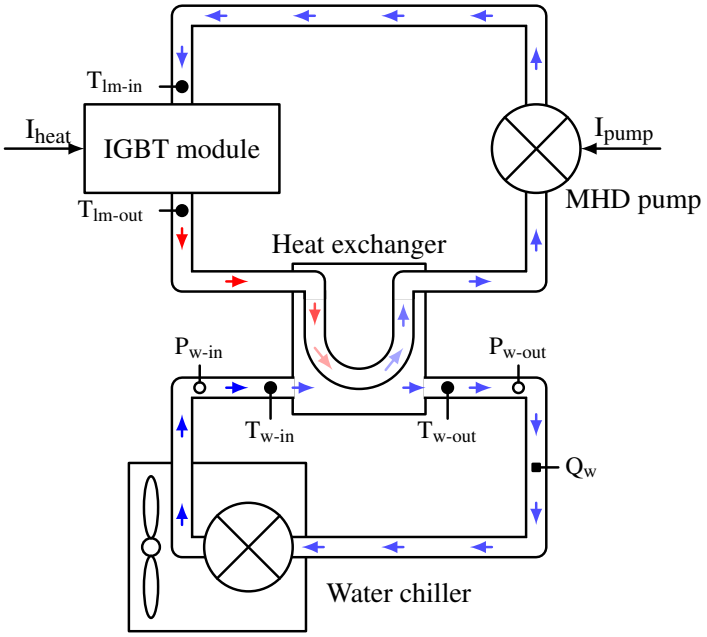

Fig. 4.20. Schematic diagram of the cooling circuit.

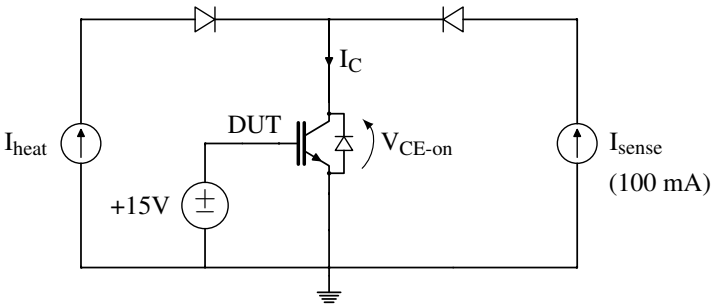

Fig. 4.21. Schematic diagram of IGBT heating and temperature sensing.

picture of the experimental test setup are shown in Fig. 4.21 and Fig 4.22, respectively. The IGBT switch remains in its forward conducting state by applying +15 V across the gate and emitter for the whole duration of the heat sink thermal characterisation process. The TopCon Quadro programmable power supply unit provides a pulsed DC current (I_{heat}) that causes the self–heating of the IGBT device through its power losses, P(t). As there is no switching action during the characterisation process, the heat losses can be easily calculated by monitoring $V_{CE\text{-}on}$ and I_C. Both $V_{CE\text{-}on}$ and I_C are recorded using a Tektronix MSO3014 oscilloscope. The current source I_{sense} is used for calculating the junction temperature of the device. The TSEP measurement takes place when the pulsed heating current I_{heat} is zero and only I_{sense} conducts. A dead time of 1 ms was added before measurement takes place in order to avoid measurement errors caused by

the noise during the turn–off process. Then, five consecutive $V_{CE\text{-}on}$ samples are obtained with a 10 µs delay between them. A median filter is then applied, where the $V_{CE\text{-}on}$ readings are sorted in ascending order and then the third value (i.e the medium value) is used to estimate T_j based on (4.10). An example input waveform, used for both heating the IGBT and measuring T_j, is shown in Fig. 4.23.

Thermal characterisation is essential for evaluating the cooling capabilities of the developed heat sink. During the characterisation process, the water inlet temperature, $T_{w\text{-}in}$, is fixed at 20 °C through the water chiller control interface. Several static results were performed for a range of power losses, P(t), of 0 to 40 W and pumping current I_{pump} of 1 to 15 A, respectively. Fig. 4.24 shows the characterisation process results in a 3–D plot, where the junction temperature is a function of both the MHD pump current and the heating losses. The results can be divided in three segments. In the first segment for a pumping current from 1 to 5 A there is a linear relationship between I_{pump} and T_j for a given P(t). Similarly, there is linear relationship for a pumping current from 5 to 10 A, however, with a smaller slope. Finally, in the third segment for a pumping current from 10 to 15 A the heat sink performance is saturated and the junction temperature is no longer a function of of the liquid metal flow rate. It should be noted that the glass transition temperature of the pump housing (T_g = 52 °C) cannot be exceeded. Otherwise,

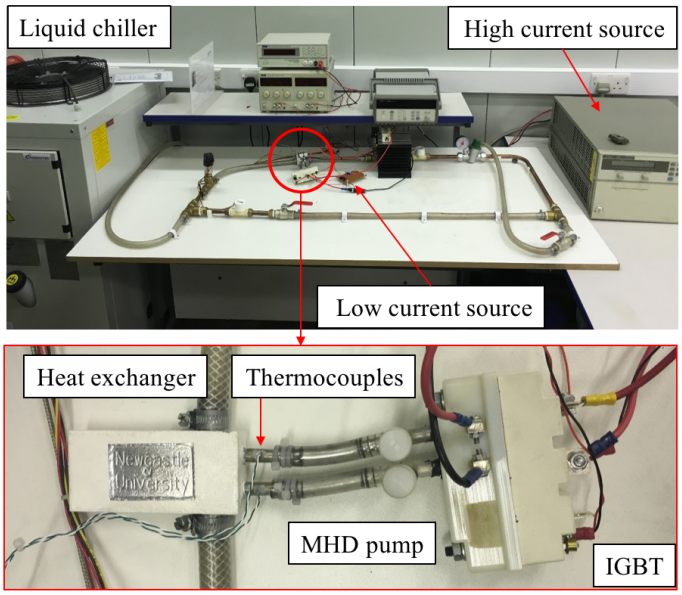

Fig. 4.22. Experimental test setup.

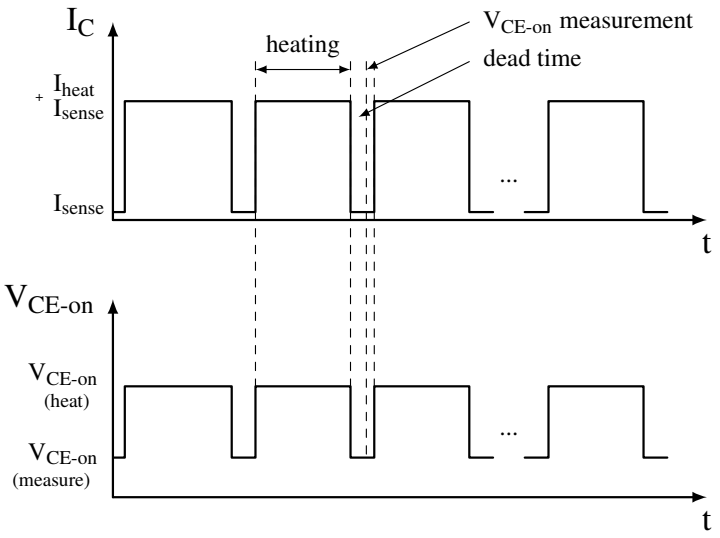

Fig. 4.23. Example waveform for IGBT heating and junction temperature measurement.

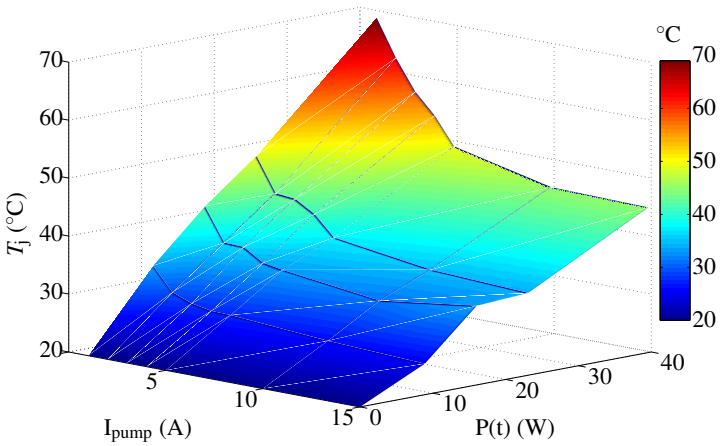

Fig. 4.24. Liquid metal heat sink characterisation results.

the thin nylon walls of the inlet and outlet slots in the liquid block could be damaged, as they are constantly subjected to the magnetic force generated by the embedded magnets of the MHD pump. Therefore, the characterization process for the current design was limited for junction temperatures ranging from 20 to 70 °C. At 70 °C the liquid metal temperature is about 41 °C, which is well below 52 °C.

Fig. 4.25 shows a comparison of the CFD simulation and experimental results of the heat sink thermal characterisation. As shown, there is a strong correlation between the simulation and practical findings from 5 to 15 A, suggesting that the simulation model can be used to extrapolate the results and accurately predict the junction temperature of the device for higher heat fluxes.

As mentioned earlier, operating the IGBT at higher heat fluxes in the practical experiment is not achievable due to limitations in MHD pump body prototype material. For pumping currents below 5 A the MHD flow is not fully developed, as the pressure loss caused by resistance in the channel is comparatively large compared to the total pressure provided by the MHD pump. Hence, the pressure head P_{MHD} does not vary linearly with the pump current I_{pump} in that region.

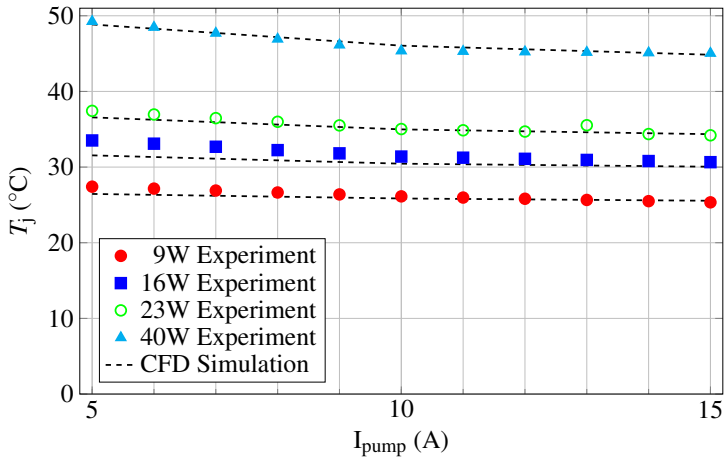

Fig. 4.25. CFD simulation and experimental results comparison of liquid metal heat sink at various heat losses.

Chapter 5

Lifetime extension for power electronic devices

Applications such as offshore wind power, subsea drilling and railway require power converter systems that demonstrate high life spans, considering that the cost for unscheduled maintenances can be extremely high. Many components, such as power semiconductor modules [**?**], capacitors [**?**], and printed circuit boards (PCBs) [**?**] are reliability critical for the power converter operation. Therefore, research for the past few decades has focused on increasing the lifespan and reliability of electronic components. Power semiconductor devices are the most fragile component in a power converter [**? ? ?**], thus, this work aims to increase their lifespan by reducing the thermal stress experienced during large temperature fluctuations.

Fig. 5.1 shows the schematic of a common power module. Its structure consists of many layers of different materials, each one owning a different coefficient of thermal expansion (CTE). During large temperature fluctuations, a shear force is generated between the layers because of the mismatch in the CTE of the power module's materials. Hence, the thermomechanical stress within the layers consequently leads to devices' failures such as bond wire lift–off [**?**] and solder joint fatigue [**?**]. Thus, reducing the thermal stress within the power module structure can prolong the lifetime of power modules and reduce the possibility of a failure [**?**]. A junction temperature control method for IGBT power modules based on a liquid metal heat sink

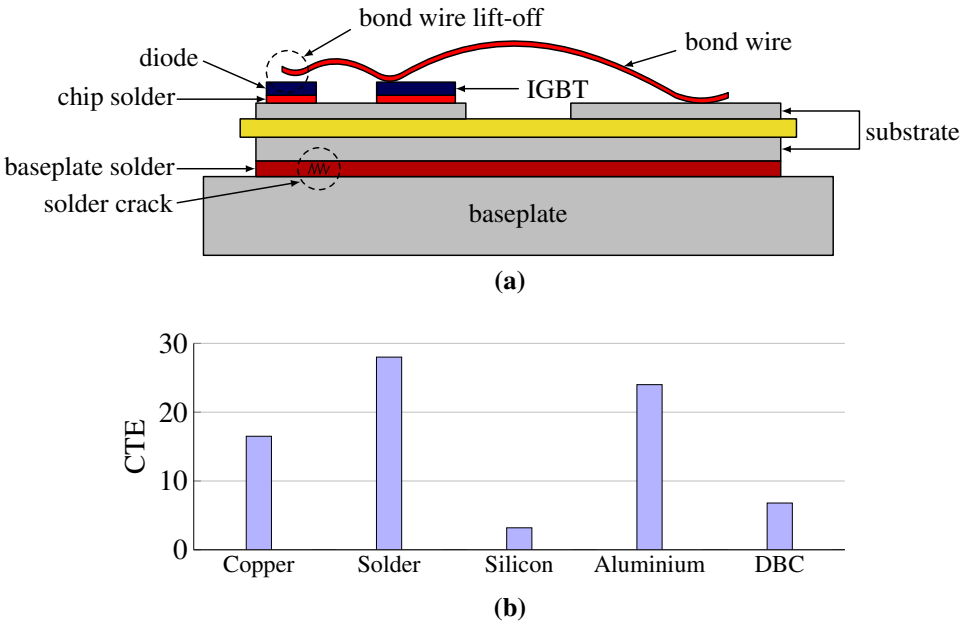

Fig. 5.1. Power module structure: (a) typical failure modes and (b) CTE value of each material in the power module.

is proposed, in which the thermal stress between the device's layers is decreased by reducing the chip's temperature fluctuations.

5.1 Lifetime of power electronic devices

The lifetime of power electronic devices is associated with the temperature cycles of the device during operation. Numerous lifetime models have indicated that the cycles to failure of the device is directly affected by both the junction temperature swing, ΔT_j, and the average working temperature, T_m. An example junction temperature cycle is presented in Fig. 5.2, where T_{max} and T_{min} are the maximum and minimum junction temperature, respectively.

5.1.1 Lifetime models for power modules

A simplified analytical model for estimating the lifetime of a power electronic device is based on Arrhenius model [**?**], stating that the number of cycle to failure (N_f) for a power module is a

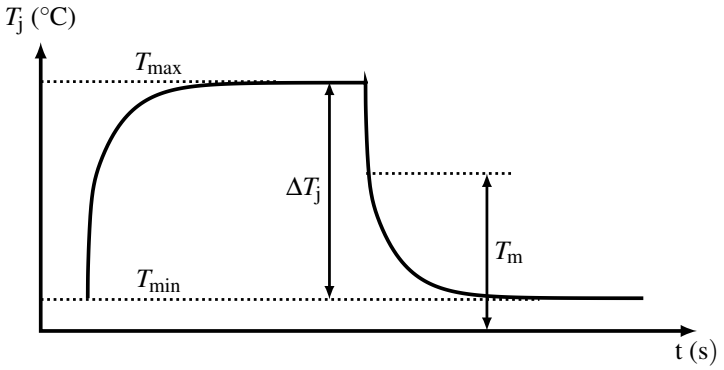

Fig. 5.2. Example junction temperature cycle.

function of the absolute temperature (T_{abs}):

$$N_f = e^{\left(\frac{E_a \cdot N_a}{R \cdot T_{abs}}\right)} \tag{5.1}$$

where E_a is the activation energy, N_a is the Avogadro constant and R is the ideal gas constant. The initial assumption stating that the lifetime of a power electronic chip is halved with every 10 °C increase of T_{abs} is based on that model, however, the junction temperature swing, which is the dominant contributor to lifetime consumption, is not considered in (5.1).

An improved lifetime model was developed in the late 90s by Held *et al.* [**?**] during the LESIT research program, in which the lifetime consumption of power modules is calculated based on the junction temperature swing, ΔT_j, and the mean junction temperature, T_m. Hence, the number of cycles to failure, N_f, is expressed as:

$$N_f = m \cdot (\Delta T_j)^{-n} \cdot e^{\left(\frac{E_a}{k_B \cdot T_m}\right)} \tag{5.2}$$

where m and n are material dependent coefficients and k_B is the Boltzmann constant. The outcomes of the LESIT study are illustrated in Fig. 5.3, clearly showing that the most influencing factor for power modules failures is ΔT_j.

Further research has shown that the lifetime of power electronic modules depends on many other parameters, including the pulse duration (t_{on}), the current amplitude per bond wire (I_D) and other packaging parameters. The model presented by Bayerer *et al.* [**?**] in (5.3), assumes that the blocking voltage capability of the switch and the bond wire diameter are predefined by the

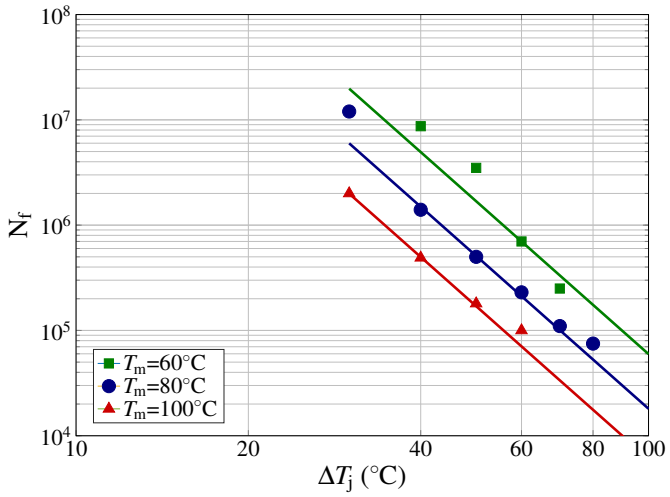

Fig. 5.3. Power cycling results from LESIT project, showing the dependency of power modules lifespan on junction mean temperature and junction temperature swing [**?**].

manufacturer and are therefore not included in the lifetime model. Despite that t_{on} and I_D impact the lifetime of the power module, the operating junction temperature and junction temperature swing remain the main contributors to their lifetime consumption.

$$N_f = m \cdot (\Delta T_j)^{\beta_1} \cdot e^{\left(\frac{\beta_2}{T_{min}+273}\right)} \cdot t_{on}^{\beta_3} \cdot I_D^{\beta_4} \tag{5.3}$$

Fig. 5.4 shows the implementation of the Bayerer lifetime model for a typical Semikron Semitrans power module, where the cycles to failure are presented as a function of ΔT_j and T_{min}. The parameters used for estimating the cycles to failure are shown in Table 5.1 [**?**]. Electrical

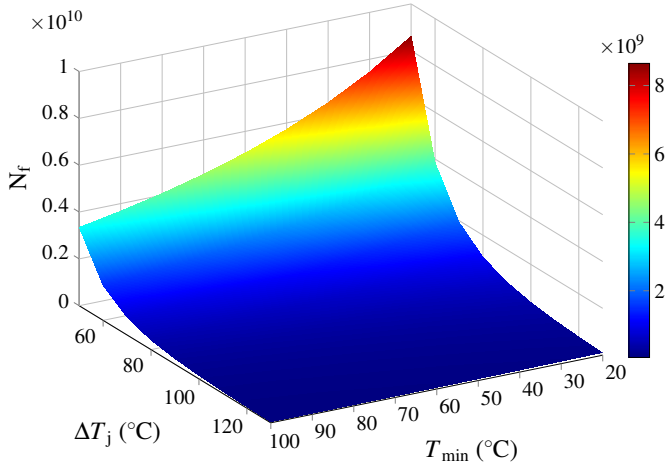

Fig. 5.4. Cycles to failure, N_f, as function of ΔT_j and T_{min} based on Bayerer lifetime model.

Table 5.1. Bayerer lifetime model for Semikron IGBT power module.

Parameter	Symbol	Unit	Value
Current per bond wire	I_D	A	15
Pulse-on time	t_{on}	s	5
Scaling factor	A	—	$1.04 \cdot 10^{15}$
Coefficient	β_1	—	−4.416
Coefficient	β_2	—	1285
Coefficient	β_3	—	−0.463
Coefficient	β_4	—	−0.716

parameters, such as the pulse duration and collector current are identical for all the samples. This lifetime model is only valid for ΔT_j from 45 to 150 °C and T_{min} from 20 to 120 °C. The obtained results demonstrate that in spite of the significant contribution of the operating temperature to the lifetime consumption of the power module, the most influencing factor for the ageing of the power electronic device remains the junction temperature swing, ΔT_j.

The mission profile of the device, which can be either the output power, the output current, or the junction temperature, is arbitrary for a wide range of applications and depends on external conditions. For instance, in electric vehicles and traction applications the mission profile is associated to the driving cycle, whereas in wind turbines the mission profile depends on the wind speed. In addition, each temperature cycle has unique amplitude and duration. Therefore, a mechanism that detects and logs the temperature cycles is often used and implemented in lifetime models.

Several cycle counting methods exist, including peak counting, Hayes method, and level counting, however, rainflow counting algorithm is preferred for most cycle counting of power electronics mission profiles as it is able to capture all the characteristics required for the lifetime model accurately [**?**]. According to rainflow algorithm, the mission profile is defined as a series of pagoda roofs and each peak and valley are water sources from which the rain drop flows down. Fig. 5.5 shows the rainflow algorithm applied on an example mission profile. The rainflow algorithm is based on the following conditions:

- The rain drop stops when it starts from a peak and meets a peak of higher value; for example the red drop that starts from ② and finishes at ④. Similarly, the rain drop stops

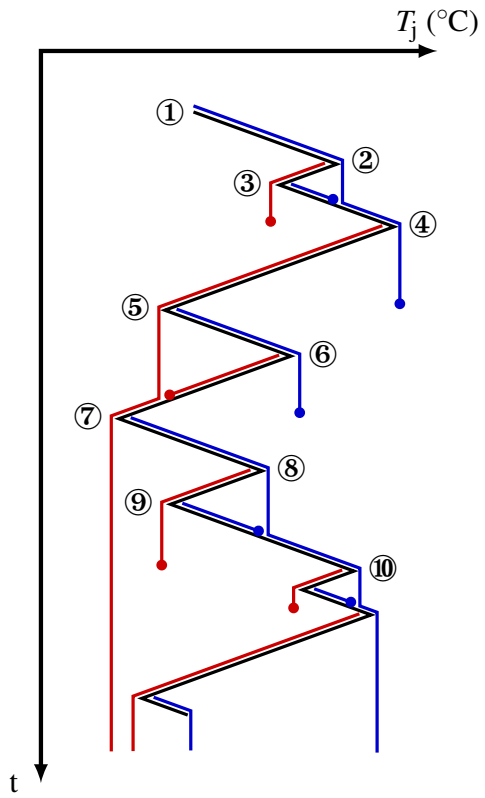

Fig. 5.5. Rainflow algorithm example for temperature mission profile.

when it starts from a valley and meets another valley of lower value; for example the blue drop that starts from ① and finishes at ⑤.

- The rain drop stops when it interacts with a predefined drop; for example the red drop starting from ⑥ and ending before ⑦ and the blue drop starting from ③ and ending before ④.

- The rain drop can continue to travel on another roof, as long as it satisfies the aforementioned conditions.

The rainflow algorithm measures half–cycles for peaks and valleys. Each peak half–cycle is then matched to a valley half–cycle of identical amplitude and duration, thus forming a full cycle that is used in the lifetime model. The models presented in this section give a good insight into the factors that contribute to the lifetime consumption of power modules and the significance of reducing ΔT_j, however, the implementation of a lifetime model and a cycle counting algorithm are out of the scope of this thesis.

5.1.2 Lifetime extension methods for power modules

The expected lifespan of power electronic devices is a multi–objective problem that depends on various factors. The lifetime extension of the devices can be accomplished through different approaches, mainly categorised in (i) the package design, (ii) software–based active thermal controllers, and (iii) adaptive heat sinks. The implementation of each method, as well as its benefits and limitations are discussed in this section.

The lifetime of power electronic devices can be extended by altering the hardware itself. From the manufacturer's point of view, the package technology can be improved. The interconnections between the bond wires and the chips could be improved to avoid bond wire lift–off. In addition, the package of the device could be improved by introducing technologies such as double side cooling in order to increase the heat transfer area. Moreover, the power converter topology has an effect on the lifetime of the power module, as multilevel converters can distribute the stress experienced by the device. Finally, as already mentioned, effective cooling can decrease the mean junction temperature, T_{m}, that also affects the lifetime of the device.

The implementation of software–based active thermal controllers has been widely used in an attempt to reduce the thermal stress within the device's structure. The aim of such controllers is to either decrease the number of thermal cycles or reduce the amplitude of ΔT_{j}, by manipulating the junction temperature, T_{j}. Their principle of operation is based on the variation of electrical parameters of the device during normal operation, such as limiting the load current [**?**], redistributing the power among parallel chips [**?**] and changing the loss distribution [**? ? ?**]. In spite of their easier implementation, these thermal management controllers are not ideal and have significant drawbacks, such as the need for a predefined mission profile in order to operate [**?**], reduction of the IGBT's efficiency [**?**], and requirement for multiple IGBT switches for the scheme to be applicable.

The last method for increasing the lifetime of power module is the utilisation of an adaptive heat sink that controls the chip's junction temperature, T_{j}, by adjusting the rate of cooling. Such cooling devices can add complexity to the system in applications where the cooling medium is shared among many components. The implementation of an adaptive forced–air cooled heat sink

was presented in [**?**] and [**?**], demonstrating an increase in the lifetime of power electronic devices through power cycling tests. Nonetheless, with the ever–increasing power densities of power electronics, air–cooled technologies are unable to dissipate the excess heat [**?**]. In addition, an adaptive TEC was presented in [**?**]. However, as TECs need to dissipate the heat that is being moved from the semiconductor chip and the heat that is generated from its own power, their heat dissipation capability is limited [**?**].

The design, development and fabrication of MHD pumps has been reported for a few cooling applications of electronic devices, because of the ability of liquid metals to dissipate high heat fluxes. Nonetheless, the heat sinks presented in the literature focus solely on protecting the electronic device from thermal runaway by operating the pump at its maximum capability. The simulation and experimental results presented in Chapter 4 have demonstrated a dependency of the device's T_j on the liquid metal flow rate. As already demonstrated by several lifetime models, reducing the temperature fluctuations; even at the cost of operating at a higher mean temperature, could dramatically increase the lifespan of IGBT. Therefore, the proposed adaptive heat sink aims at reducing the amplitude of junction temperature swings, ΔT_j, by altering the input pump current, I_{pump}, and thus, manipulating the thermal resistance of the heat sink. The time lag of the cooling system that is further discussed in this section, also depends on I_{pump} and influences T_j.

5.2 Junction temperature control of IGBT device

In real applications, the temperature profile of power semiconductors is jointly determined by operating and environmental conditions, whose dynamic changes in terms of time constants

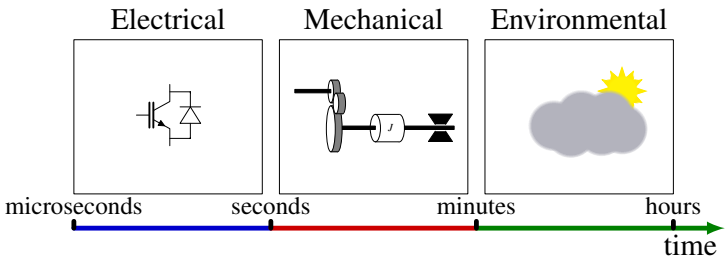

Fig. 5.6. Typical thermal time constants experienced by the IGBT device during operation.

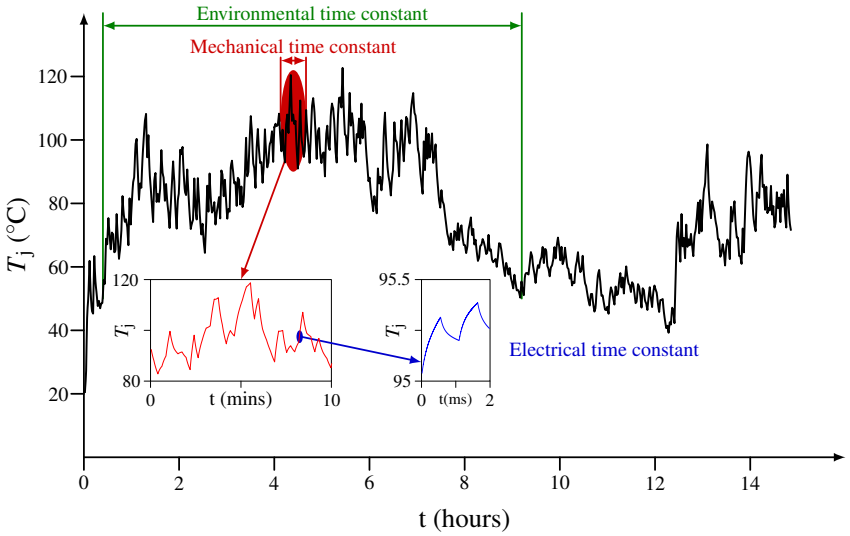

Fig. 5.7. Example junction temperature mission profile.

generally shows diverse differences, as shown in Fig. 5.6. The time constants governing the device and circuit electrical properties usually range from sub–microseconds to milliseconds and are related to the characteristic performance of the switching device and switching frequency, f_s, of the power converter. Similarly, the time constant of a mechanical system typically including the motor drive, shaft and mechanical load could vary from sub–seconds to several minutes. Finally, the long term thermal cycle is associated with environmental changes, such as the day–night and seasonal alternation–driven temperature variation or geographical/spacious relocation–driven temperature changes. Fig. 5.7 illustrates an example mission profile and the different temperature variations caused by each time constant. Power modules are subjected to cyclic thermomechanical stresses resulted from the superposed temperature deviations mentioned above. They are mostly stressed because of load changes with regards to the mechanical system requirement, which is always accompanied by large temperature swings occurring at a substantial frequency [**?**]. Changes associated with environmental temperature contribute to the module ageing, however, they are outperformed by the load cycling [**?**]. On the other hand, temperature cycles caused by the device switching action and circuit topological alternations result in very small amplitude that does not greatly impact the lifetime of a healthy power semiconductor module [**?**]. That is partly because the thermal variation caused by higher frequencies is absorbed by the capacitance of the thermal circuit, and partly because the thermal strain is counterbalanced by the elastic deformation of the power module's materials.

5.2.1 Thermal modelling of adaptive heat sink

In order to reduce the significant thermal cycles dominated by load changes in the mechanical time constant range, the adaptive liquid metal heat sink can be designed to offset the temperature variations by adjusting its inherent cooling performance. This will then reduce the module's fatigue and therefore, increase the lifetime of power semiconductor devices. The proposed temperature control scheme is achieved by employing an actively controlled liquid metal heat sink enabled by the MHD pump that changes the coolant's flow rate in terms of the variation of the junction temperature, T_j.

The Cauer thermal network presented in Fig. 4.5 assumes that the coolant flow rate is constant, thus, the thermal resistance of the heat sink is constant as well. Therefore, the junction temperature becomes only a function of power losses, P(t), and the coolant reference temperature. In contrast, Fig. 5.8 illustrates a Cauer thermal network of an IGBT power module cooled by an adaptive heat sink. The thermal resistance representing the heat sink, R_{thn}, is adjustable and as demonstrated in [**?**], its value is a function of the liquid metal flow rate, Q. Hence, by controlling the variable thermal resistance of the heat sink, the junction temperature swing, ΔT_j, could be minimised. In this thermal model, T_{lm} is the reference liquid metal inlet temperature.

An 8^{th} order Cauer thermal network was developed for simulating the junction temperature of an IGBT die in a power semiconductor module, where the first 7 Cauer elements represent the IGBT device and the 8^{th} element emulates the liquid metal MHD pump. Fig. 5.9 shows the schematic of the circuit including the principal control structure, which was simulated in

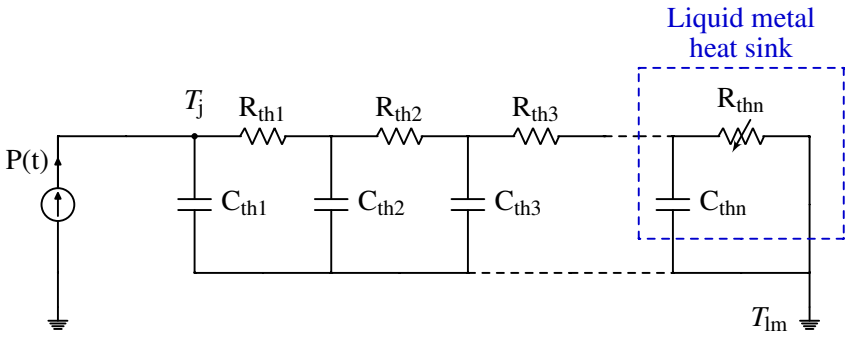

Fig. 5.8. Equivalent thermal network for IGBT with adaptive liquid metal cooling.

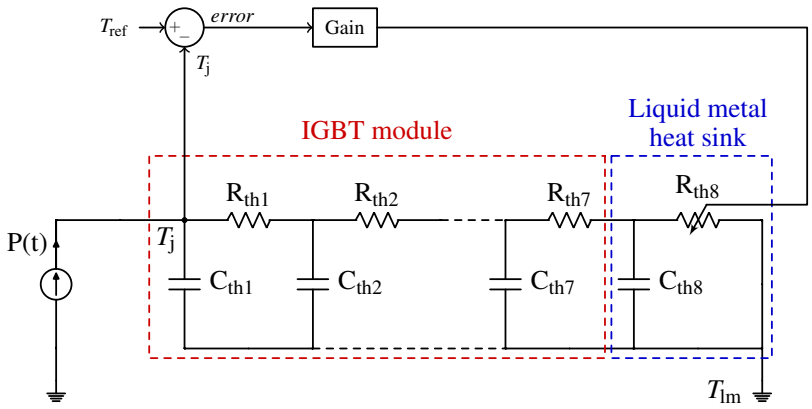

Fig. 5.9. Simulation schematic of IGBT temperature control scheme.

PLECS. The losses of the IGBT switch are emulated by an input signal that is fed to the power source, P(t). The junction temperature is compared to a reference temperature and the error between those two values is fed to a proportional controller. Hence, the value of the variable thermal resistance is changed based on the instantaneous IGBT junction temperature, in order to reduce the junction temperature fluctuation, ΔT_j. A proportional controller was selected, as the proposed scheme considers temperature changes dominated by the mechanical system of a relatively large time constant. The gain value ($k_p = 0.2$) is selected based on the overall thermal resistance boundaries of the system. The thermal parameters of the IGBT module that is used for the experiment are listed in Table 4.3. The traditionally used thermal grease layer is omitted due to the direct interface between the module and the liquid metal. The boundary limits of the heat sink's thermal resistance are set between 0.15 and 3 °C/W and were obtained empirically. It is therefore assumed that the liquid metal flow rate is maximum and zero at the minimum and maximum thermal resistance limits, respectively.

Applications such as electric vehicles, traction, wind turbines and solid state transformers often have mission profiles with large temperature fluctuations that reduce the lifetime of the power converter significantly [**?**]. A metro–system mission profile was selected for this study [**?**], in order to evaluate the impact of adaptive cooling on the junction temprerature of the IGBT device. Power modules used in electric rail traction applications are expected to have at least 30 years of reliable operation that corresponds to several millions of power cycles [**?**].

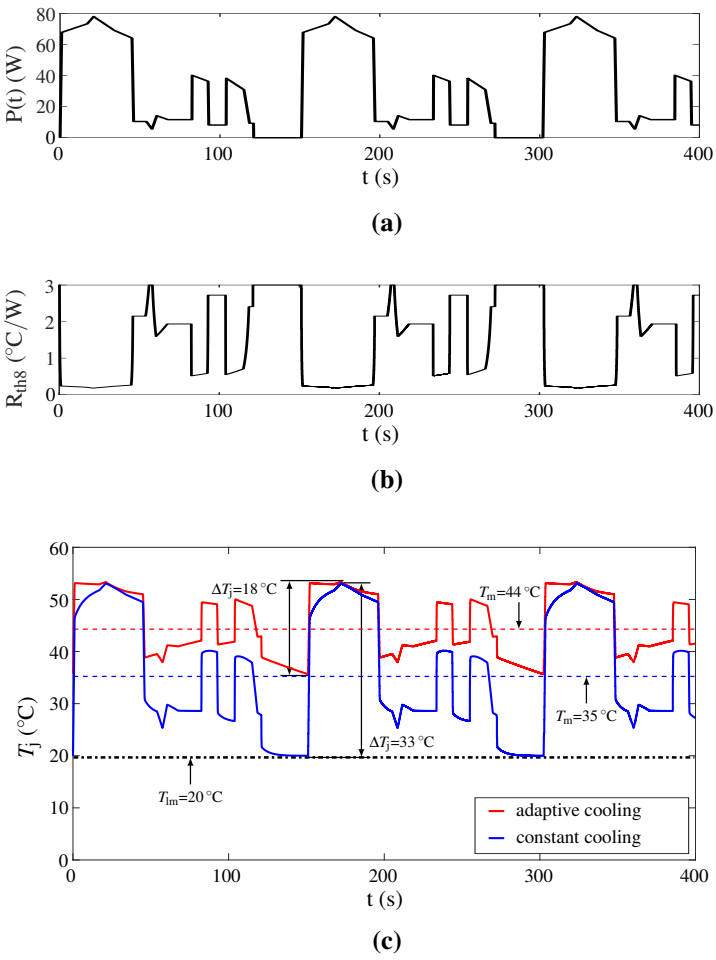

Fig. 5.10. Simulation results for metro mission profile showing, (a) input heat profile P(t), (b) variation of the thermal resistance R_{th8} and (c) junction temperature T_j for constant and adaptive cooling.

The mission profile that is applied to the simulation model is based on a repeating cycle of a total duration of 151 s that consists of the following steps: (i) accelerating for 41 s, (ii) travelling at 60 km/h for 37 s, (iii) braking for 10 s, (iv) travelling at 40 km/h for 11 s, (v) braking for 22 s and finally, (vi) making a complete stop for 30 s. The original mission profile is scaled down, with the maximum load current capped to 50 A to meet the requirements of the selected IGBT module. The maximum current used later in the practical experiment is also limited to 50 A. The simulation results are presented in Fig. 5.10. The scaled mission profile has been converted into a simplified power loss profile P(t) that accounts only for the on–state losses, as shown in Fig. 5.10(a). Based on the actual junction temperature T_j variation and the reference temperature $T_{ref} = 50\,°C$, the controller minimises the temperature swings ΔT_j by manipulating

the thermal resistance R_{th8}. The change of R_{th8} over time is shown in Fig. 5.10(b). It is shown that R_{th8} decreases with rising P(t), and vice versa. During the stop mode of the metro, the MHD pump is commanded to stop pumping liquid metal resulting in a constant high value of $R_{th8} = 3\,°C/W$ during this period, whereas a minimum thermal resistance is required during dynamic accelerating/braking.

Adaptive cooling intends to mitigate the thermal stresses compared to the constant cooling based on the comparison of the junction temperatures, T_j, evolution over the full mission profile. Fixing R_{th8} represents the use of liquid coolant with constant flow rate and this scenario can therefore be regarded as a standard cold plate, as shown in Fig. 4.5. The thermal resistance value for the latter simulation is set to its lowest value of $R_{th8} = 0.15\,°C/W$. Fig. 5.10(c) shows an evident impact on T_j by adjusting the thermal resistance of the heat sink, R_{th8}. Particularly, the junction temperature swings, ΔT_j, are significantly reduced over the course of the repeating cycle. The largest temperature swing reduction is achieved during the acceleration phase from standstill to the top speed of $60\,km/h$. During that period, the amplitude of the junction temperature swing is decreased from $33\,°C$ while operating at a constant cooling to $18\,°C$ in the case where the adaptive cooling is applied. The increase in the mean junction temperature, T_m, is a by–product of the adaptive cooling scheme. As the maximum junction temperature, T_{max}, is almost the same for the two cooling methods and ΔT_j is significantly reduced by using the adaptive cooling, the mean operating temperature will inevitably increase during the operation of the IGBT. Fig. 5.10(c) shows an $8\,°C$ increase of T_m; from $35\,°C$ for the constant cooling to $44\,°C$ for the adaptive cooling. As already highlighted in section 5.1.1, the thermal stress within the module's layers is reduced while T_j is actively controlled, in spite of the higher mean junction temperature of the device.

5.2.2 Liquid metal heat sink control

The simulated temperature control scheme offers an insight into the application of a thermal controller based on an adaptive heat sink and its influence on ΔT_j. Nonetheless, for the implementation of the junction temperature controller in the practical experiment, other factors should also

be considered. Firstly, the simulation model assumes that the heat conduction from the die to the baseplate and the heat convection from the baseplate to the liquid metal coolant is the sum of simplified 1–D heat transfer problems. However, the heat transfer across the layers of the IGBT power module and heat extraction by the liquid metal to the ambient is a much more complicated phenomenon. In the simulated thermal model, the thermal resistance of the adaptive heat sink is adjusted instantly in line with the changing junction temperature, which is not the case for the proposed liquid metal heat sink, as the thermal resistance is associated with the liquid metal flow rate and therefore, a certain period of time is required before it reaches steady state. The cause of the delay in varying the thermal resistance is due to the fact that the MHD pump behaves as an electrical machine and thus, requires some time to reach its steady state [**?**]. Hence, time delays that might occur during the variation of the liquid metal flow rate are not considered. Finally, the implementation of the thermal controller requires accurate junction temperature measurement. Therefore, the TSEP method presented in Chapter 4 is employed for estimating the junction temperature, T_j, of the IGBT device.

The dynamic thermal performance of the heat sink is evaluated for different values of I_{pump} and the system time constant (τ_{MHD}) is derived and illustrated in Fig. 5.11. As shown, the time required for the junction temperature, T_j, to reach its steady state from a predefined temperature of 70 °C is a function of I_{pump}. The time constant of the IGBT module is comparatively small and can be neglected. The results show that τ_{MHD} is dependent on the liquid metal flow rate, and therefore, the MHD pump current I_{pump}. Consequently, at higher input pump current, I_{pump}, heat

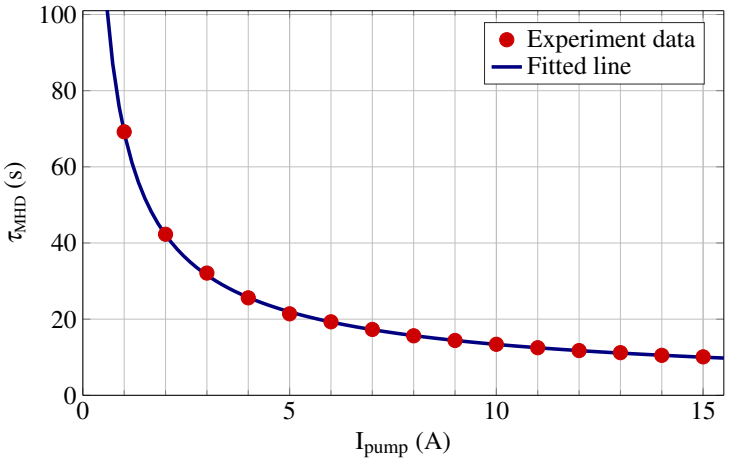

Fig. 5.11. MHD system time constant, τ_{MHD}, as a function of the pump current I_{pump}.

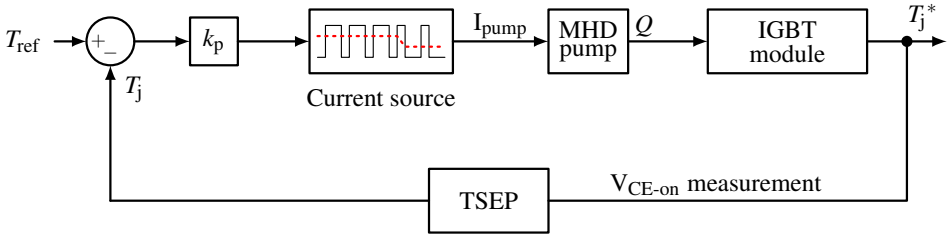

Fig. 5.12. Block diagram of liquid metal heat sink controller.

in the baseplate is removed quicker by the liquid metal coolant. For example, for a given fixed input power loss, a 15 A continuous pump current for 10 s will bring the junction temperature into steady state. As the relationship between the time of heat removal τ_{MHD} and pump current is not linear, an open loop control based on a lookup table derived from the data of Fig. 4.24 cannot be utilised. Therefore, a closed loop controller is used for thermal control of the IGBT.

Fig. 5.12 shows the principal control structure for the junction temperature control experiment. The actual junction temperature (T_j^*) is measured with the help of the TSEP, as indicated in Fig. 4.10. The obtained T_j is compared to a reference value T_{ref} = 50 °C and an error is generated. A proportional controller with $k_p = 0.5$ is used since the system has a very high time constant. The electrodes of the MHD pump are connected to a variable DC current source supply that supplies a maximum of 15 A. A bench power supply (Agilent 6684A) is used as a current source for the MHD pump. The selected power supply is a laboratory equipment and cannot be utilised in a real environment. Instead, for a real–case application, a constant current source that is able to provide the maximum driving current of 15 A with a maximum efficiency of up to 90% can be used [**?**]. The pump current I_{pump} determines the flow rate Q of the liquid metal, which impinges against the baseplate and regulates the junction temperature T_j^* at given power losses.

The schematic diagram of the temperature controller circuit is shown in Fig. 5.13. The dual operational amplifier MCP6042 is selected to measure the voltage between the collector and emitter of the IGBT and to trigger the temperature measurement process. Amplifier A_1 is configured as a differential amplifier that subtracts the emitter voltage from the collector voltage and amplifies the output voltage by 4.7. The reason for that is because the *mbed NXP LPC1768* microcontroller has a 12–bit analog–to–digital (ADC) converter with a maximum input voltage of 3.3 V. Thus, the ADC resolution is approximately 0.8 mV per step. Since the resolution of the

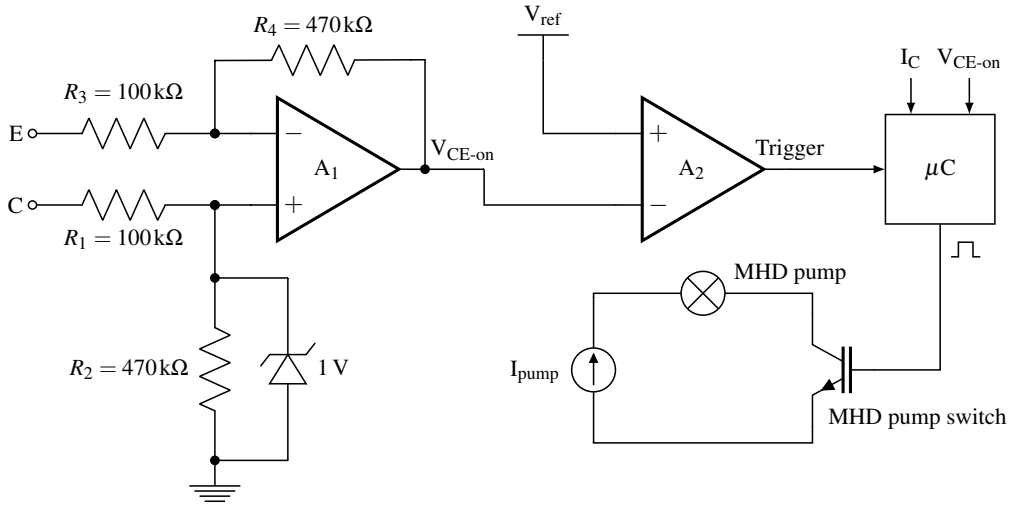

Fig. 5.13. Schematic of temperature control circuit.

TSEP is 2.14 mV/°C and the maximum required voltage is less than 650 mV for temperature sensing, amplification of the input signal allows for utilising the full measurement range of the ADC of the microcontroller, which results in a temperature sensing resolution of 0.08 °C/step. During the heating phase of the IGBT power module the amplified on–state voltage, $V_{CE\text{-}on}$, exceeds the 5 V supply voltage of the operational amplifier, which would saturate its output voltage. In order to avoid that, a 1 V Zener diode was used that limits the input voltage. As the IGBT device is in its forward conduction state throughout the whole experimental process, more advanced overvoltage protection is not required. Amplifier A_2 is configured as a comparator. The amplified $V_{CE\text{-}on}$ signal is fed to its inverting input and compared against a reference voltage. The output of amplifier A_2 is high once the amplified $V_{CE\text{-}on}$ is less than the reference voltage, which initiates the temperature measurement process. Once the TSEP process is executed, the pump current, I_{pump}, is adjusted accordingly, in order to reduce the temperature swing, ΔT_j. The collector current is also monitored and is used in conjunction with the on–state voltage, $V_{CE\text{-}on}$, to calculate the on–state losses of the IGBT chip.

In order to test the temperature sensing circuit the IGBT device was mounted on the temperature controlled plate, in the same configuration as in Fig. 4.8. The IGBT chip temperature is controlled externally, whereas a current pulse of 1 A is emulating the high heating current. The value of 1 A is selected, as it does not greatly impact the junction temperature. The flowchart shown in

Fig. 5.14 describes the testing process. The controller detects the turn–off of I_{heat} and initiates the junction temperature sensing process. Once the IGBT has reached thermal equilibrium, the obtained T_j value is compared to the temperatures measured by the thermocouples. That way, the temperature sensing circuit is verified to obtain accurate temperature readings, which is essential for the operation of the controller.

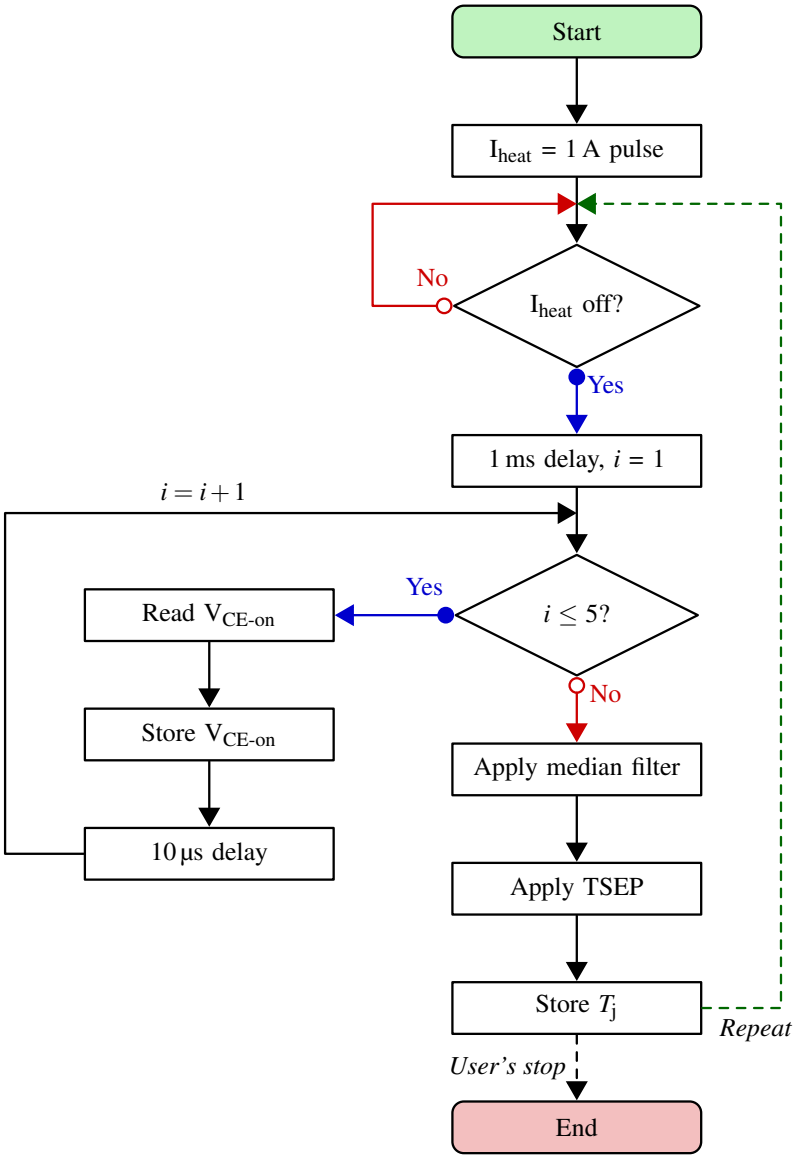

Fig. 5.14. Temperature sensing test with 1 A pulsed current and external heating.

The flowchart describing the temperature controller operation is presented in Fig. 5.15. The maximum temperature of 50 °C is set as the upper limit of the controller. Hence, once the

junction temperature reaches that value, the pump is supplied with 15 A. As mentioned earlier, once the falling edge of the heating current, I_{heat}, is detected, the TSEP measurement takes place and the liquid metal flow rate changes based on the value of T_j.

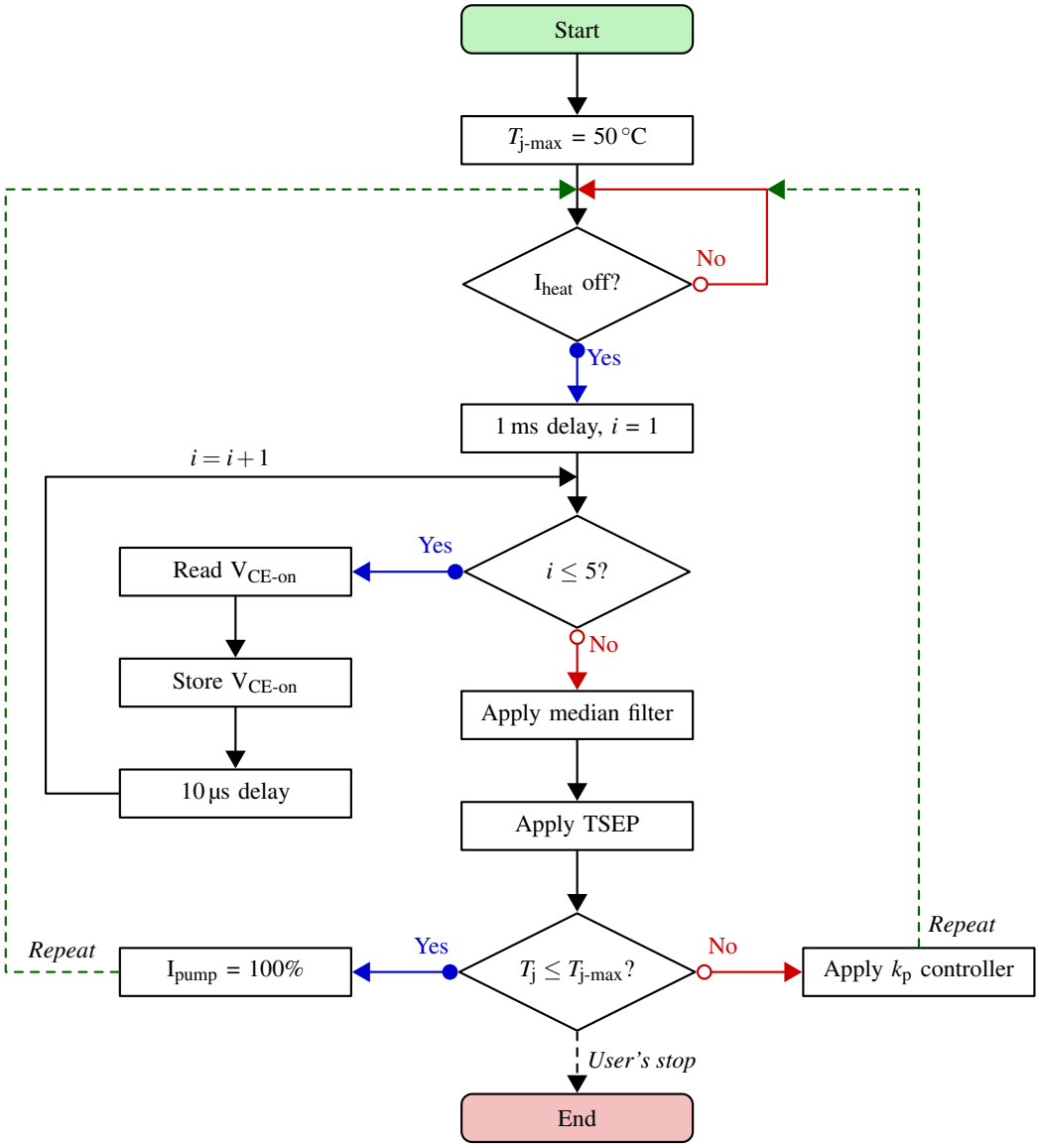

Fig. 5.15. Temperature controller operation.

5.2.3 Experimental validation of the junction temperature control

The experimental testing of the temperature controller focuses on reducing the temperature fluctuations caused by load variations in the mechanical time constant. The metro–system mission profile introduced in section 5.2.1 is applied to generate the heat losses in the IGBT chip. The current profile is scaled down to meet the maximum allowable conducting current specifications of the DUT and is presented in Fig. 5.16.

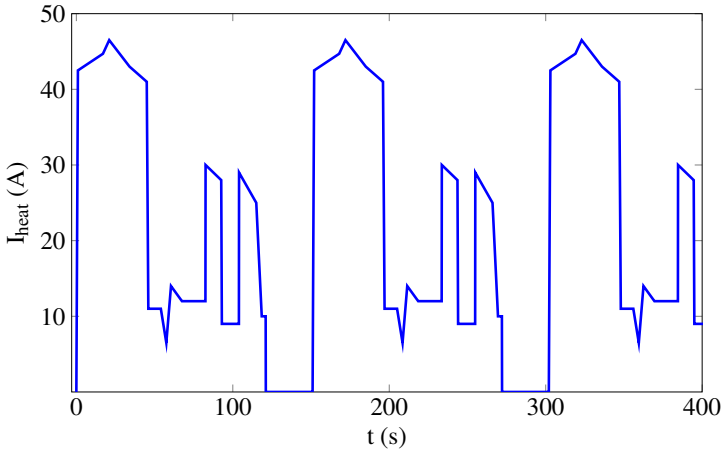

Fig. 5.16. Scaled metro load current mission profile.

The DUT was subjected to the same I_{heat} mission profile of Fig. 5.16 for two tests. In the first test the MHD pump is supplied with the maximum I_{pump} of 15 A throughout the whole experiment. This test emulates a typical heat sink used for protecting the IGBT device from thermal runaway. For the second test, the MHD pump is adaptively controlled by varying I_{pump} from 0 A to a peak current up to 15 A. This test represents a combination of cooling and extending the lifetime of the power module by reducing large temperature swings. The results for both tests are shown in Fig. 5.17. In both experiments the water temperature is fixed at 20 °C. Therefore, the inlet liquid metal temperature, T_{lm} has approximately the same value as the water temperature due to the effective heat transfer properties of the heat exchanger.

Fig. 5.17 shows that the junction temperature swing is greatly reduced with the introduction of the adaptive controller. The largest variations of the temperature are observed during the accelerating and braking phases, as there is a large amount of heat losses during those intervals. Similar to the simulation results, the temperature swing ΔT_j is reduced while the adaptive

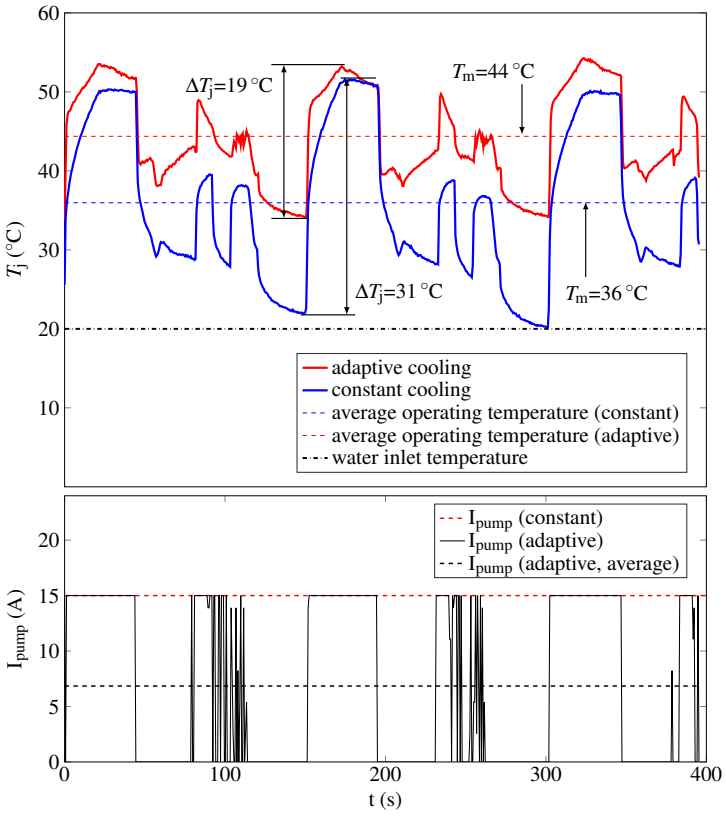

Fig. 5.17. Junction temperature, T_j, results and liquid metal pump supplied current, I_{pump}, with and without thermal controller.

temperature controller is activated, in comparison to the case where maximum constant cooling is applied over the full metro–mission profile. The impact of the MHD time constant, τ_{MHD}, can be seen in Fig. 5.17 when compared with Fig. 5.10. The variation of the thermal resistance R_{th8} for the simulation model is instant, which results in fast changes of the junction temperature. For example, in Fig. 5.10 T_j is the same for both constant and adaptive cooling at the peak point, during the acceleration phase. On the other hand, during the experimental test there is a difference in the junction temperature T_j between the two cooling schemes during acceleration as a result of the time constant τ_{MHD} required by the heat sink to reach its steady state. The largest temperature swing occurs for both adaptive and constant cooling during the acceleration of the metro from a full stop to maximum speed. Over the course of a full metro cycle the adaptive cooling scheme manages to decrease the maximum ΔT_j from 31 to 19 °C, which corresponds to a 12 °C decrease between the two cooling methods. As a consequence, the mean junction temperature is increased by 8 °C, which also contributes to the IGBT lifetime consumption, but as previously mentioned, its impact is not as strong as the temperature fluctuation [**?**]. Also

in Fig. 5.17, the supplied pump current for each case is shown. With the thermal controller activated, the pump current is constantly changing, which affects the flow rate of the liquid metal and therefore, the thermal resistance of the system. Fig. 5.17 shows that the average current required by the adaptive cooling scheme is 50% lower compared to the uncontrolled cooling, which decreases the power consumption of the MHD pump. Thus, the efficiency of the cooling system is also improved with the proposed thermal management scheme.

The proposed thermal control method offers several advantages over other methods found in the literature. It is focused on reducing the temperature swings caused by the mechanical time constant, but at the same time can also reduce the temperature variations caused by environmental changes. Since the feedback from the junction temperature of the device is used for the thermal controller, ΔT_{j} will be decreased irrespectively of the ambient or coolant temperature. Thus, the controller will aim at maintaining the targeted T_{max} even if T_{lm} is varied. Another significant advantage of the presented thermal management scheme is its ability to perform with any arbitrary mission profile, in contrast with thermal controllers that require a predefined one. Finally, except from the liquid metal heat sink, it does not require any auxiliary components. In spite of all the advantages of the proposed thermal controller, its main drawback is the dependence on an accurate online junction temperature measurement method applied [**?**].

Chapter 6

Liquid metal thermal management of press–pack IGBT device

Press–pack is an alternative packaging technology for high–power IGBT modules. In contrast to the conventional power modules, where soldered bond wires are used for the electrical connections, press–pack devices achieve electrical and thermal contact by applying pressure, which is typically from 10 to 20 $\mathrm{N/mm^2}$ [**?**]. The press–pack package was first introduced for monolithic devices containing one silicon wafer in order to improve the reliability for high–power semiconductors, such as diodes, thyristors, and gate turn–off thyristors.

The structure of a PPI device consists of copper lids and molybdenum plates on each side of the silicon dies. Ceramic walls are used to hermetically seal the capsule. Fig. 6.1 shows various internal structures for PPIs, where the pressure distribution system and the molybdenum spacer geometry is the main difference for each design. Molybdenum is ideal as a support material between the lid and the IGBT chip, as it has high mechanical hardness. In addition, it owns a CTE similar to silicone's, therefore, any reliability issues associated with the mismatch of CTE between the materials of conventional power modules are significantly reduced. Combined with the absence of bond wires, the reliability of press–pack devices is significantly improved. Another advantage of press–pack package is the double–sided cooling, which allows for dissipating the

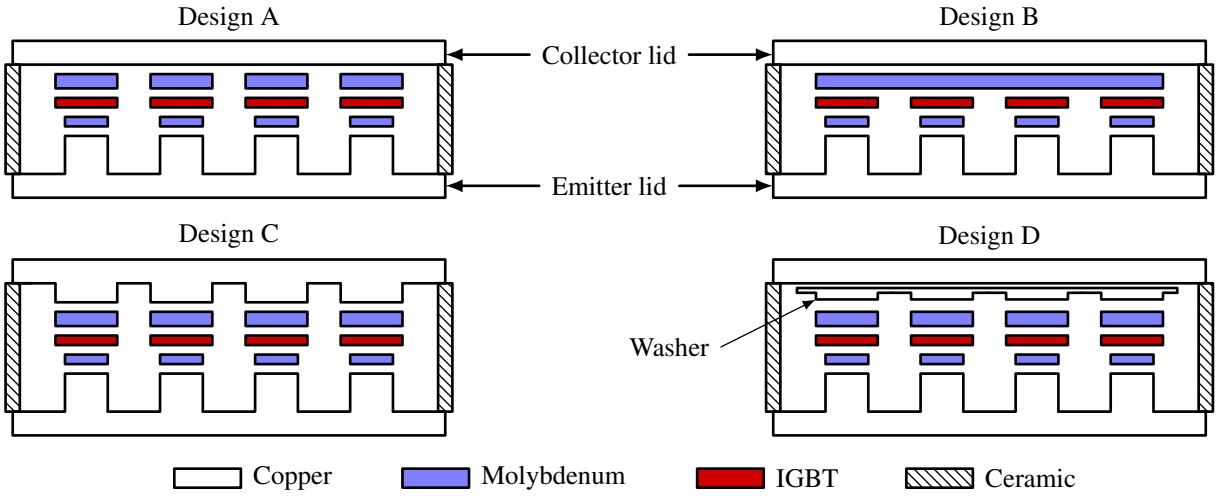

Fig. 6.1. Structure types for press–pack IGBT power modules.

excess heat more effectively. However, their main disadvantage is the absence of electrical insulation.

Unlike conventional IGBT power modules, which behave as an open circuit at their end of lifetime, PPIs feature a short–circuit failure mode. Moreover, they are mechanically compatible to thyristor valves, thus, they can be retrofitted to existing high–voltage systems or be used in new systems in conjunction with existing equipment. Both of these features are particularly important for high–voltage direct current (HVDC) power applications, where multiple press–pack devices are connected in series to attain the required blocking voltage. Fig. 6.2 shows a simplified example of a stack consisting of two PPIs connected in series and cooled by a liquid heat sink on each side. In case that one of the IGBTs fails, it will operate in short–circuit mode, therefore,

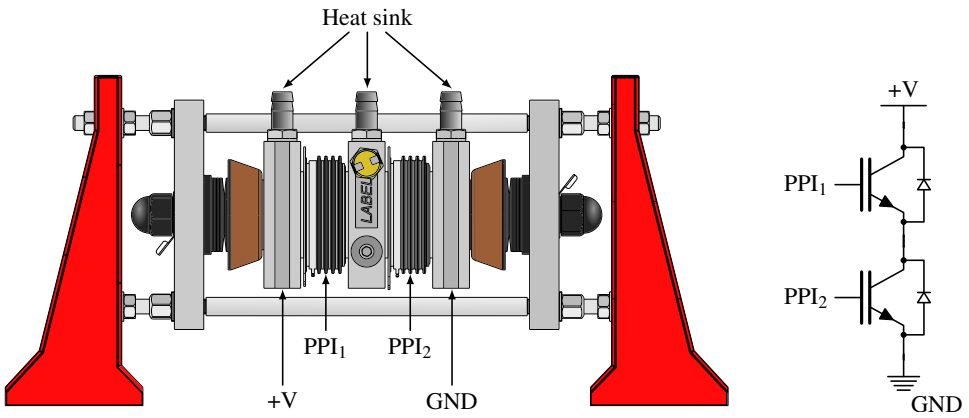

Fig. 6.2. Example electrical schematic for press–pack stack.

allowing the other IGBT to operate normally. Considering that more than 6000 PPIs are used in a modern HVDC station and the cost for unscheduled maintenance is very high [**?**], the short–circuit failure mode is particularly important. The heat management of press–pack devices in HVDC applications is challenging, as an effective cooling method that is able to cope with the high heat loads is required. The most common approach is to use water for dissipating the excess heat. However, since the current should also conduct through the heat sinks, deionised water should be used to avoid short–circuiting the devices. Nonetheless, ionised particles are still developed within the coolant, which could lead to corrosion of the piping system or blockage. Thus, this study focuses on an alternative cooling method for PPIs that can deliver high cooling performance without any of the water cooling shortcomings.

6.1 Design of liquid metal heat sink for PPIs

Traditional cooling for HVDC PPI systems requires deionised water flowing through copper heat sinks that are configured in either typical "S" meander or "Archimedes" spiral structures [**?**]. The heat sink housing is made of copper due to its high electrical and thermal conductivities, which is nickel plated for protection against corrosion. The heat sinks are series or parallel connected and supplied through a liquid pump, as shown in Fig. 6.3. The main disadvantage for series connection is the accumulation of heat from the top modules to the bottom and for parallel connection the need for a large manifold to ensure equal pressure across all the heat

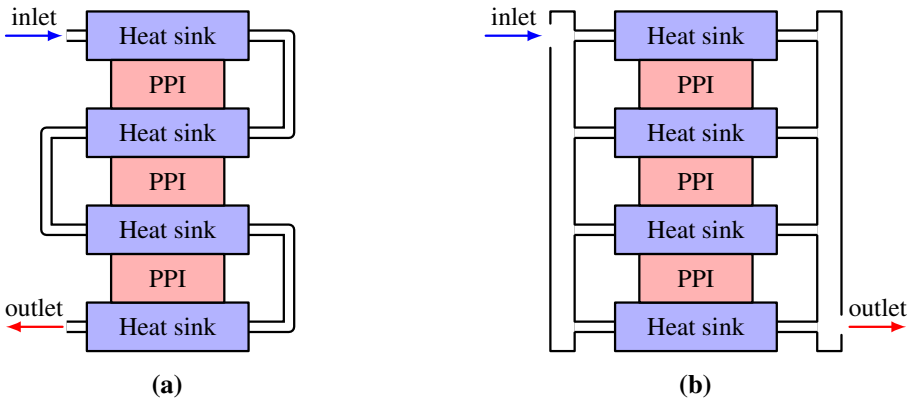

Fig. 6.3. Water–cooled PP stack configurations: (a) series and (b) parallel.

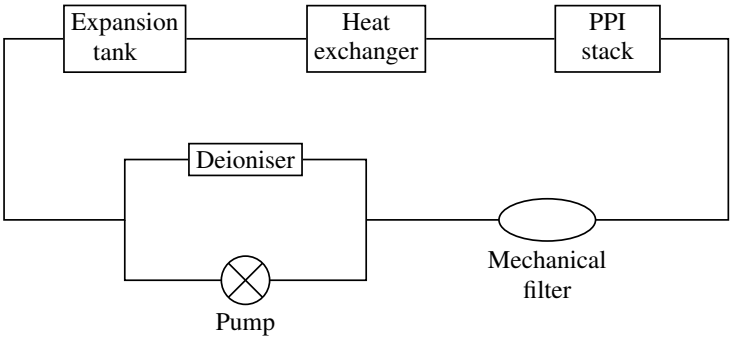

Fig. 6.4. Typical cooling system for HVDC using deionised water.

sinks. Also, Fig. 6.4 shows the schematic of a cooling circuit for HVDC, using deionised water as heat transfer medium. Water is an electrolytic conductor, hence, its chemical composition varies as current conducts through it. More specifically, the free oxygen produced due to the electrolytic activity contributes to the oxidisation process of the cooling system [**?**]. In addition, any electrical potential imbalance between metal components of the cooling circuit, such as the heat sink body and pipe fittings, leads to chemical reactions on the metals. Therefore, in order to reduce the electrolytic currents flowing in the cooling medium, techniques such as limitation of the coolant's electrical conductivity via a chemical filter placed in a bypass parallel to the main circuit, minimisation of the hydraulic diameter of the piping system and placement of grading electrodes at predefined locations, should be employed. In addition, due to deionised water's aggressiveness irrespectively of whether current is flowing through it, the system should be pressurised so as the free oxygen content is limited. Even when plastic tubing, fittings or sealants are used, contact with deionised water could lead to embrittlement and thus, to premature failure. Also, there is a risk of pit corrosion in areas where there is a contact of rubber sealants with metal surfaces [**?**].

This research project focuses on the design and development of a heat dissipation system for HVDC that eliminates the disadvantages of deionised water coolant. Hence, a liquid metal heat sink is proposed that transfers the excess heat generated by the PPIs to a liquid metal–to–water heat exchanger. The geometry of the heat sink was designed considering numerous parameters, such as the geometry of the PPI used for experimental validation, the magnetic field strength in the liquid metal pump active channels and the mechanical rigidity of the heat sink. A pre–assembled commercial PPI stack that consists of a pressure clamp and two PPI devices (Westcode

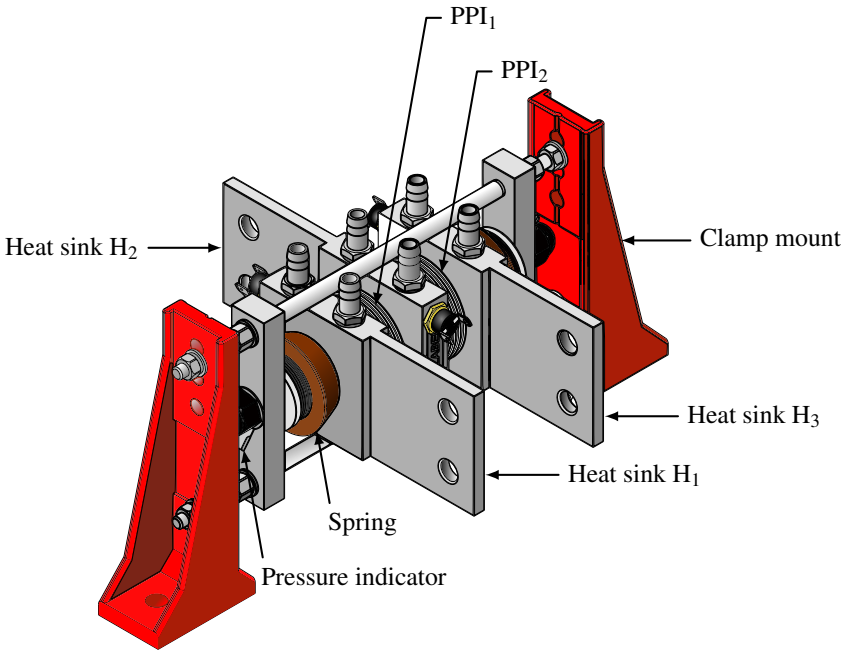

Fig. 6.5. Schematic of press–pack stack.

T0360NB25A), which are double–sided cooled by water heat sinks, is used in this work. The schematic representation of the press–pack stack is illustrated in Fig. 6.5. Two pre–calibrated springs are used to ensure that constant pressure is delivered by the clamp during temperature variations that can potentially cause elastic deformation of the various components. Moreover, mechanical pressure indicators are placed on both sides of the clamping mechanism to ensure that sufficient clamping force is supplied to the press–pack stack.

Detailed schematic diagrams of the PPI and the press–pack stack are presented in Fig. 6.6 and 6.7, respectively. The proposed liquid metal heat sink is designed based on the geometry of the

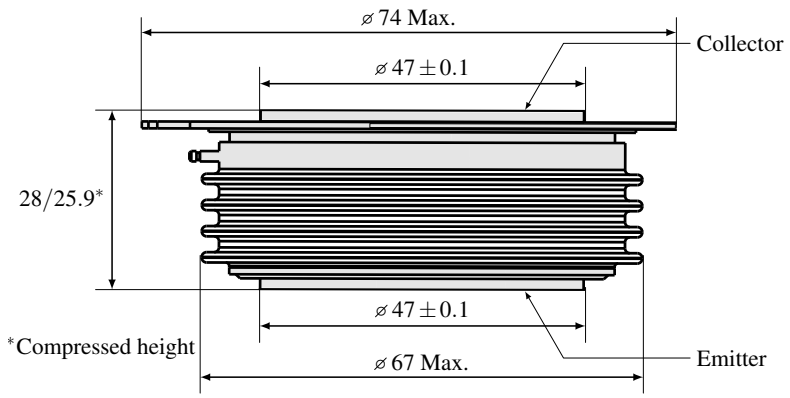

Fig. 6.6. Drawing of Westcode T0360NB25A in mm (W40 package).

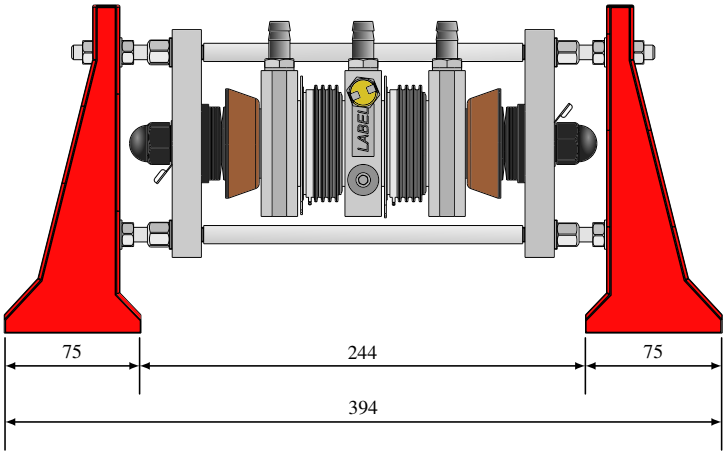

(a)

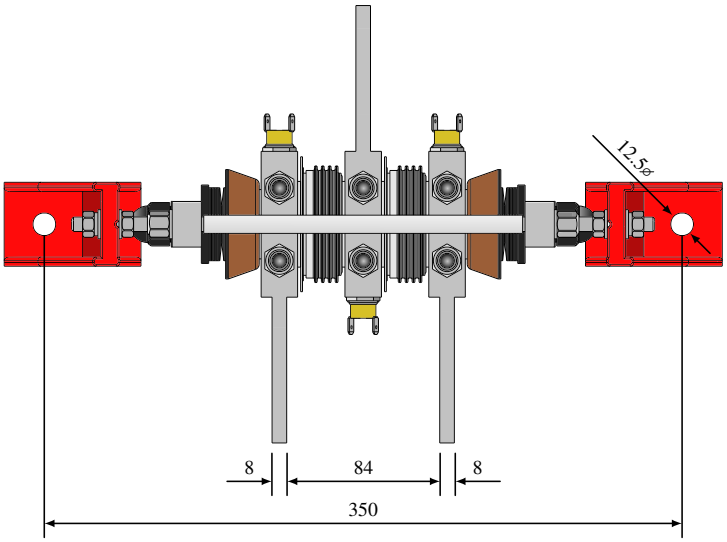

(b)

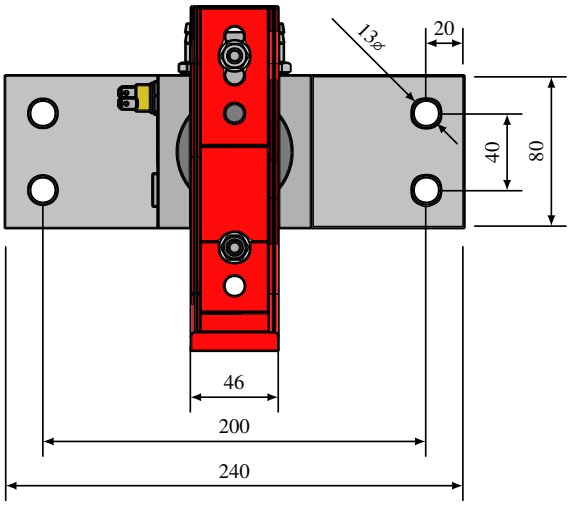

(c)

Fig. 6.7. Press–pack stack dimensions in mm: (a) front view, (b) top view and (c) side view

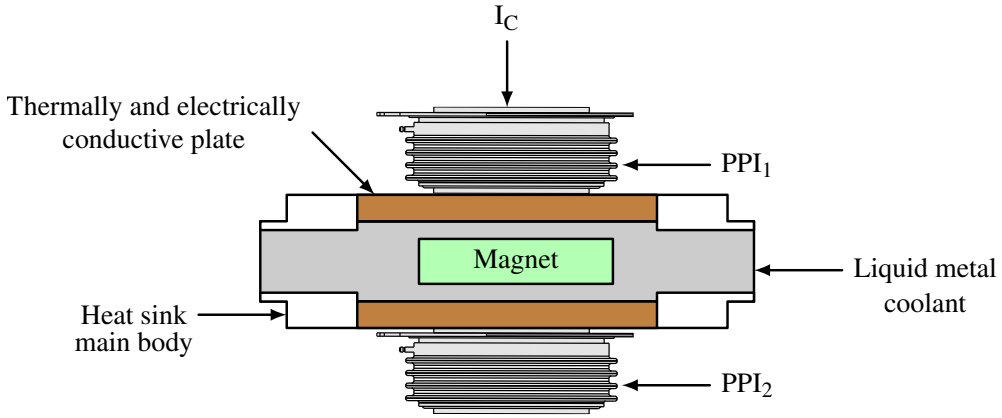

Fig. 6.8. Schematic of proposed heat sink.

stack and the PPI. Dimensions, such as the thickness of the liquid metal heat sink, as well as the surface area of its top and bottom copper plates, are therefore based on the requirements constrained by the stack and PPI geometries.

Fig. 6.8 shows the principle of operation of the proposed heat sink. The collector current, I_C, drives the liquid metal coolant in the presence of a magnetic field provided by permanent magnets. Each side of the heat sink contains a plate that its inner and outer surfaces come in direct contact with the PPI and the liquid metal coolant, respectively. Therefore, the excess heat generated by the PPIs is transferred via the liquid metal. The material selection for the heat sink components are based on their chemical compatibility with $Ga_{68}In_{22}Sn_{10}$. In addition to that, the top and bottom plates of the heat sink should be a good electrical and thermal conductor. On the other hand, the material used for the main body of the heat sink should be an electrical insulator, thus ensuring that I_C conducts solely through the liquid metal.

6.1.1 Mangetostatic simulation of liquid metal pump

Infolytica MagNet was used to perform various magnetostatic simulations for the design of the liquid metal heat sink, which are presented in this section. Firstly, a magnetostatic simulation is performed for various pump geometries, where 50 A conducting current and N42 Neodymium magnets are used for all simulation models. The results are shown in Fig. 6.9. Design A has a large liquid metal channel covering the whole copper lid area and the magnetic field is provided

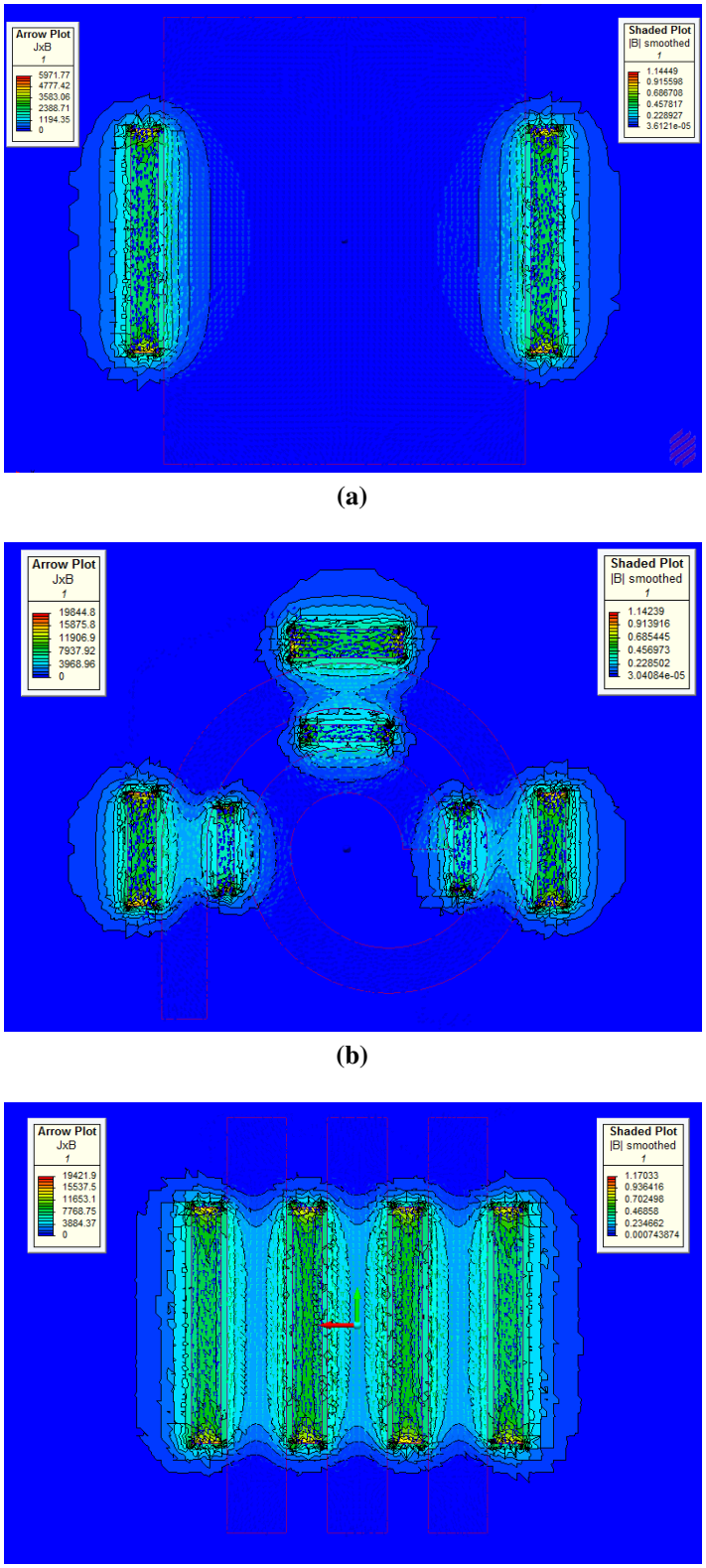

Fig. 6.9. Magnetostatic simulation results for various pump geometries: (a) design A – single channel, (b) design B – spiral and (c) design C – parallel channel.

by two magnets placed on each side of the channel. This design is not suitable, as the distance between the two magnets is large and therefore, there is no uniform magnetic field cutting through the conductive coolant. As shown, a Lorentz force is generated only at the sides of the liquid metal channel, thus, there is no fluid flow at the center of the channel.

On the other hand, design B shows a spiral structure for the liquid metal, where three sets of magnets are placed for generating the liquid metal flow. Although a large heat transfer area is achieved with the spiral design, the magnets size and position are limited, which impacts the net Lorentz force. Moreover, the implementation of such design is challenging compared to the other two candidates.

Finally, design C proposes a heat sink consisting of parallel channels. A magnetic field is provided through permanent magnets at each channel. The advantage of design C is that the length of the magnets is not restricted by the channel geometry. Hence, long magnets that are able to cover the majority of the current path can be used. In addition, the channel length (i.e. the distance between the magnets) can be altered, so as sufficient magnetic field strength is provided for the pump. As shown, the largest Lorentz force is generated with design C. Therefore, a heat sink that features parallel channels is selected for this work.

The relationship between the channel length, the magnetic field strength and the heat transfer area is also studied numerically. The geometry of the permanent magnets is maintained constant at $40 \times 10 \times 5\,\text{mm}$, which is the same size as the magnets used in the experimental work. Similarly, the total heat sink area is restricted to $70 \times 70\,\text{mm}$ due to the stack and PPI geometries. Therefore, the heat transfer area of the cooling device and the magnetic field in the midplane of the channel is a function of the channel distance. The results are shown in Fig. 6.10. For a distance less than 10 mm there is a strong magnetic field, however the heat transfer area is not large, whereas, for a distance larger than 14 mm the magnetic field is not sufficient to pump the liquid metal and the effective heat transfer area is reduced, as the number of parallel channels is decreased. A channel distance of 14 mm is selected in this work, as it provides the largest heat transfer area without compromising the liquid metal pump performance.

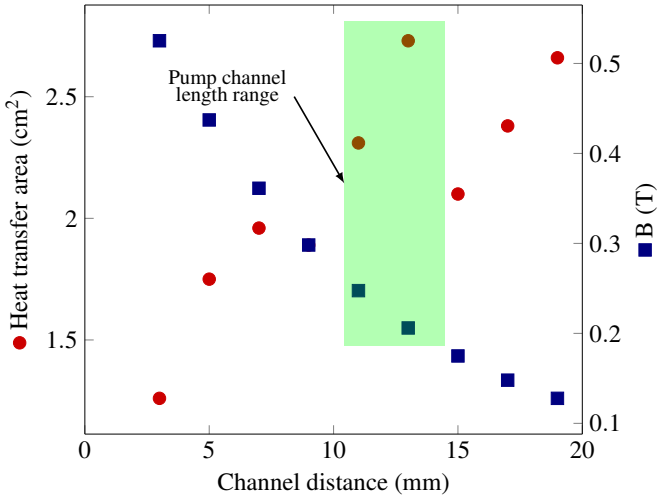

Fig. 6.10. Magnetostatic analysis of the channel distance in relationship with the magnetic field strength and heat transfer area.

6.1.2 Design parameters of liquid metal heat sink

Fig. 6.11 illustrates a detailed view of the cooling system for one side of the PPI. As shown, the collector and emitter lids of each PPI come in direct contact with the copper plates of the heat sink, which forms a closed loop with a heat exchanger. The system is filled with the liquid metal $Ga_{68}In_{22}Sn_{10}$ and the excess heat is transferred from the copper plates to the heat exchanger, where it is then dissipated to the ambient through water cold plates that are attached to the heat

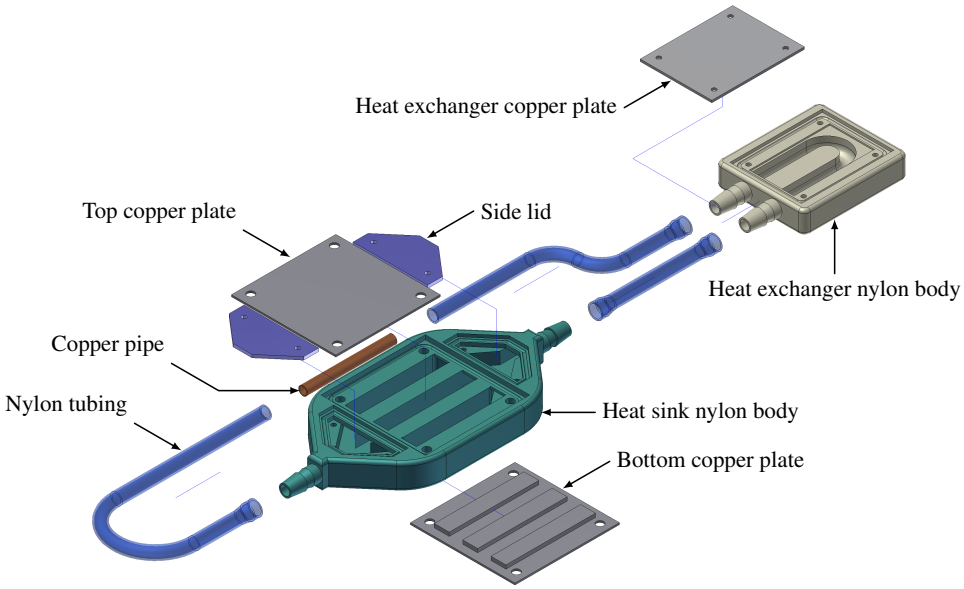

Fig. 6.11. Exploded view of press-pack heat sink.

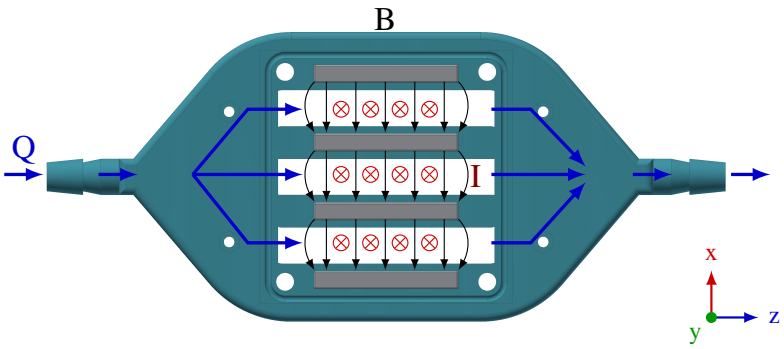

Fig. 6.12. Working principle of liquid metal heat sink for press–pack devices.

exchanger copper surface. An intermediate layer made of ceramic aluminium oxide is applied between the heat exchanger and the water cold plate, which provides electrical isolation between the two surfaces while allowing the heat to travel. The drawings of the liquid metal–to–water heat exchanger, the liquid metal heat sink and their copper lids are presented in Appendix C. Fig. 6.12 shows the operating principle of the liquid metal pump. As the body of the heat sink is made of nylon, the collector current I_C conducts only through the liquid metal in y plane, which in combination with the constant magnetic field in x plane generates a Lorentz force in z plane that drives the liquid metal. Therefore, the liquid metal pump is self–driven, as no external power is required.

The material selection for the cooling system was performed based on the project requirements. The bodies of the heat sink and heat exchanger are 3–D printed using VeroWhite, which is chemically compatible with $Ga_{68}In_{22}Sn_{10}$. Also, VeroWhite is an electrical insulator. The design of the 3–D printing was performed by the author, whereas the printing was executed at one of Newcastle University's printers that is able to print at high resolution. In order to connect the heat sink to the heat exchanger, chemically resistant flexible plastic tubing is used. Although copper forms a thin oxidation layer when it is in direct contact with $Ga_{68}In_{22}Sn_{10}$, its mechanical

Table 6.1. Physical parameters of copper and nickel.

Parameter	Unit	Copper	Nickel
Electrical conductivity	S/m	$5.96 \cdot 10^7$	$1.43 \cdot 10^7$
Thermal conductivity	$W/(m \cdot K)$	385	90
Relative permeability	—	0.999 994	100–600

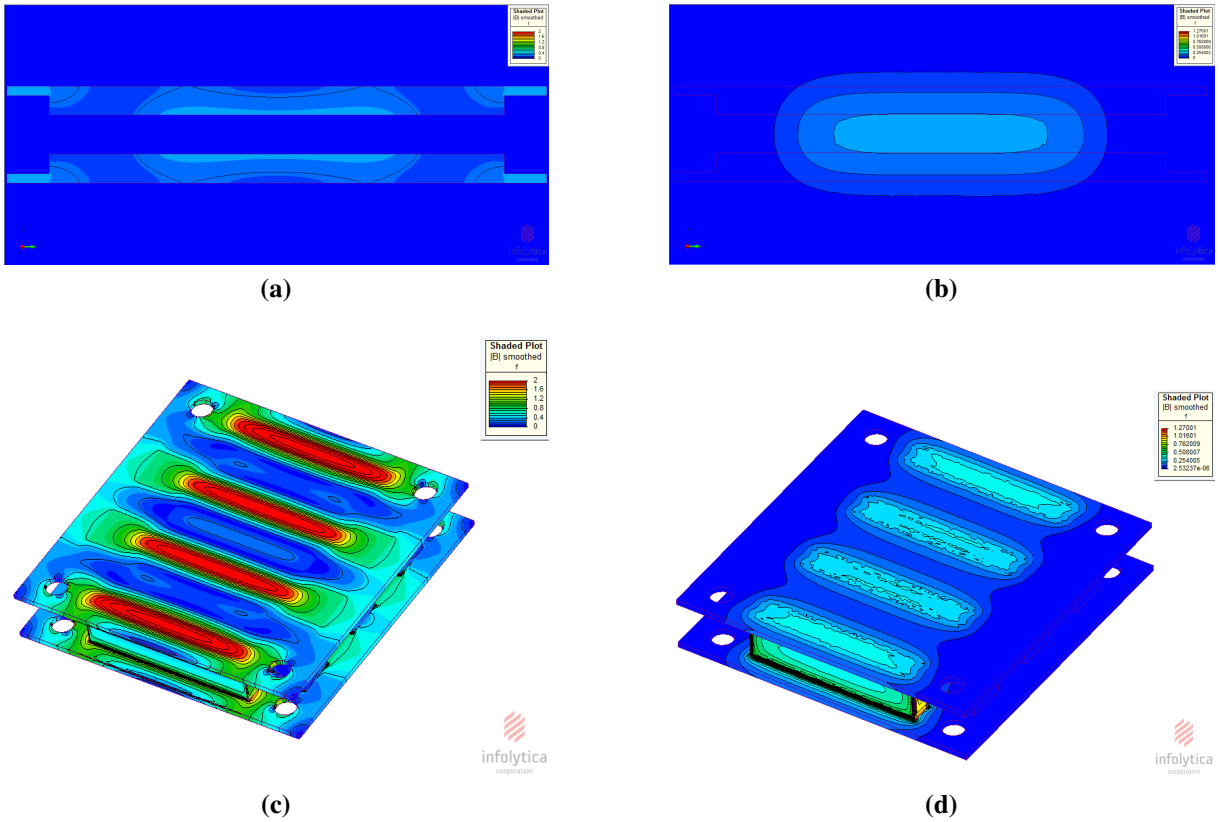

Fig. 6.13. Simulation results of magnetic field in the liquid metal pump: magnetic field contour in the active channel of the pump for (a) nickel plate (b) and copper plate. Magnetic leakage for (c) nickel plate and (d) copper plate.

rigidity and long–term reliability are not compromised. Nonetheless, applying a thin nickel layer ensures protection against corrosion. Alternatively, pure nickel was considered for the lids, as it does not corrode against $Ga_{68}In_{22}Sn_{10}$. However, as shown in Table 6.1, copper has significantly superior thermal and electrical properties. In addition, nickel has very high relative magnetic permeability (μ/μ_0), thus affecting the magnetic field in the active channel of the pump. The effect of copper and nickel lids on the magnetic field was investigated numerically. As observed from Fig. 6.13, there is a uniform magnetic field of 0.2 T by using copper plates, whereas the use of nickel results in a magnetic field of 0 T, since there is a large magnetic flux leakage caused by the nickel plates. In the simulation model the best case scenario of $\mu/\mu_0 = 100$ was selected for nickel. Another disadvantage of nickel compared to copper is its higher cost.

6.1.3 Static structural analysis of the heat sink

The cooling system is constantly subjected to a high clamping force, therefore, a static structural analysis was performed in ANSYS Mechanical to evaluate the stress and strain magnitude within the heat sink structure and to determine whether a plastic strain will occur in the event of excessive pressure being applied. A maximum force of 10 kN is applied at the top copper lid, whereas the bottom copper lid is configured as a fixed support. Moreover, all the contact connections between different bodies were configured as rough. As the results in Fig. 6.14 show, the maximum strain is observed at the edges of the heat sink body, however, it is only a few µm. Also, no plastic strain is observed, which could lead to failure of the cooling system. However, during the experimental testing the glass transition temperature, T_g, of VeroWhite should not be exceeded, as its physical properties are altered at that point.

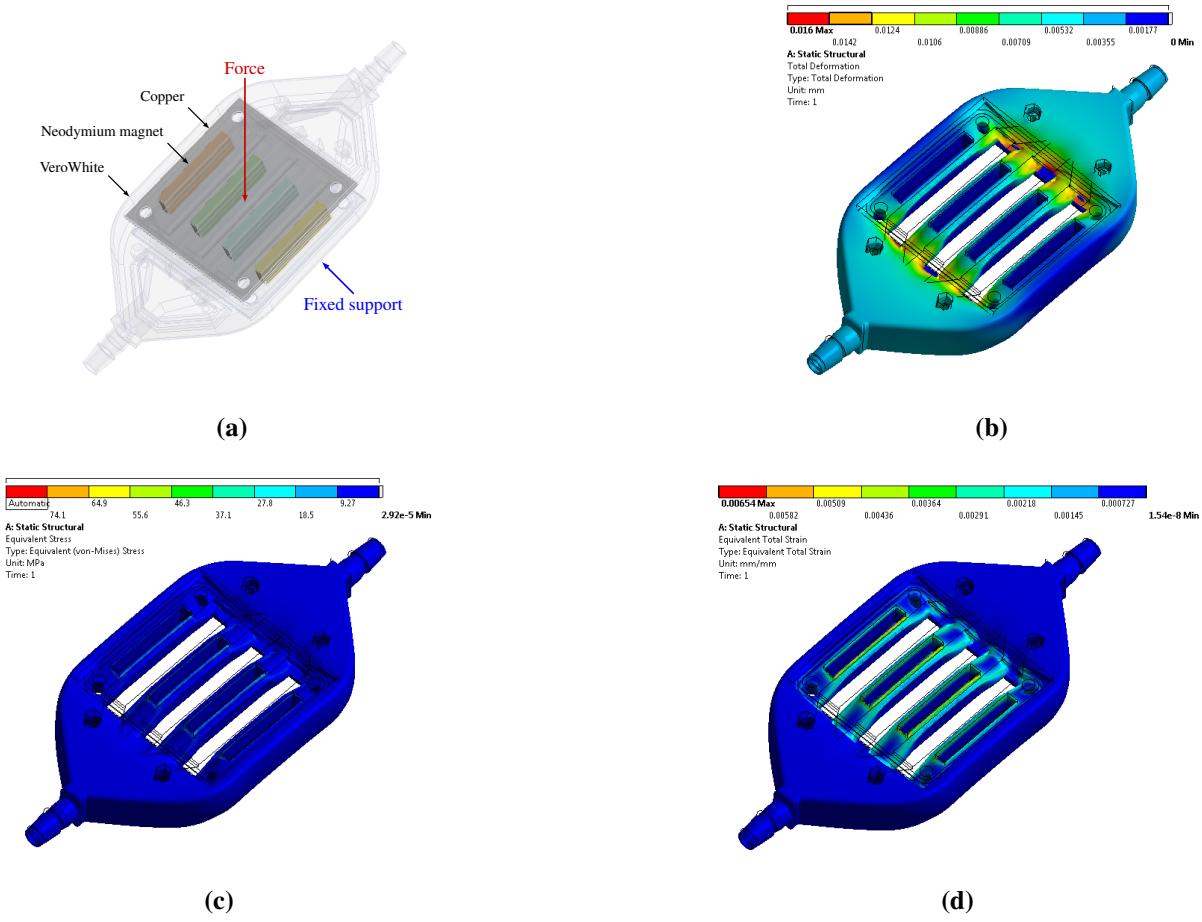

Fig. 6.14. Simulation results of static structural analysis for the heat sink: (a) simulation model (b) total deformation (c) equivalent stress and (d) equivalent strain.

6.2 Experimental setup for press–pack heat sink evaluation

The steady state heat transfer capability of the liquid metal heat sink is experimentally evaluated through a series of tests, in which the water heat sinks H_2 and H_3 are replaced by the proposed heat sinks. The heat load of the system is generated by the self–heating of the PPI devices due to the power losses, P(t). The schematic diagram of the circuit used for heating the PPI device and sensing the junction temperature, T_j, is shown in Fig. 6.15. Devices PPI_1 and PPI_2 are press–pack devices mounted on the same stack, as illustrated in Fig. 6.5. The TopCon Quadro programmable power supply unit provides a constant DC current, I_{heat}, for heating the DUT, whereas, I_{sense} provides a small current for temperature sensing. Diodes D_1 and D_2 are placed in order to force I_{sense} and I_{heat} to flow through PPI_2, which is the DUT. The IGBT switch S_1 serves as auxillary switch and provides a path to I_{heat} whenever PPI_1 is switched off.

The current waveforms for heating the IGBT and T_j sensing is shown in Fig. 6.16. The DUT remains in its forward conducting state for the whole thermal characterisation process, by applying +15 V across the gate and emitter. During the heating phase, S_1 is switched off while PPI_1 is conducting, thus allowing I_{heat} to also conduct through PPI_2, which drives the coolant as well. On the other hand, during the temperature measurement process S_1 conducts while PPI_1 is switched off. At that instance only I_{sense} is conducting through PPI_2, therefore, the TSEP is applied. The DUT is heated for 98.5 ms, whereas, the temperature measurement process lasts for 1.5 ms. There is an overlap of a few µs, during which both S_1 and PPI_2 are conducting simultaneously, in order to prevent the I_{heat} power supply switching to constant voltage mode.

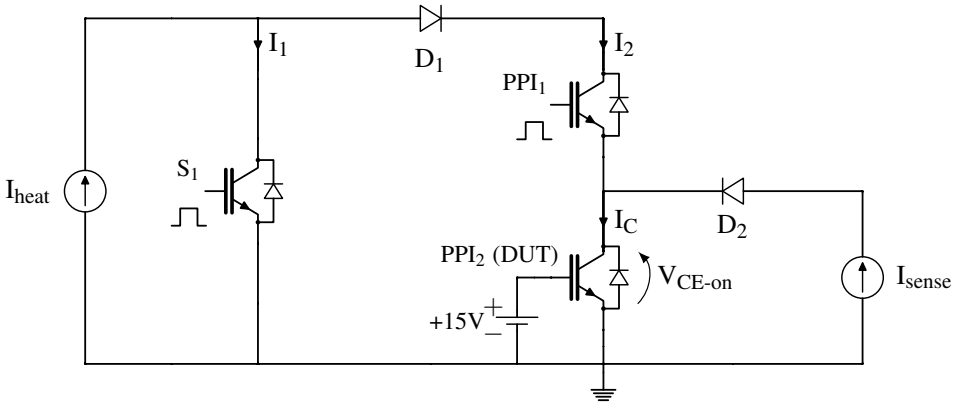

Fig. 6.15. Schematic diagram of PPI heating and temperature sensing.

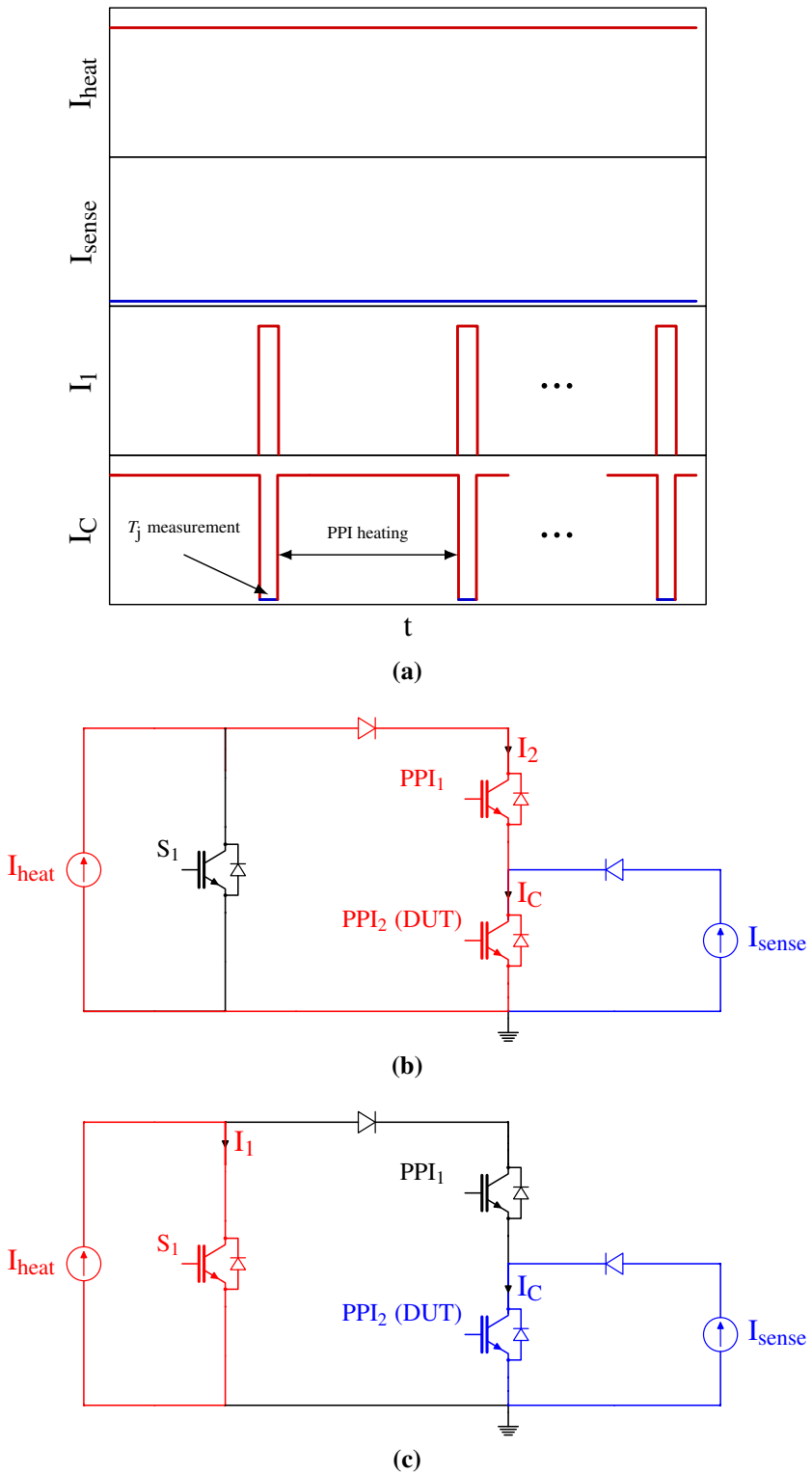

Fig. 6.16. PPI heating and temperature measurement: (a) example waveform for PPI heating and junction temperature measurement, (b) heating phase and (c) temperature measurement phase.

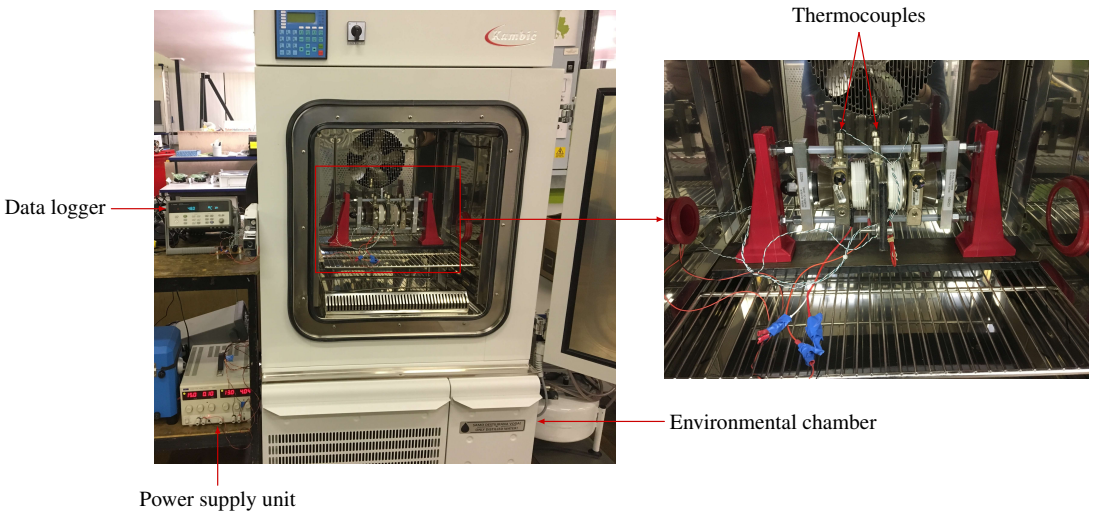

Fig. 6.17. TSEP calibration test setup.

Similarly to the work conducted in Chapter 4, the dependency of $V_{CE\text{-}on}$ on T_j for a low conducting current was selected for sensing the junction temperature of the PPI. Unlike the IGBT devices that are housed in a conventional pagkage, press–pack devices require a pressing force that ensures electrical and thermal contact. Therefore, the calibration of the TSEP cannot be performed using a temperature controlled plate (presented in p. 62), as the device should be pressed and heated concurrently. Instead, an environmental chamber was used, where the press–pack stack is heated uniformly. The DUT is constantly in its forward conducting state and I_{sense} conducts through it for the whole duration of the calibration. The temperature of various locations was monitored with thermocouples that were mounted on the heat sink bodies and inside the hollow heat sink pipes. The TSEP calibration setup is shown in Fig. 6.17. Each $V_{CE\text{-}on}$ reading is taken once the DUT is in thermal equilibrium (i.e. once all thermocouples sense the same temperature). The $V_{CE\text{-}on}$ is recorded for I_{sense} between 20–100 mA in 10 mA intervals. The results of the TSEP calibration process are presented in Fig. 6.18. The value of 20 mA was selected as sense current for temperature measurement of the PPI device, as it provides the highest resolution ($-2.5\,\mathrm{mV/^{\circ}C}$). In addition, the R^2 value of the graph approaches 1, thus indicating a very good linear regression of the curve. Hence, for a constant sense current of 20 mA and a given $V_{CE\text{-}on}$, the junction temperature, T_j, is defined as:

$$T_j = 221.47 - 400 \cdot V_{CE\text{-}on} \tag{6.1}$$

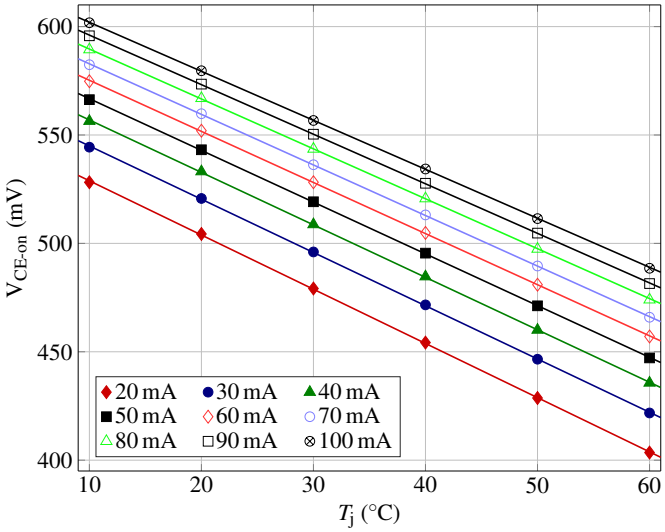

Fig. 6.18. TSEP calibration curves of PPI for various sense currents.

6.3 Experimental testing of liquid metal heat sink

The heat dissipation performance of the liquid metal heat sink is evaluated through a steady state heat transfer experimental test and is compared against a conventional water–based commercial heat sink for PPIs. The schematics of the cooling circuits for water and liquid metal heat sinks are presented in Fig. 6.19 (a) and (b), respectively. In both tests, a flow meter (Q_w), pressure

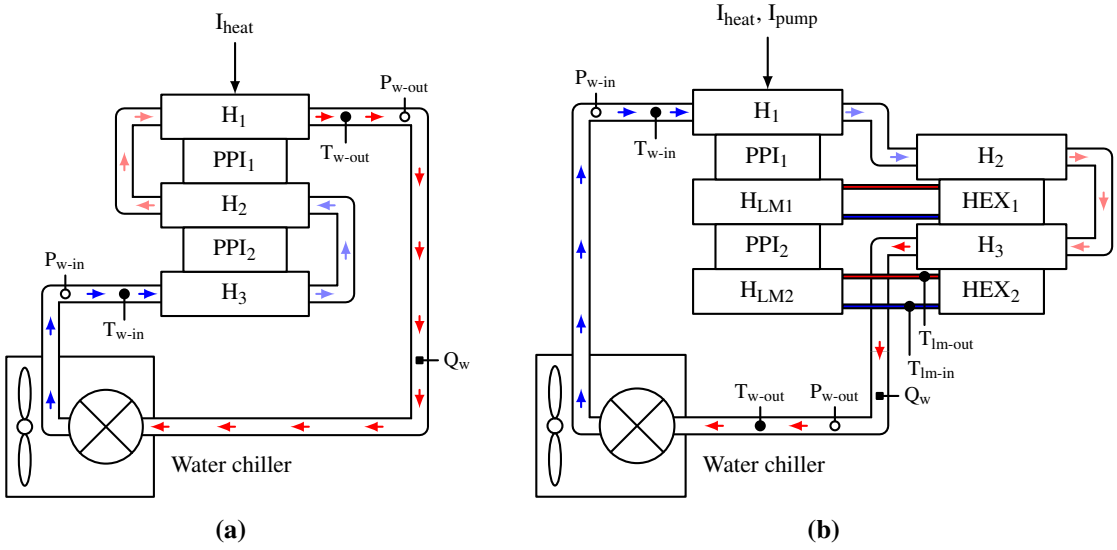

Fig. 6.19. Schematic diagram of press–pack cooling circuit: (a) water cooling system and (b) liquid metal cooling system with liquid metal–to–water heat exchangers.

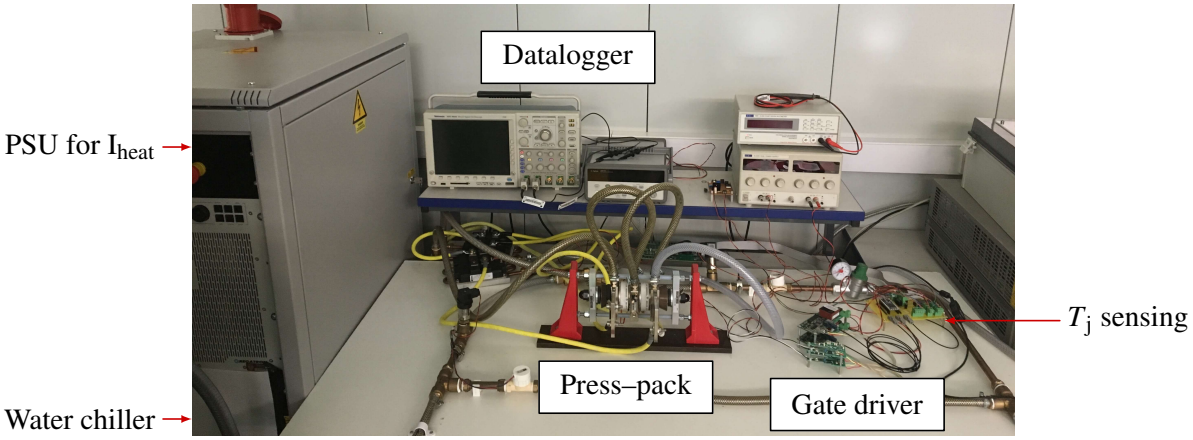

(a)

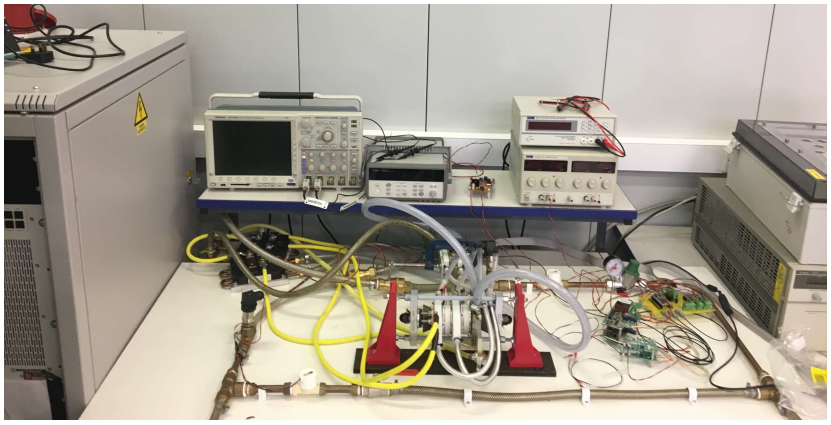

(b)

Fig. 6.20. Experimental test setup for press–pack cooling testing: (a) water cooling system and (b) liquid metal cooling system with liquid metal–to–water heat exchangers.

transducers ($P_{w\text{-}in}$ and $P_{w\text{-}out}$), and thermocouples ($T_{w\text{-}in}$ and $T_{w\text{-}out}$) are used for monitoring the water flow rate, the pressure drop across the water cooling loop and the inlet and outlet temperatures of water. Additional thermocouples ($T_{lm\text{-}in}$ and $T_{lm\text{-}out}$) are placed for monitoring the inlet and outlet temperature of the liquid metal loop. Fig. 6.20 shows pictures of the experimental test setups for water and liquid metal cooling. Additional pictures of the liquid metal cooling system are presented in Appendix C.

The results of the thermal characterisation for both water and liquid metal cooling schemes are shown in Fig. 6.21. The two cooling methods were subjected to a heating current, I_{heat}, ranging from 50 to 200 A, which corresponds to heat loads between 60 and 384 W. In addition, the flow rate of the water cooling circuit was varied throughout the experimental process. Each

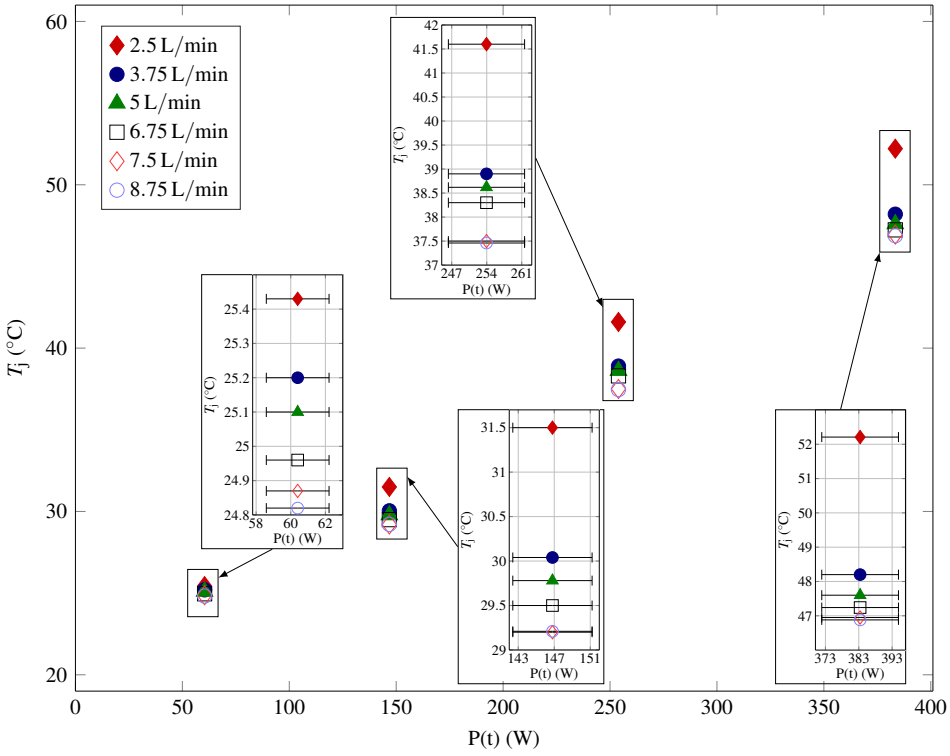

(a)

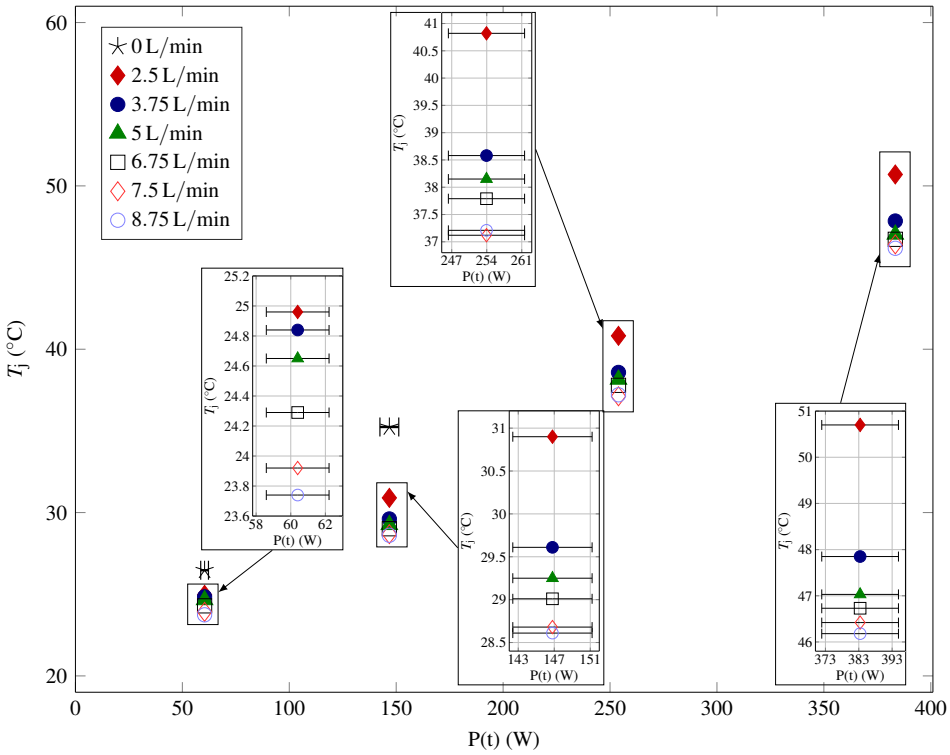

(b)

Fig. 6.21. Experimental results for press–pack cooling system under various heat loads and flow rates: (a) water and (b) liquid metal

measurement is performed after the DUT has been heated for 30 minutes, whereas the water inlet temperature is fixed at 20 °C . As observed, the cooling effectiveness of both cooling systems is reduced as the coolant's flow rate decreases. A special case where the water cooling system is shut off and thus emulates a water pump failure is also tested and presented in Fig. 6.21. For that part of the experiment, the water chiller is switched off, resulting in a net water flow rate of $0\,\mathrm{L/min}$. Therefore, the heat is transported through the liquid metal to the heat exchanger and then is dissipated to the ambient via the copper bodies of the water heat sinks.

The assessment of uncertainty was performed in accordance to the methodology presented by Moffat [**?**] and the work of Coleman and Steele [**?**], in which the overall uncertainty (u_t) is dependent on two error indexes; the systematic and random errors. In (6.2) the overall uncertainty, u_t, is described.

$$u_t = 2\sqrt{\left(\frac{B_u}{2}\right)^2 + \left(\frac{\sigma_d}{\sqrt{x}}\right)^2} \tag{6.2}$$

In (6.2) B_u is the systematic uncertainty, σ_d is the standard deviation of the results and x is the number of samples for each measurement point. In this work, once steady state is reached, one sample per second has been recorded for a total duration of 5 minutes. Thus, the overall uncertainty for power measurements, based on the measuring equipment used for this experiment, is $\pm$ 3%, for the current is $\pm$ 1%, for the thermal resistance is $\pm$ 3% and for the water flow rate is $\pm$ 5%. The uncertainty for temperature measurements; both via thermocouples and the TSEP was negligible, as a temperature calibration was performed for all the temperature sensing devices before the experimental procedure.

The repeatability tests demonstrate a 95% data reproduction. Therefore, the uncertainty analysis ensures that 19 out of 20 repeated trials should yield the same results within the error spectrum in the case where the same apparatus and techniques are used, however, without using the same instruments.

The thermal resistance of the cooling system for various flow rates is derived from the experimental data presented in Fig. 6.21 and is shown in Fig. 6.22. As demonstrated, the proposed liquid metal cooling system provides lower thermal resistance for identical water flow rates. Thus, higher heat loads can be potentially rejected without the risk of thermal runaway, although

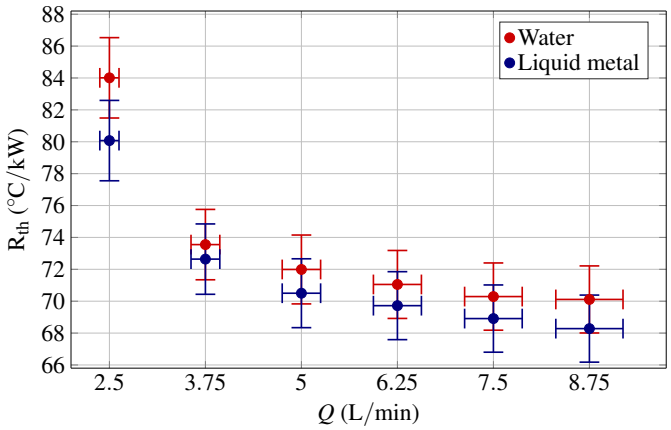

Fig. 6.22. Thermal resistance of cooling systems as a function of the water flow rate.

the difference between the two cooling methods in not large. Moreover, based on the uncertainty analysis, the error bars in Fig. 6.22 indicate that the difference in the thermal resistance of the two heat sinks is not significant, as their error ranges intersect. In spite of all the advantages that the proposed method offers, such as higher cooling capability and electrically isolated cooling mechanisms that eliminate the problem associated with corrosion in HVDC systems, no moving parts and external power source, each liquid metal heat sink acts as a series resistance between the PPIs. Hence, as presented in Fig. 6.23, each liquid metal pump generates additional heat loss that needs to be dissipated by the cooling mechanism. The water cooling system consumes an additional 10–40 W for a flow rate range between 2.5–8.75 L/min. Nonetheless, these figures only consider the power across the three water heat sinks and do not take into account the full power required by the chiller, which includes the water pump efficiency and the additional fan

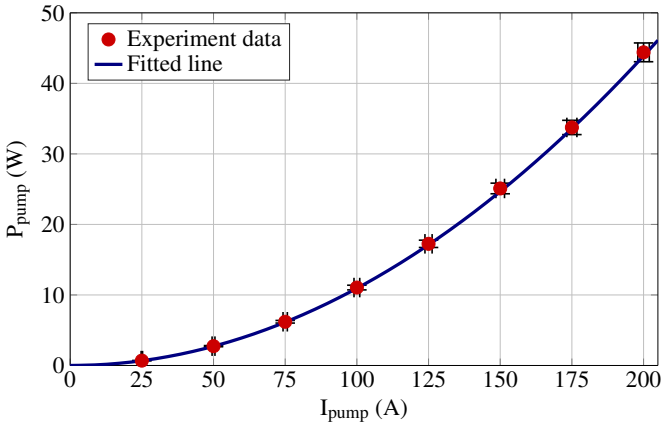

Fig. 6.23. Consumed power of liquid metal pump as a function of the input current.

required for the radiator. Moreover, there is a voltage drop across each heat sink that should be taken into consideration for HVDC applications, which involve high currents and require multiple PPIs connected in series. To overcome this limitation, a current path that is parallel to the pump can be placed to limit the current conducting though the liquid metal. This will in turn have an effect on the liquid metal flow, however, as demonstrated in Chapter 4, the heat extraction capability of the liquid metal cooling loop is saturated at flow rates lower than the ones generated by the conducting current. On the other hand, the heat sink housing could be electrically conductive thus allowing the current to pass through it, in a similar configuration to the traditional water–cooled heat sink. Consequently, the MHD pump should be placed externally and driven by a secondary isolated power supply source, without the cooling system contributing to the voltage drop of the PPI stack. Finally, the proposed scheme is only applicable for PPIs that do not feature an anti–parallel diode. As the direction of the magnetic field is fixed, inverting the conducting current would reverse the liquid metal flow, thus resulting in oscillating movement of the coolant.

Lastly, the junction temperature of the DUT is measured for various switching frequencies, f_s, to test the effect of the switching current on the liquid metal heat sink. Similarly to the previous experiment, the DUT remains in its forward conducting state, however, PPI_1 and S_1 operate at a predefined switching frequency. As the results of Fig. 6.24 show, the junction temperature, T_j, is constant irrespectively of the switching frequency. The junction temperature increases slightly

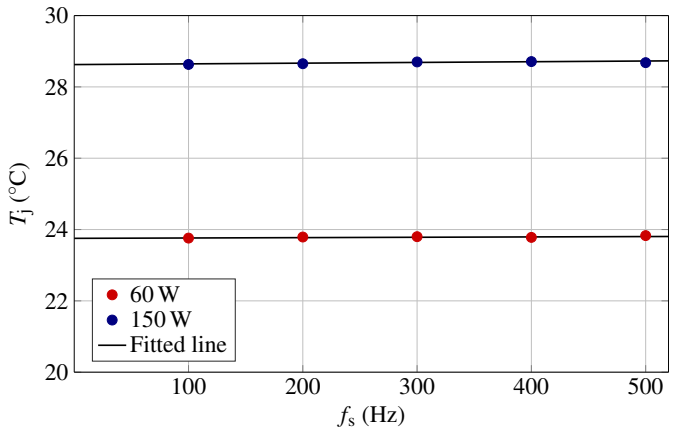

Fig. 6.24. Dependence of the cooling system on the switching frequency.

as the switching frequency is increased but it could be due to the additional heat losses generated by the switching action of PPI_1.

Chapter 7

Conclusions

Power electronic devices are essential components for energy conversion in modern power systems. They are often employed in safety–critical applications, hostile environments or in spatial restricted applications. As the long–term reliability and lifetime expectancy of the power electronics are associated with the operating junction temperature and the junction temperature fluctuations of the device, there's a need for high–performance, reliable, compact and lightweight thermal management systems.

In this thesis, the adoption of a room–temperature liquid metal as heat transfer agent has been investigated for two types of IGBT devices; conventional and PPI power modules. The superior thermophysical properties of liquid metals compared to water contribute to the development of heat management devices that offer higher cooling capability, higher reliability, and lower weight, which are desirable characteristics for modern power electronic applications.

Unlike conventional coolants, such as water, which require a mechanical pump to drive the fluid, an MHD pump can be used for driving liquid metals due to their high electrical conductivity. Therefore, this thesis has presented the design, development and fabrication of two MHD pumps, which are integrated in the cooling loop.

7.1 Liquid metal heat sink for conventional power modules

An integrated liquid metal heat sink has been designed, developed and tested for conventional power modules. The heat sink is attached to the bottom of the power module and the coolant is impinging against the baseplate, thus having a direct interface between the coolant and the power module. The liquid metal jet is directed toward the IGBT chip position, so as to achieve local cooling. The prototype heat sink body is made of VeroWhite engineering plastic. An MHD pump is used for driving the coolant and is integrated in the heat sink body. The simulation and experimental results show that the liquid metal heat sink can achieve lower junction temperature of the IGBT device under identical heat loads.

The liquid metal heat sink is also utilised for adaptive thermal management of the IGBT power module. Based on lifetime models, the amplitude of junction temperature swing is the dominant factor for the lifetime consumption of the device due to the thermomechanical stress imposed between the layers of the device during temperature fluctuations. The aim of the adaptive temperature control is to reduce the temperature fluctuations, which depend on the mission profile of the device or on environmental alternations. To achieve that, the liquid metal flow rate is controlled based on the junction temperature of the device, which is sensed based on an implemented TSEP. Compared to the adaptive thermal management techniques found in the literature, this method does not introduce additional heat loads to the system, does not require auxiliary power switches or knowledge of the mission profile.

7.2 Liquid metal heat sink for PPI power modules

PPI modules have significant advantages over conventional modules, such as the ability to apply double–side cooling and higher tolerance against large temperature fluctuations because of its internal structure. Nonetheless, their use in HVDC power stations in combination to a water–based cooling system leads to overcomplicated cooling networks. Moreover, there is a risk of failure of the cooling system due to piping corrosion as a product of the interaction between the conducting current and the coolant.

Similarly to the work presented for conventional power modules, a heat sink based on a liquid metal agent is proposed for PPI devices. Heat is transported from the PPI device via convection to the liquid metal coolant, which is driven by an integrated MHD pump, to a liquid metal–to–water heat exchanger. Each liquid metal cooling loop is electrically isolated to their adjacent loops, therefore, the same water loop can be used without risking current conducting through water and thus leading to the development of corrosion in the water piping system. In addition, the load current conducting through PPIs is used for driving the liquid metal, hence, the liquid metal cooling system is self–driven and does not depend on an external power source. Experimental comparisons between the liquid metal–based cooling system and a commercial water–based cooling system have demonstrated a junction temperature reduction under identical working conditions by employing the proposed cooling scheme.

7.3 Future work

Based on the work presented in this thesis, there is potential for further development of the proposed cooling methods. The liquid metal heat sink for conventional power modules has been tested on a single IGBT chip, however, for the scheme to be applicable in a real application, an online method is required for sensing the junction temperature. In addition, the cooling loop should be modified, so as it cools all the IGBT and diode chips of the power conversion system. Similarly, the heat sink for PPIs should use an external MHD pump that is fed by an isolated DC power source if the power module features antiparallel diode chips, to avoid an oscillating movement of the liquid metal coolant. Moreover, a current path parallel to the heat sink should be employed for high current applications, such as HVDC, to limit the losses of the MHD pump. Both of the proposed heat sinks have been fabricated using 3–D printed engineering plastic, however, considering the long term reliability of the cooling system a material that can withstand high temperatures and is chemically resistant to liquid metals should be used instead.

Appendix A

Types of fluid flow

Fluid flows are classified into three types; laminar, transient, or transitional. Fig. A.1 shows the velocity profile for each flow regime.

Laminar flow, also known as streamline flow, is characterised by fluid flowing in parallel layers. As a result, neighbouring layers are not interfering. It is mainly found in small pipe diameters at low fluid velocities. The velocity is maximum at the mid–plane and approaches zero at the pipe walls under the no–slip condition. The flow parameters, including the velocity and pressure, remain constant at each point of the fluid.

Turbulent flow is described by chaotic variations in the velocity or pressure of the fluid. It occurs in regions of the fluid flow, where the damping effect of the viscosity is surpassed by kinetic energy. Turbulence is the most common fluid flow; spanning from natural phenomena, such as ocean currents and wind, to engineering applications, such as oil transport in pipelines.

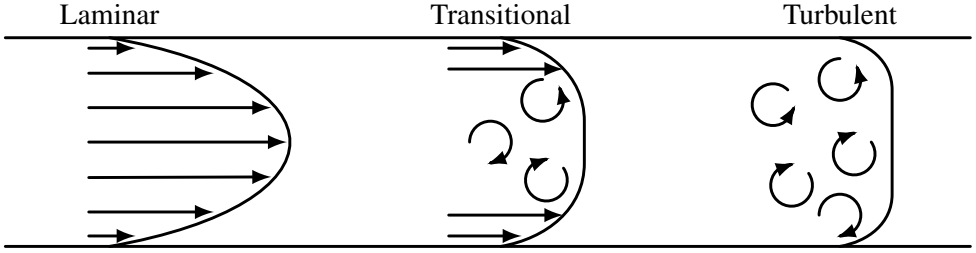

Fig. A.1. Types of fluid flow in a pipe.

Finally, transitional flow is a mixture of the two types mentioned above. It is characterised by turbulence in the center of the pipe and laminar flow towards the pipe walls. The flow regime is defined by the Reynolds number, as follows:

- $Re < 2300$ for laminar flow.
- $2300 < Re < 4000$ for transitional flow.
- $Re > 4000$ for turbulent flow.

Appendix B

CFD supplementary data for conventional IGBT module heat sink

Simulation problem and results

Fig. B.1 shows the simulation model of the liquid metal heat sink. The inlet and outlet of the fluid domain are perpendicular to the baseplate of the IGBT module. Only half the module is

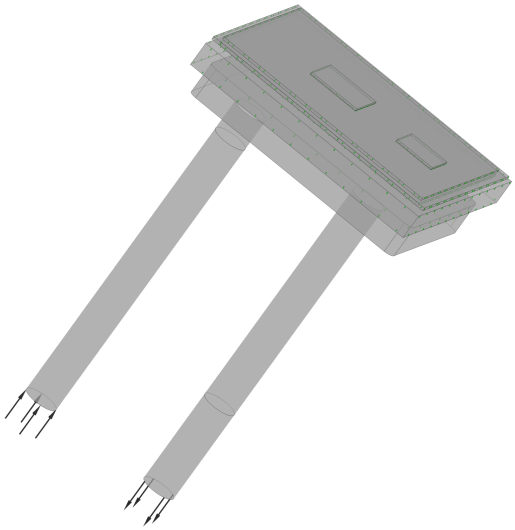

Fig. B.1. CFD model geometry.

simulated, which consists of one IGBT and one diode die. In the model, both dies are configured as heat sources. Example simulation results are shown in Fig. B.2. The temperature distribution within the power module is presented for inlet pressure of 10 kPa and heat losses of 150 and 50 W for the IGBT and the diode chips, respectively.

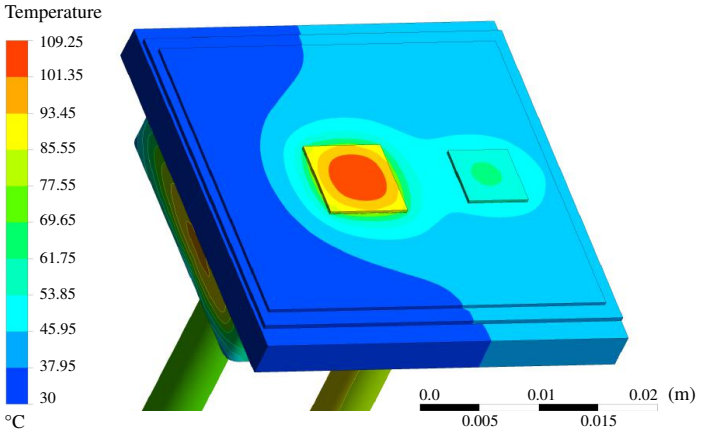

(a)

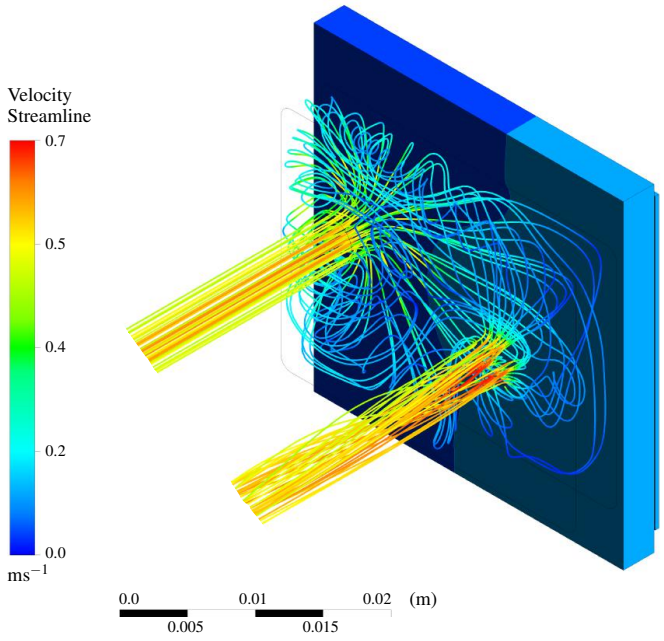

(b)

Fig. B.2. Example CFD simulation results for heat losses of 150 W for the IGBT chip, 50 W for the diode chip, and 10 kPa inlet pressure: (a) temperature and (b) flow velocity.

Coefficients C_1 and C_2

Equation (4.12) provides a relationship between the pressure head, P_{MHD}, and the fluid velocity, u. As Fig. B.3 shows, coefficients C_1 and C_2 were determined by multiple CFD simulation trials, where P_{MHD} and the corresponding u were varied. Therefore, velocity u can be calculated as a function of P_{MHD}:

$$P_{\mathrm{MHD}} \approx 1.085\rho u^2 + 0.0123\rho u \tag{B.1}$$

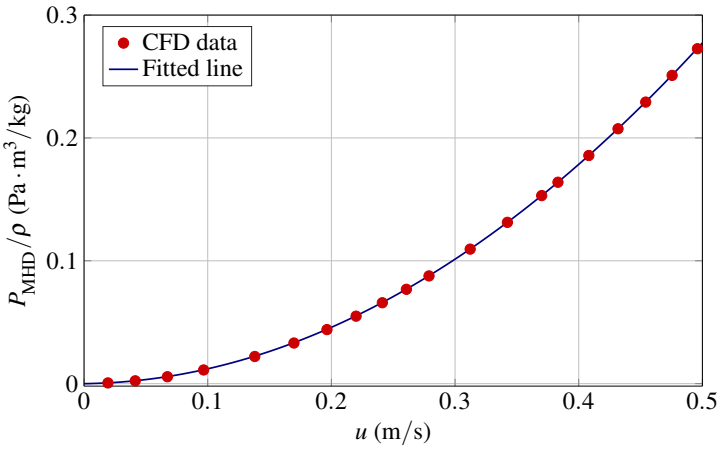

Fig. B.3. Computation of coefficients C_1 and C_2.

Appendix C

Press–pack liquid metal heat sink drawings and pictures

Drawings containing dimensions for the liquid metal–to–water heat exchanger, the liquid metal heat sink, the copper lids, and the busbar are presented in Fig. C.1, C.2 and C.3, respectively.

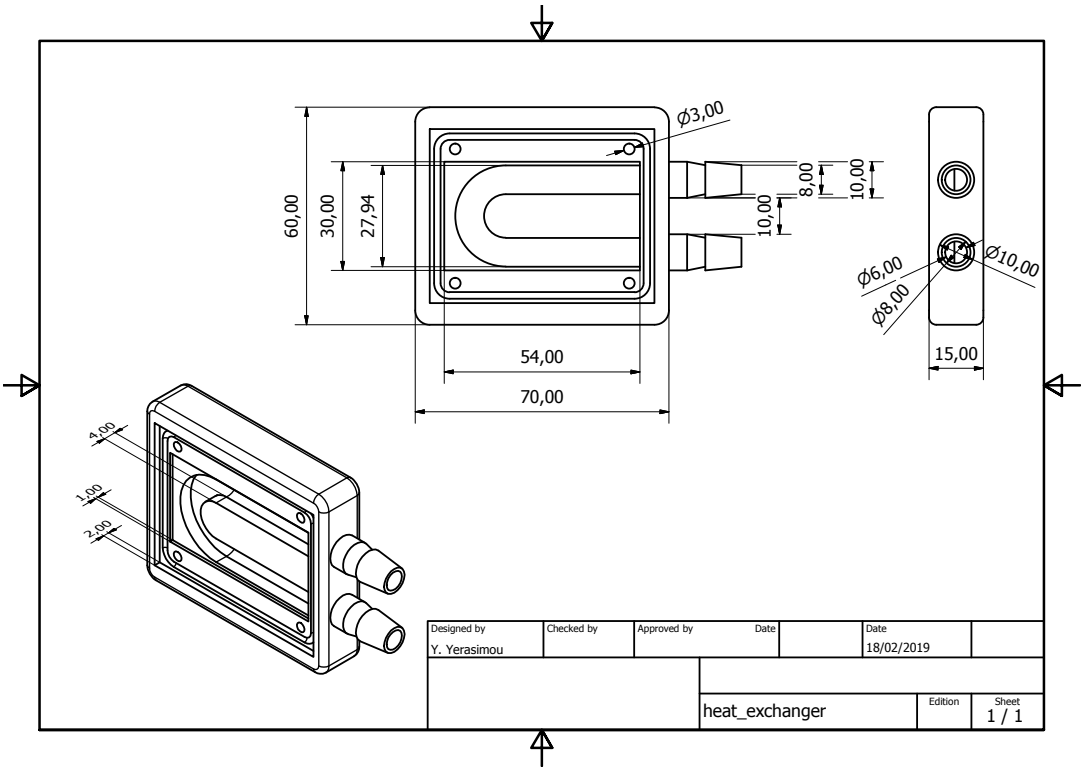

Fig. C.1. Dimensions of liquid metal–to–water heat exchanger.

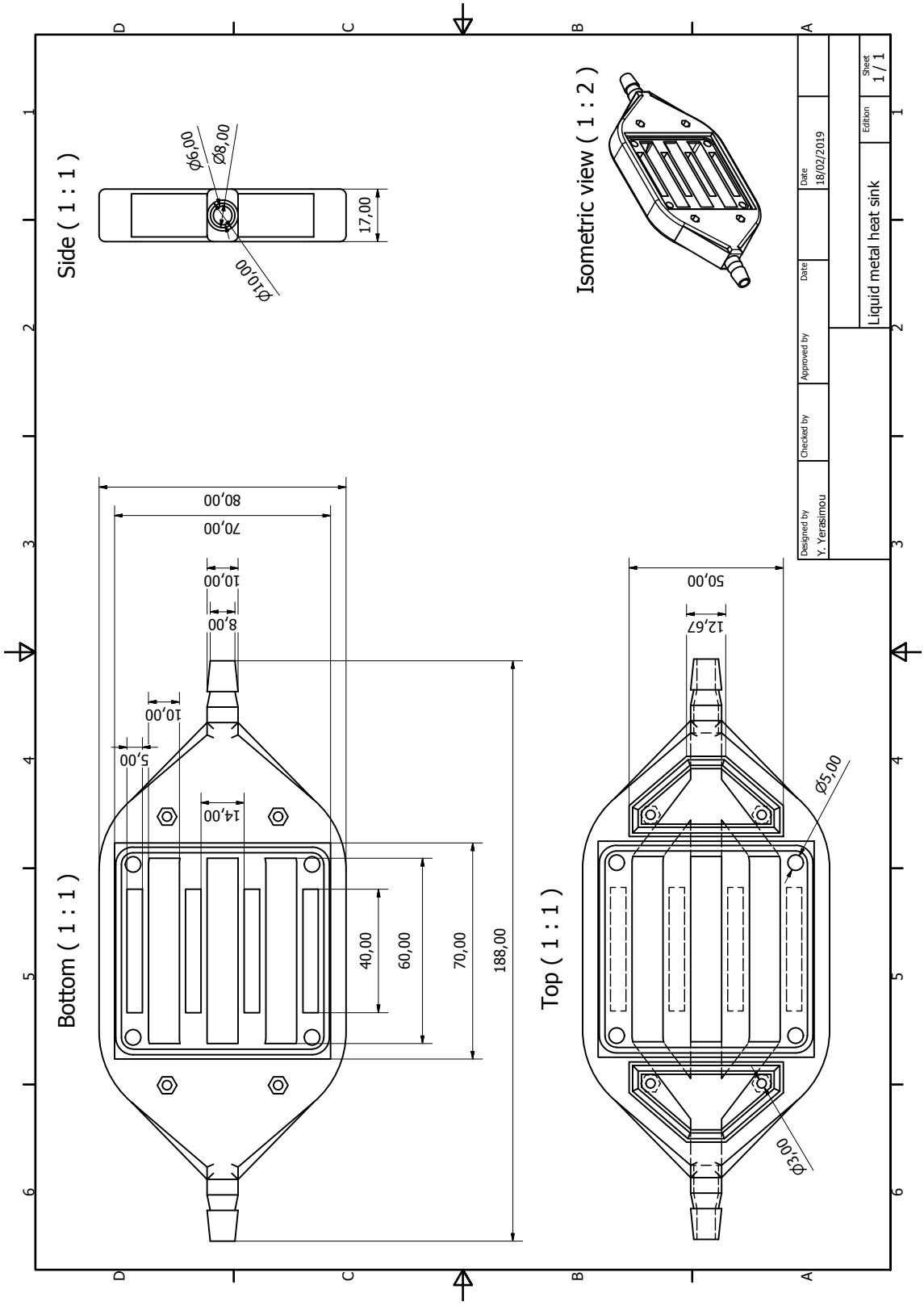

Fig. C.2. Dimensions of proposed liquid metal heat sink for press–pack devices.

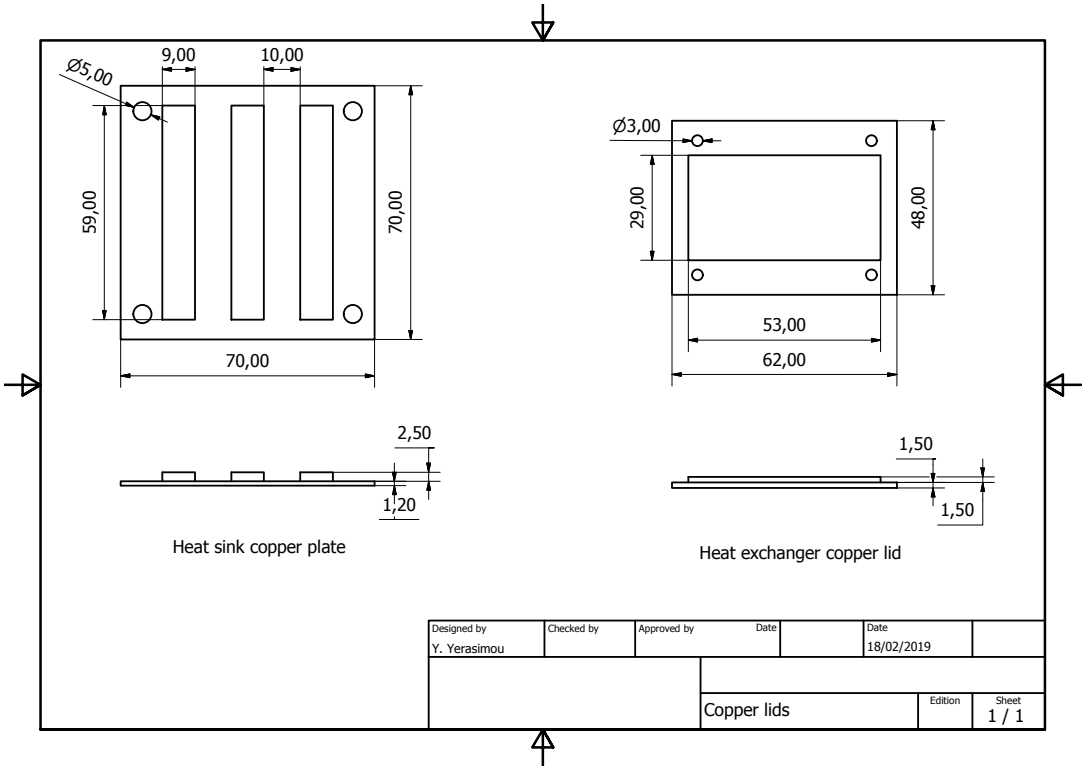

Fig. C.3. Dimensions of copper lids for heat sink and heat exchanger.

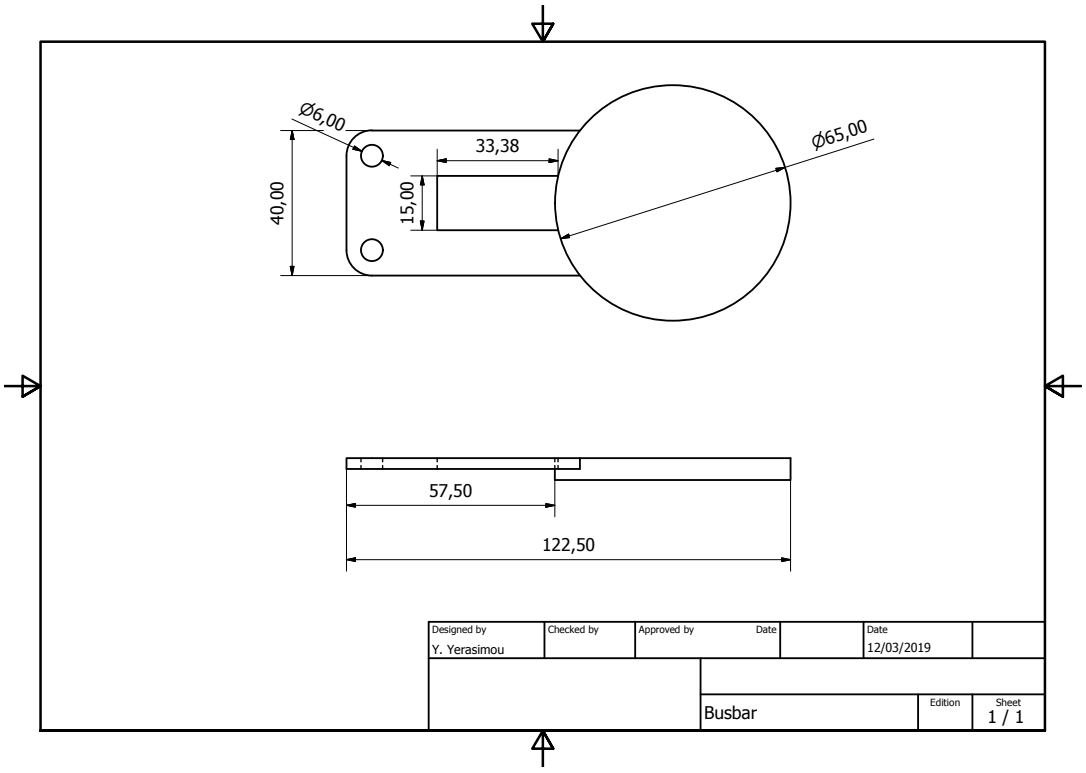

Fig. C.4. Dimensions of copper busbar for liquid metal press–pack cooling.

Figures C.5–C.8 shows pictures of the prototype heat sink, the heat exchanger and the copper lid and busbar. Moreover, Fig. C.9 shows pictures of the liquid metal cooling system for PPI devices that was experimentally tested.

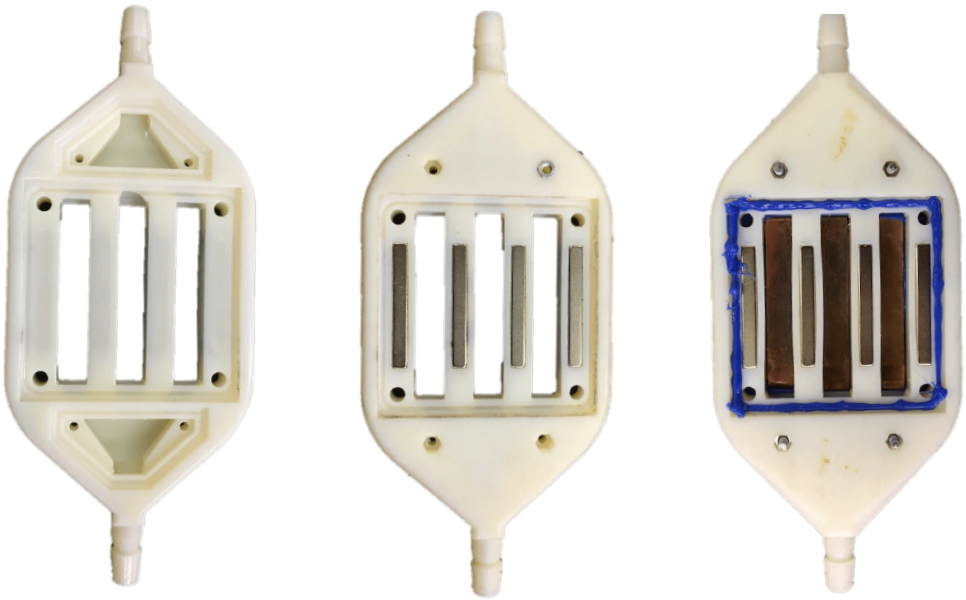

(a) (b) (c)

Fig. C.5. Picture of liquid metal heat sink for press–pack devices: (a) front view, (b) back view with integrated permanent magnets and (c) with sealant applied.

(a) (b) (c)

Fig. C.6. Picture of prototype liquid metal–to–water heat exchanger: (a) front view, (b) with sealant applied and (c) with ceramic aluminium oxide layer applied.

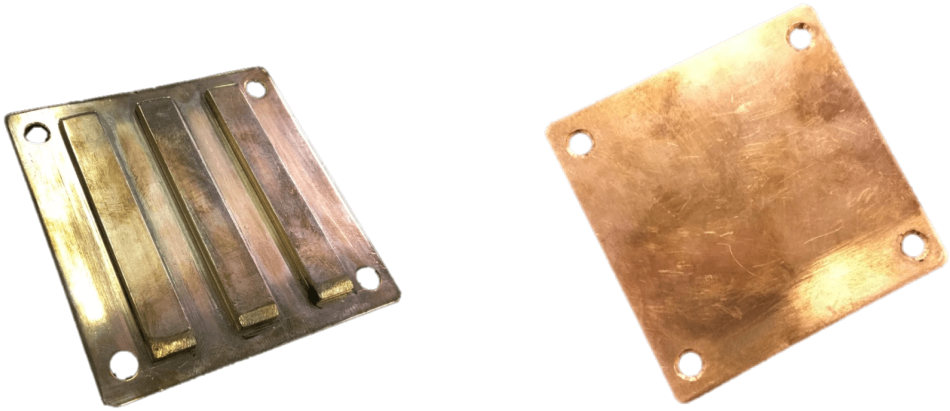

(a) **(b)**

Fig. C.7. Picture of copper plate for press–pack heat sink: (a) front and (b) back view.

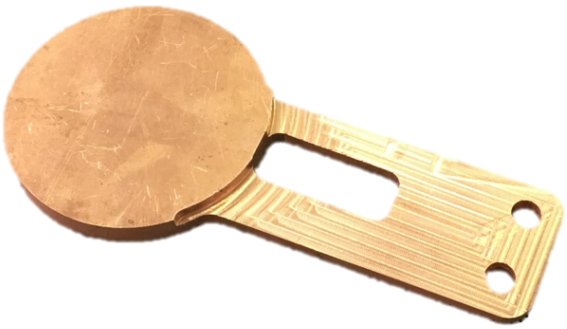

Fig. C.8. Copper busbar for liquid metal press–pack cooling.

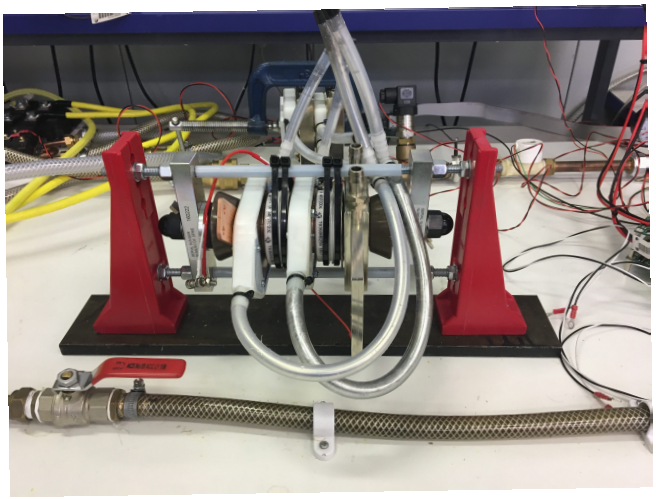

(a)

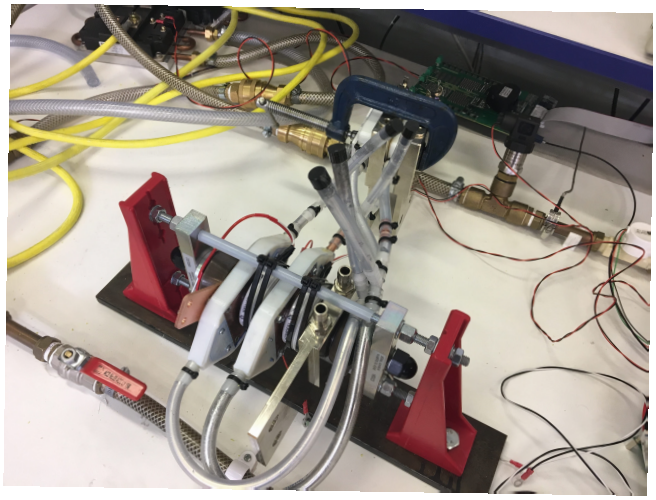

(b)

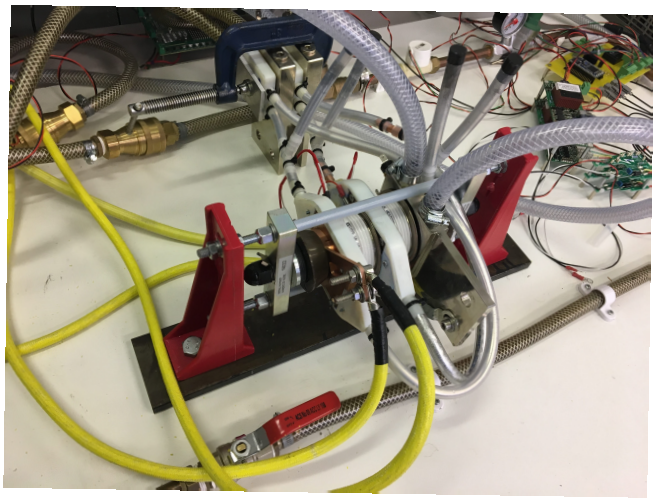

(c)

Fig. C.9. Pictures of the liquid metal cooling system for PPIs.

References

[1] The European Commission, *Green Paper 2030: Main outcomes of the public consultation*, 2013.

[2] International Energy Agency, *Global EV Outlook 2018: 3 million and counting*, 2018.

[3] Yole Developpment, *Status of the power electronics industry report*, July 2017.

[4] B. J. Baliga, "Chapter 1 - Introduction," in *The IGBT Device*, B. J. Baliga, Ed. Amsterdam: William Andrew Publishing, 2015, pp. 1 – 18.

[5] Y. Deng and J. Liu, "Hybrid liquid metal–water cooling system for heat dissipation of high power density microdevices," *Heat and Mass Transfer*, vol. 46, no. 11, pp. 1327–1334, Dec 2010.

[6] Y. Hayashi, N. Saneie, Y. J. Kim, and J.-H. Kim, "Thermal performance and pressure drop of galinstan-based microchannel heat-sink for high heat-flux thermal management," no. 56871, p. V001T07A012, 2015, 10.1115/ICNMM2015-48404.

[7] M. Hodes, R. Zhang, L. S. Lam, R. Wilcoxon, and N. Lower, "On the potential of galinstan-based minichannel and minigap cooling," *IEEE Transactions on Components, Packaging and Manufacturing Technology*, vol. 4, no. 1, pp. 46–56, Jan 2014.

[8] R. Zhang, M. Hodes, N. Lower, and R. Wilcoxon, "Water-based microchannel and galinstan-based minichannel cooling beyond 1 kW/cm^2 heat flux," *IEEE Transactions on Components, Packaging and Manufacturing Technology*, vol. 5, no. 6, pp. 762–770, June 2015.

[9] U. Ghoshal, D. Grimm, S. Ibrani, C. Johnston, and A. Miner, "High-performance liquid metal cooling loops," in *Semiconductor Thermal Measurement and Management IEEE Twenty First Annual IEEE Symposium, 2005.*, March 2005, pp. 16–19.

[10] Y. Deng and J. Liu, "Design of practical liquid metal cooling device for heat dissipation of high performance cpus," *Journal of Electronic Packaging*, vol. 132, no. 3, pp. 031 009–031 009–6, 2010, 10.1115/1.4002012.

[11] Y. Deng and J. Liu, "Optimization and evaluation of a high-performance liquid metal cpu cooling product," *IEEE Transactions on Components, Packaging and Manufacturing Technology*, vol. 3, no. 7, pp. 1171–1177, July 2013.

[12] T. Li, Y.-G. Lv, J. Liu, and Y.-X. Zhou, "A powerful way of cooling computer chip using liquid metal with low melting point as the cooling fluid," *Forschung im Ingenieurwesen*, vol. 70, no. 4, pp. 243–251, Dec 2005.

[13] J. Vetrovec, D. A. Copeland, R. Feeler, and J. Junghans, "Testing of active heat sink for advanced high-power laser diodes," *Proc.SPIE*, vol. 7918, pp. 7918 – 7918 – 6, 2011.

[14] Y. Deng and J. Liu, "A liquid metal cooling system for the thermal management of high power leds," *International Communications in Heat and Mass Transfer*, vol. 37, no. 7, pp. 788 – 791, 2010.

[15] M. Luo, Y. Zhou, and J. Liu, "Blade heat dissipator with room-temperature liquid metal running inside a sheet of hollow chamber," *IEEE Transactions on Components, Packaging and Manufacturing Technology*, vol. 4, no. 3, pp. 459–464, March 2014.

[16] R. Wilcoxon, N. Lower, and D. Dlouhy, "A compliant thermal spreader with internal liquid metal cooling channels," in *2010 26th Annual IEEE Semiconductor Thermal Measurement and Management Symposium (SEMI-THERM)*, Feb 2010, pp. 210–216.

[17] A. Sakanova, C. F. Tong, K. J. Tseng, R. Simanjorang, and A. K. Gupta, "Weight consideration of liquid metal cooling technology for power electronics converter in future aircraft," in *2016 IEEE 2nd Annual Southern Power Electronics Conference (SPEC)*, Dec 2016, pp. 1–5.

[18] M. Tawk, Y. Avenas, A. Kedous-Lebouc, and M. Petit, "Numerical and experimental investigations of the thermal management of power electronics with liquid metal mini-channel coolers," *IEEE Transactions on Industry Applications*, vol. 49, no. 3, pp. 1421–1429, May 2013.

[19] M. Luo and J. Liu, "Experimental investigation of liquid metal alloy based mini-channel heat exchanger for high power electronic devices," *Frontiers in Energy*, vol. 7, no. 4, pp. 479–486, Dec 2013.

[20] J. Vetrovec, "High-performance heat sink for hybrid electric vehicle inverters," *Volume 4: 12th International Conference on Advanced Vehicle and Tire Technologies; 4th International Conference on Micro- and Nanosystems*, 2010.

[21] J. Y. Zhu, S.-Y. Tang, K. Khoshmanesh, and K. Ghorbani, "An integrated liquid cooling system based on galinstan liquid metal droplets," *ACS Applied Materials & Interfaces*, vol. 8, no. 3, pp. 2173–2180, 2016, pMID: 26716607.

[22] S. Tan, Y. Zhou, L. Wang, and J. Liu, "Electrically driven chip cooling device using hybrid coolants of liquid metal and aqueous solution," *Science China Technological Sciences*, vol. 59, no. 2, pp. 301–308, Feb 2016.

[23] K.-Q. Ma and J. Liu, "Heat-driven liquid metal cooling device for the thermal management of a computer chip," *Journal of Physics D: Applied Physics*, vol. 40, no. 15, p. 4722, 2007.

[24] P. Li, J. Liu, and Y. Zhou, "Design of a self-driven liquid metal cooling device for heat dissipation of hot chips in a closed cabinet," *Journal of Thermal Science and Engineering Applications*, vol. 6, no. 1, pp. 011 009–011 009–8, 2013, 10.1115/1.4024786.

[25] K. De Vogeleer, G. Memmi, P. Jouvelot, and F. Coelho, "Theoretical analysis of radiative cooling for mobile and embedded systems," *arXiv preprint arXiv:1410.0628*, 2014.

[26] H. Wang, M. Su, and K. Sheng, "Theoretical performance limit of the IGBT," *IEEE Transactions on Electron Devices*, vol. 64, no. 10, pp. 4184–4192, Oct 2017.

[27] J. Falck, C. Felgemacher, A. Rojko, M. Liserre, and P. Zacharias, "Reliability of power electronic systems: An industry perspective," *IEEE Industrial Electronics Magazine*, vol. 12, no. 2, pp. 24–35, June 2018.

[28] S. Yang, A. Bryant, P. Mawby, D. Xiang, L. Ran, and P. Tavner, "An industry-based survey of reliability in power electronic converters," *IEEE Transactions on Industry Applications*, vol. 47, no. 3, pp. 1441–1451, 2011.

[29] D. Zhou, F. Blaabjerg, M. Lau, and M. Tonnes, "Thermal cycling overview of multi-megawatt two-level wind power converter at full grid code operation," *IEEJ Journal of Industry Applications*, vol. 2, no. 4, pp. 173–182, 2013.

[30] Y. Huaiyu, S. Koh, H. van Zeijl, A. Gielen, and Z. Guoqi, "A review of passive thermal management of LED module," *Journal of Semiconductors*, vol. 32, no. 1, p. 014008, 2011.

[31] G. Maranzana, I. Perry, D. Maillet, and S. Raël, "Design optimization of a spreader heat sink for power electronics," *International Journal of Thermal Sciences*, vol. 43, no. 1, pp. 21 – 29, 2004.

[32] D. Schweitzer, H. Pape, and L. Chen, "Transient measurement of the junction-to-case thermal resistance using structure functions: Chances and limits," in *2008 Twenty-fourth Annual IEEE Semiconductor Thermal Measurement and Management Symposium*, March 2008, pp. 191–197.

[33] J. Zhong, D. Liu, Z. Li, and X. Sun, "High thermal conductivity materials and their application on the electronic products," in *2012 IEEE Asia-Pacific Conference on Antennas and Propagation*, Aug 2012, pp. 173–175.

[34] D. I. Bradley, A. M. Guénault, D. Gunnarsson, R. P. Haley, S. Holt, A. T. Jones, Y. A. Pashkin, J. Penttilä, J. R. Prance, M. Prunnila, and L. Roschier, "On-chip magnetic cooling of a nanoelectronic device," *Scientific Reports*, vol. 7, p. 45566, 2017.

[35] A. Martinez, D. Astrain, and P. Aranguren, "Thermoelectric self-cooling for power electronics: Increasing the cooling power," *Energy*, vol. 112, pp. 1 – 7, 2016.

[36] H. Zhang, Y. Mui, and M. Tarin, "Analysis of thermoelectric cooler performance for high power electronic packages," *Applied Thermal Engineering*, vol. 30, no. 6, pp. 561 – 568, 2010.

[37] F. Jin and S. Little, "Thermionic cooling with functionalized carbon nanotube thin films," *Applied Physics Letters*, vol. 106, no. 11, p. 113102, 2015.

[38] J. S. Brown and P. A. Domanski, "Review of alternative cooling technologies," *Applied Thermal Engineering*, vol. 64, no. 1, pp. 252 – 262, 2014.

[39] U. Drofenik, A. Stupar, and J. W. Kolar, "Analysis of theoretical limits of forced-air cooling using advanced composite materials with high thermal conductivities," *IEEE Transactions on Components, Packaging and Manufacturing Technology*, vol. 1, no. 4, pp. 528–535, April 2011.

[40] M. Chinthavali, Z. J. Wang, S. Campbell, T. Wu, and B. Ozpineci, "50-kW 1kV DC bus air-cooled inverter with 1.7 kV SiC MOSFETs and 3D-printed novel power module packaging structure for grid applications," in *2018 IEEE Applied Power Electronics Conference and Exposition (APEC)*, March 2018, pp. 133–140.

[41] G. M. Gilson, S. J. Pickering, D. B. Hann, and C. Gerada, "Piezoelectric fan cooling: A novel high reliability electric machine thermal management solution," *IEEE Transactions on Industrial Electronics*, vol. 60, no. 11, pp. 4841–4851, Nov 2013.

[42] C. Cadile, A. Rumpf, D. Elzo, and J. P. Fradin, "Hydrodynamics behaviour study of a Dual piezoelectric cool jet (DCJ) system on the thermal cooling of electronic casings," in *2017 23rd International Workshop on Thermal Investigations of ICs and Systems (THERMINIC)*, Sept 2017, pp. 1–4.

[43] G. Buchberger, B. Jakoby, J. Schöftner, A. Schützenberger, B. Wiesmayr, W. Baumgartner, S. Puttinger, A. Brandl, and W. Hilber, "Simple synthetic jet actuators for cooling applications using soft or rigid magnets," *Procedia Engineering*, vol. 168, pp. 1541 – 1546, 2016, proceedings of the 30th anniversary Eurosensors Conference – Eurosensors 2016, 4-7. Sepember 2016, Budapest, Hungary.

[44] N. E. Jewell-Larsen, H. Ran, Y. Zhang, M. K. Schwiebert, K. A. H. Tessera, and A. V. Mamishev, "Electrohydrodynamic (EHD) cooled laptop," in *2009 25th Annual IEEE Semiconductor Thermal Measurement and Management Symposium*, March 2009, pp. 261–266.

[45] S. W. Chau, C. H. Lin, C. H. Yeh, and C. Yang, "Study on the cooling enhancement of LED heat sources via an electrohydrodynamic approach," in *IECON 2007 - 33rd Annual Conference of the IEEE Industrial Electronics Society*, Nov 2007, pp. 2934–2937.

[46] K. Tartibu, B. Sun, and M. A. E. Kaunda, "Geometric optimization of micro-thermoacoustic cooler for heat management in electronics," in *2013 IEEE International Conference on Industrial Technology (ICIT)*, Feb 2013, pp. 527–532.

[47] S. G. Kandlikar, "High flux heat removal with microchannels—a roadmap of challenges and opportunities," *Heat Transfer Engineering*, vol. 26, no. 8, pp. 5–14, 2005.

[48] S. C. Mohapatra and D. Loikits, "Advances in liquid coolant technologies for electronics cooling," in *Semiconductor Thermal Measurement and Management IEEE Twenty First Annual IEEE Symposium, 2005.*, March 2005, pp. 354–360.

[49] E. Laloya, O. Lucia, H. Sarnago, and J. M. Burdio, "Heat management in power converters: From state of the art to future ultrahigh efficiency systems," *IEEE Transactions on Power Electronics*, vol. 31, no. 11, pp. 7896–7908, Nov 2016.

[50] K. Yuki and K. Suzuki, "Applicability of minichannel cooling fins to the next generation power devices as a single-phase-flow heat transfer device," *Transactions of The Japan Institute of Electronics Packaging*, vol. 4, no. 1, pp. 52–60, 2011.

[51] S. T. Kadam and R. Kumar, "Twenty first century cooling solution: Microchannel heat sinks," *International Journal of Thermal Sciences*, vol. 85, pp. 73 – 92, 2014.

[52] A. Abdollahi, H. Mohammed, S. Vanaki, A. Osia, and M. G. Haghighi, "Fluid flow and heat transfer of nanofluids in microchannel heat sink with V-type inlet/outlet arrangement," *Alexandria Engineering Journal*, vol. 56, no. 1, pp. 161 – 170, 2017.

[53] H. Oprins, G. V. der Veken, C. C. S. Nicole, C. J. M. Lasance, and M. Baelmans, "On-chip liquid cooling with integrated pump technology," *IEEE Transactions on Components and Packaging Technologies*, vol. 30, no. 2, pp. 209–217, June 2007.

[54] G. Bindiganavale, S. M. You, and H. Moon, "Study of hotspot cooling using electrowetting on dielectric digital microfluidic system," in *2014 IEEE 27th International Conference on Micro Electro Mechanical Systems (MEMS)*, Jan 2014, pp. 1039–1042.

[55] M. Wada, A. Matsunaga, M. Hachiya, M. Chiba, K. Ishihara, and M. Yoshikawa, "Feasibility study of two-phase immersion cooling in closed electronic device," in *2017 16th IEEE Intersociety Conference on Thermal and Thermomechanical Phenomena in Electronic Systems (ITherm)*, May 2017, pp. 899–904.

[56] H. C. Coles and M. Herrlin, "Immersion cooling of electronics in DoD installations," U.S. Naval Research Laboratory (NRL), Tech. Rep., 05/2016 2016.

[57] K. Gould, S. Q. Cai, C. Neft, and A. Bhunia, "Liquid jet impingement cooling of a silicon carbide power conversion module for vehicle applications," *IEEE Transactions on Power Electronics*, vol. 30, no. 6, pp. 2975–2984, June 2015.

[58] J. Jörg, S. Taraborrelli, G. Sarriegui, R. W. D. Doncker, R. Kneer, and W. Rohlfs, "Direct single impinging jet cooling of a MOSFET power electronic module," *IEEE Transactions on Power Electronics*, vol. 33, no. 5, pp. 4224–4237, May 2018.

[59] H. Shabgard, M. J. Allen, N. Sharifi, S. P. Benn, A. Faghri, and T. L. Bergman, "Heat pipe heat exchangers and heat sinks: Opportunities, challenges, applications, analysis, and state of the art," *International Journal of Heat and Mass Transfer*, vol. 89, pp. 138 – 158, 2015.

[60] M. H. Kusuma, N. Putra, A. R. Antariksawan, R. A. Koestoer, S. Widodo, S. Ismarwanti, and B. T. Verlambang, "Passive cooling system in a nuclear spent fuel pool using a vertical straight wickless-heat pipe," *International Journal of Thermal Sciences*, vol. 126, pp. 162 – 171, 2018.

[61] P. Smakulski and S. Pietrowicz, "A review of the capabilities of high heat flux removal by porous materials, microchannels and spray cooling techniques," *Applied Thermal Engineering*, vol. 104, pp. 636 – 646, 2016.

[62] W.-L. Cheng, W.-W. Zhang, H. Chen, and L. Hu, "Spray cooling and flash evaporation cooling: The current development and application," *Renewable and Sustainable Energy Reviews*, vol. 55, pp. 614 – 628, 2016.

[63] A. Arshad, H. M. Ali, M. Ali, and S. Manzoor, "Thermal performance of phase change material (PCM) based pin-finned heat sinks for electronics devices: Effect of pin thickness and PCM volume fraction," *Applied Thermal Engineering*, vol. 112, pp. 143 – 155, 2017.

[64] H. Farhat, I. Mjallal, M. Hammoud, S. Ali, A. A. Shaer, A. Assi, and I. Assi, "Investigating the effect of the density of phase change materials on cooling electronic packages," in *2017 29th International Conference on Microelectronics (ICM)*, Dec 2017, pp. 1–5.

[65] H. Lu and C. Bailey, "Lifetime prediction of an IGBT power electronics module under cyclic temperature loading conditions," in *2009 International Conference on Electronic Packaging Technology High Density Packaging*, Aug 2009, pp. 274–279.

[66] M. Faraday, "VI. the Bakerian lecture. - Experimental researches in electricity. - Second series," *Philosophical Transactions of the Royal Society of London*, vol. 122, pp. 163–194, 1832.

[67] J. M. Lafferty, "Michael Faraday's Waterloo Bridge Experiment at museum of innovation and science," *General Electric Company. Research Laboratory*, 1961, accessed: 2018-07-20. [Online]. Available: http://nyheritage.nnyln.org/digital/collection/p16694coll20/id/327/

[68] S.-I. Pai, *Magnetogasdynamics and Plasma Dynamics*. Springer Vienna, 1962.

[69] E. F. Northrup, "Some newly observed manifestations of forces in the interior of an electric conductor," *Phys. Rev. (Series I)*, vol. 24, pp. 474–497, Jun 1907.

[70] G. Dannen, "The Einstein-Szilard refrigerators," *Scientific American*, vol. 276, no. 1, pp. 90–95, 1997.

[71] J. Hartmann, "Hg-dynamics II : experimental investigations on the flow of mercury in a homogeneous magnetic field," København, 1937.

[72] H. Alfvén, "Interplanetary Magnetic Field," in *Electromagnetic Phenomena in Cosmical Physics*, ser. IAU Symposium, B. Lehnert, Ed., vol. 6, 1958, p. 284.

[73] P. A. Davidson, *An Introduction to Magnetohydrodynamics*, ser. Cambridge Texts in Applied Mathematics. Cambridge University Press, 2001.

[74] M. Haghparast, "Transient analysis of magnetohydrodynamic seawater thrusters with decaying magnetic field," *Ships and Offshore Structures*, vol. 12, no. 5, pp. 591–598, 2017.

[75] M. Haghparast, M. R. A. Pahlavani, and D. Azizi, "Numerical investigation of the effects of magnetic field and fluid electrical conductivity on the performance of marine magnetohydrodynamic motors," *IET Electric Power Applications*, May 2018.

[76] J. Overduin, V. Polyak, A. Rutah, T. Sebastian, J. Selway, and D. Zile, "The Hunt for Red October II: A magnetohydrodynamic boat demonstration for introductory physics," *The Physics Teacher*, vol. 55, no. 8, pp. 460–466, 2017.

[77] S. Khripchenko, S. Lekomtsev, S. Denisov, V. Dolgikh, and A. Pavlinov, "Laboratory model of the aluminum furnace with mhd stirring induced by a rod-like inductor generating a travelling magnetic field." *Magnetohydrodynamics (0024-998X)*, vol. 53, no. 2, 2017.

[78] K. E. Bolotin, V. E. Frizen, I. F. Sokolov, and S. A. Bychkov, "Numerical simulation of mhd stirrer for 12 ton metallurgical aggregate," in *2018 IEEE Conference of Russian Young Researchers in Electrical and Electronic Engineering (EIConRus)*, Jan 2018, pp. 585–587.

[79] V. Timofeev and M. Khatsayuk, "Theoretical design fundamentals for MHD stirrers for molten metals." *Magnetohydrodynamics (0024-998X)*, vol. 52, no. 4, 2016.

[80] V. Batenin, I. Belyaev, V. Sviridov, E. Sviridov, and Y. I. Listratov, "Modernization of the experimental base for studies of MHD heat exchange at advanced nuclear power facilities," *High Temperature*, vol. 53, no. 6, pp. 904–907, 2015.

[81] J. E. Nieminen and C. O. Maidana, "Comparative studies for the MHD modeling of annular linear induction pumps for space applications," in *15th International Energy Conversion Engineering Conference*, 2017, p. 4963.

[82] A. Shahidian, M. Ghassemi, S. Khorasanizade, M. Abdollahzade, and G. Ahmadi, "Flow analysis of non-newtonian blood in a magnetohydrodynamic pump," *IEEE transactions on magnetics*, vol. 45, no. 6, pp. 2667–2670, 2009.

[83] F. Khan, D. Baucom, C. D. Heyes, and I. Fritsch, "Studies toward lab-on-a-chip separations and detection using redox magnetohydrodynamic microfluidics," in *Meeting Abstracts*, no. 42. The Electrochemical Society, 2015, pp. 2227–2227.

[84] T. Takahashi, T. Fujino, and M. Ishikawa, "Comparison of generator performance of small-scale mhd generators with different electrode dispositions and load connection systems," *Journal of International Council on Electrical Engineering*, vol. 4, no. 3, pp. 192–198, 2014.

[85] H. Liancheng, K. Hiromichi, and O. Yoshihiro, "Analyses on response of a liquid metal mhd power generation system to various external inputs," *IEEJ Transactions on Electrical and Electronic Engineering*, vol. 10, no. 3, pp. 268–273.

[86] X.-D. Niu, H. Yamaguchi, X.-J. Ye, and Y. Iwamoto, "Characteristics of a mhd power generator using a low-melting-point gallium alloy," *Electrical Engineering*, vol. 96, no. 1, pp. 37–43, Mar 2014.

[87] H. Kobayashi, H. Shionoya, and Y. Okuno, "Turbulent duct flows in a liquid metal magnetohydrodynamic power generator," *Journal of Fluid Mechanics*, vol. 713, p. 243–270, 2012.

[88] L. Zhao, H. Ye, A. Peng, Q. Zhang, Q. Xia, B. Liu, J. Li, F. Wang, R. Li *et al.*, "Mhd wave energy underwater recharging platforms for auvs," in *The 26th International Ocean and Polar Engineering Conference*. International Society of Offshore and Polar Engineers, 2016.

[89] E. R. Morgan and M. W. Shafer, "Marine energy harvesting using magnetohydrodynamic power generation," in *ASME 2014 Conference on Smart Materials, Adaptive Structures and Intelligent Systems*. American Society of Mechanical Engineers, 2014, pp. V002T07A018–V002T07A018.

[90] V. Bandaru, I. Sokolov, and T. Boeck, "Lorentz force transient response at finite magnetic reynolds numbers," *IEEE Transactions on Magnetics*, vol. 52, no. 8, pp. 1–11, Aug 2016.

[91] A. Wiederhold, C. Resagk, and C. Cierpka, "On the influence of gas-liquid two-phase flow on lorentz force velocimetry," *Measurement Science and Technology*, 2018.

[92] R. Jebahi, M. Ayadi, H. Aloui, and R. Néji, "1d thermal modelling of pmsm intended for an electric vehicle's powertrain," in *2014 International Conference on Electrical Sciences and Technologies in Maghreb (CISTEM)*, Nov 2014, pp. 1–5.

[93] H. S. Sohn, N. K. Kim, J. J. Chae, C. H. Yeo, and J. H. Kim, "2d fully coupled analysis with magneto-thermal model for prediction of temperature distribution on uhv gib," in *2013 2nd International Conference on Electric Power Equipment - Switching Technology (ICEPE-ST)*, Oct 2013, pp. 1–4.

[94] A. S. Bahman, K. Ma, P. Ghimire, F. Iannuzzo, and F. Blaabjerg, "A 3-d-lumped thermal network model for long-term load profiles analysis in high-power igbt modules," *IEEE Journal of Emerging and Selected Topics in Power Electronics*, vol. 4, no. 3, pp. 1050–1063, Sept 2016.

[95] X. Song, V. Pickert, B. Ji, R. T. Naayagi, C. Wang, and Y. Yerasimou, "Questionnaire-based discussion of finite element multiphysics simulation software in power electronics," *IEEE Transactions on Power Electronics*, vol. 33, no. 8, pp. 7010–7020, Aug 2018.

[96] Z. Zhou, P. M. Holland, and P. Igic, "Compact thermal model of a three-phase igbt inverter power module," in *2008 26th International Conference on Microelectronics*, May 2008, pp. 167–170.

[97] J. Zhang, X. Du, P. Sun, and H. Tai, "Thermal network parameters identifying during the cooling procedure of igbt module," in *IECON 2017 - 43rd Annual Conference of the IEEE Industrial Electronics Society*, Oct 2017, pp. 1616–1621.

[98] Z. Wang, W. Qiao, B. Tian, and L. Qu, "An effective heat propagation path-based online adaptive thermal model for igbt modules," in *2014 IEEE Applied Power Electronics Conference and Exposition - APEC 2014*, March 2014, pp. 513–518.

[99] J. N. Davidson, D. A. Stone, and M. P. Foster, "Required cauer network order for modelling of thermal transfer impedance," *Electronics Letters*, vol. 50, no. 4, pp. 260–262, February 2014.

[100] J. R. Gyorki, "Design World: How to select a suitable heat sink," https://www.designworldonline.com/how-to-select-a-suitable-heat-sink/, 2011, accessed: 2020-04-20.

[101] A. T. Solutions, "IGBT cold plates," Tech. Rep., 04/2018.

[102] M. Musallam and C. M. Johnson, "Real-time compact thermal models for health management of power electronics," *IEEE Transactions on Power Electronics*, vol. 25, no. 6, pp. 1416–1425, June 2010.

[103] J. He, V. Mehrotra, and M. C. Shaw, "Thermal design and measurements of igbt power modules: transient and steady state," in *Conference Record of the 1999 IEEE Industry Applications Conference. Thirty-Forth IAS Annual Meeting (Cat. No.99CH36370)*, vol. 2, Oct 1999, pp. 1440–1444 vol.2.

[104] D. Werber and G. Wachutka, "Interpretation of laser absorption measurements on 4h-sic bipolar diodes by numerical simulation," in *2008 International Conference on Simulation of Semiconductor Processes and Devices*, Sept 2008, pp. 89–92.

[105] I. Bakun, N. Čobanov, and P. Željko Jakopović, "Real-time measurement of igbt's operating temperature," *Automatika*, vol. 52, no. 4, pp. 295–305, 2011.

[106] D. L. Blackburn, "Temperature measurements of semiconductor devices - a review," in *Twentieth Annual IEEE Semiconductor Thermal Measurement and Management Symposium (IEEE Cat. No.04CH37545)*, March 2004, pp. 70–80.

[107] Z. Sun, M. Ma, M. Zhan, and J. Wang, "Junction temperature estimation in igbt power modules based on kalman filter," in *2017 IEEE Conference on Energy Internet and Energy System Integration (EI2)*, Nov 2017, pp. 1–6.

[108] M. A. Eleffendi and C. M. Johnson, "Application of kalman filter to estimate junction temperature in igbt power modules," *IEEE Transactions on Power Electronics*, vol. 31, no. 2, pp. 1576–1587, Feb 2016.

[109] B. Strauss and A. Lindemann, "Measuring the junction temperature of an igbt using its threshold voltage as a temperature sensitive electrical parameter (tsep)," in *2016 13th International Multi-Conference on Systems, Signals Devices (SSD)*, March 2016, pp. 459–467.

[110] J. Wu, L. Zhou, X. Du, and P. Sun, "Junction temperature prediction of igbt power module based on bp neural network," *Journal of Electrical Engineering and Technology*, vol. 9, no. 3, pp. 970–977, 2014.

[111] B. Shi, S. Feng, L. Shi, D. Shi, Y. Zhang, and H. Zhu, "Junction temperature measurement method for power mosfets using turn-on delay of impulse signal," *IEEE Transactions on Power Electronics*, vol. 33, no. 6, pp. 5274–5282, June 2018.

[112] H. Luo, Y. Chen, P. Sun, W. Li, and X. He, "Junction temperature extraction approach with turn-off delay time for high-voltage high-power igbt modules," *IEEE Transactions on Power Electronics*, vol. 31, no. 7, pp. 5122–5132, July 2016.

[113] R. Mandeya, C. Chen, V. Pickert, and R. T. Naayagi, "Prethreshold voltage as a low-component count temperature sensitive electrical parameter without self-heating," *IEEE Transactions on Power Electronics*, vol. 33, no. 4, pp. 2787–2791, April 2018.

[114] B. Wang, J. Cai, X. Du, and L. Zhou, "Review of power semiconductor device reliability for power converters," *CPSS Transactions on Power Electronics and Applications*, vol. 2, no. 2, pp. 101–117, 2017.

[115] Y. Liu, M. Huang, H. Wang, X. Zha, J. Gong, and J. Sun, "Reliability-oriented optimization of the lc filter in a buck dc-dc converter," *IEEE Transactions on Power Electronics*, vol. 32, no. 8, pp. 6323–6337, 2017.

[116] S. Yang, D. Xiang, A. Bryant, P. Mawby, L. Ran, and P. Tavner, "Condition monitoring for device reliability in power electronic converters: A review," *IEEE Transactions on Power Electronics*, vol. 25, no. 11, pp. 2734–2752, 2010.

[117] R. Wu, F. Blaabjerg, H. Wang, M. Liserre, and F. Iannuzzo, "Catastrophic failure and fault-tolerant design of IGBT power electronic converters - an overview," in *IECON 2013 - 39th Annual Conference of the IEEE Industrial Electronics Society*, 2013, Conference Proceedings, pp. 507–513.

[118] B. Ji, V. Pickert, B. Zahawi, and M. Zhang, "In-situ bond wire health monitoring circuit for IGBT power modules," in *Power Electronics, Machines and Drives (PEMD 2012), 6th IET International Conference on*, Conference Proceedings, pp. 1–6.

[119] B. Ji, X. Song, W. Cao, V. Pickert, J. Hu, J. W. Mackersie, and G. Pierce, "In situ diagnostics and prognostics of solder fatigue in IGBT modules for electric vehicle drives," *Power Electronics, IEEE Transactions on*, vol. 30, no. 3, pp. 1535–1543, 2015.

[120] M. Andresen, K. Ma, G. Buticchi, J. Falck, F. Blaabjerg, and M. Liserre, "Junction temperature control for more reliable power electronics," *IEEE Transactions on Power Electronics*, vol. PP, no. 99, pp. 1–1, 2017.

[121] B. Liu, D. Liu, Y. Tang, and M. Chen, "The investigation on the lifetime prediction model of igbt module," *Energy Procedia*, vol. 12, pp. 394 – 402, 2011, the Proceedings of International Conference on Smart Grid and Clean Energy Technologies (ICSGCE 2011. [Online]. Available: http://www.sciencedirect.com/science/article/pii/S1876610211018790

[122] M. Held, P. Jacob, G. Nicoletti, P. Scacco, and M. H. Poech, "Fast power cycling test of IGBT modules in traction application," in *Proceedings of Second International Conference on Power Electronics and Drive Systems*, vol. 1, May 1997, pp. 425–430 vol.1.

[123] R. Bayerer, T. Herrmann, T. Licht, J. Lutz, and M. Feller, "Model for power cycling lifetime of IGBT modules - various factors influencing lifetime," in *Integrated Power Systems (CIPS), 2008 5th International Conference on*, Conference Proceedings, pp. 1–6.

[124] A. Wintrich, U. Nicolai, W. Tursky, and T. Reimann, "Application manual power semiconductors," 2015.

[125] H. Huang and P. A. Mawby, "A lifetime estimation technique for voltage source inverters," *IEEE Transactions on Power Electronics*, vol. 28, no. 8, pp. 4113–4119, Aug 2013.

[126] D. A. Murdock, J. E. R. Torres, J. J. Connors, and R. D. Lorenz, "Active thermal control of power electronic modules," *Industry Applications, IEEE Transactions on*, vol. 42, no. 2, pp. 552–558, 2006.

[127] M. Ke, M. Liserre, and F. Blaabjerg, "Reactive power influence on the thermal cycling of multi-MW wind power inverter," in *Applied Power Electronics Conference and Exposition (APEC), 2012 Twenty-Seventh Annual IEEE*, Conference Proceedings, pp. 262–269.

[128] J. Wolfle, O. Lehmann, and J. Roth-Stielow, "A novel control method to improve the reliability of traction inverters for permanent magnet synchronous machines," in *Power Electronics and Drive Systems (PEDS), 2015 IEEE 11th International Conference on*, Conference Proceedings, pp. 379–384.

[129] J. Lemmens, J. Driesen, and P. Vanassche, "Thermal management in traction applications as a constraint optimal control problem," in *Vehicle Power and Propulsion Conference (VPPC), 2012 IEEE*, Conference Proceedings, pp. 36–41.

[130] M. Andresen and M. Liserre, "Impact of active thermal management on power electronics design," *Microelectronics Reliability*, vol. 54, no. 9–10, pp. 1935–1939, 2014.

[131] W. Xiang, W. Yun, and A. Castellazzi, "Reduced active and passive thermal cycling degradation by dynamic active cooling of power modules," in *Power Semiconductor Devices & IC's (ISPSD), 2015 IEEE 27th International Symposium on*, Conference Proceedings, pp. 309–312.

[132] W. Xiang, A. Castellazzi, and P. Zanchetta, "Temperature control for reduced thermal cycling of power devices," in *Power Electronics and Applications (EPE), 2013 15th European Conference on*, Conference Proceedings, pp. 1–10.

[133] E. Laloya, L. Ó, H. Sarnago, and J. M. Burdío, "Heat management in power converters: From state of the art to future ultrahigh efficiency systems," *IEEE Transactions on Power Electronics*, vol. 31, no. 11, pp. 7896–7908, 2016.

[134] L. Cong, J. Da, J. Jizhou, G. Feng, and W. Jin, "Thermoelectric cooling for power electronics circuits: Modeling and active temperature control," *Industry Applications, IEEE Transactions on*, vol. 50, no. 6, pp. 3995–4005, 2014.

[135] X. Zhang and L.-D. Zhao, "Thermoelectric materials: Energy conversion between heat and electricity," *Journal of Materiomics*, vol. 1, no. 2, pp. 92–105, 2015.

[136] D. Zhou, F. Blaabjerg, M. Lau, and M. Tønnes, "Optimized reactive power flow of dfig power converters for better reliability performance considering grid codes," *IEEE Transactions on Industrial Electronics*, vol. 62, no. 3, pp. 1552–1562, March 2015.

[137] M. Ke, M. Liserre, F. Blaabjerg, and T. Kerekes, "Thermal loading and lifetime estimation for power device considering mission profiles in wind power converter," *Power Electronics, IEEE Transactions on*, vol. 30, no. 2, pp. 590–602, 2015.

[138] W. Lai, M. Chen, L. Ran, O. Alatise, S. Xu, and P. Mawby, "Low ΔT_j stress cycle effect in igbt power module die-attach lifetime modeling," *IEEE Transactions on Power Electronics*, vol. 31, no. 9, pp. 6575–6585, 2016.

[139] Y. Deng and J. Liu, "Hybrid liquid metal–water cooling system for heat dissipation of high power density microdevices," *Heat and Mass Transfer*, vol. 46, no. 11, pp. 1327–1334, 2010.

[140] M. Musallam, C. Yin, C. Bailey, and M. Johnson, "Mission profile-based reliability design and real-time life consumption estimation in power electronics," *IEEE Transactions on Power Electronics*, vol. 30, no. 5, pp. 2601–2613, 2015.

[141] X. Perpiñà, L. Navarro, X. Jordà, M. Vellvehi, J.-F. Serviere, and M. Mermet-Guyennet, "Reliability and lifetime prediction for IGBT modules in railway traction chains," in *Reliability and Safety in Railway*. InTech, 2012.

[142] S. Naceur, F. Z. Kadid, and R. Abdessemed, "The study of the electroconductive liquids flow in a conduction magnetohydrodynamic pump," *Trans. Electr. Electron. Mater.(TEEM)*, vol. 17, no. 5, pp. 252–256, 2016.

[143] TDK-Lambda, "175/180/200w configurable ac/dc power supply - nv-power nv-175."

[144] Y. Yerasimou, V. Pickert, B. Ji, and X. Song, "Liquid metal magnetohydrodynamic pump for junction temperature control of power modules," *IEEE Transactions on Power Electronics*, vol. 33, no. 12, pp. 10 583–10 593, Dec 2018.

[145] E. Deng, Z. Zhao, Z. Lin, R. Han, and Y. Huang, "Influence of temperature on the pressure distribution within press pack igbts," *IEEE Transactions on Power Electronics*, vol. 33, no. 7, pp. 6048–6059, July 2018.

[146] S. Eicher, M. Rahimo, E. Tsyplakov, D. Schneider, A. Kopta, U. Schlapbach, and E. Carroll, "4.5kv press pack igbt designed for ruggedness and reliability," in *Conference Record of the 2004 IEEE Industry Applications Conference, 2004. 39th IAS Annual Meeting.*, vol. 3, Oct 2004, pp. 1534–1539 vol.3.

[147] S. Wang, Z. Song, P. Fu, K. Wang, X. Xu, W. Tong, and Z. Wang, "Thermal analysis of water-cooled heat sink for solid-state circuit breaker based on igcts in parallel," *IEEE Transactions on Components, Packaging and Manufacturing Technology*, pp. 1–1, 2018.

[148] S. Fang, W. Luo, H. Wang, and H. Hu, "Operational performance of the valve cooling system in guangzhou converter station," in *11th IET International Conference on AC and DC Power Transmission*, Feb 2015, pp. 1–5.

[149] J.-S. Kwak, C.-K. Kim, and B.-E. Koh, "Cooling system of haenam-jeju hvdc system [power convertor]," in *ISIE 2001. 2001 IEEE International Symposium on Industrial Electronics Proceedings (Cat. No.01TH8570)*, vol. 2, June 2001, pp. 1000–1005 vol.2.

[150] R. J. Moffat, "Describing the uncertainties in experimental results," *Experimental Thermal and Fluid Science*, vol. 1, no. 1, pp. 3 – 17, 1988.

[151] H. W. Coleman and W. G. Steele, *Experimentation, validation, and uncertainty analysis for engineers*. John Wiley & Sons, 2018.

Index